Tribological characterization of reptile scales and their application as technical surfaces with tunable friction anisotropy

Zur Erlangung des akademischen Grades
Doktor der Ingenieurwissenschaften
von der KIT-Fakultät für Maschinenbau
des Karlsruher Instituts für Technologie (KIT)

genehmigte
Dissertation
von

M.Eng. Weibin Wu

Tag der mündlichen Prüfung:	25. September 2020
Hauptreferent:	apl. Prof. Dr. Hendrik Hölscher
Korreferenten:	Prof. Dr. Manfred Kohl
	Prof. Dr. André Schirmeisen

Abstract

Some reptiles surprise humans with excellent tribological properties in terms of adhesion, friction, and wear, which originate from the long time of evolution in their respective living environment. Mimicking these unique tribological properties enables researchers to develop reptile-inspired surfaces with similar or even more advanced abilities. Thus, studying the tribological properties of reptiles as well as transferring their design to the artificial surfaces are of great importance for finding new solutions to engineering problems which are related to friction and wear.

After a brief introduction into the topic and a short recall of the applied methodologies, four chapters of this thesis deal with different aspects of reptile scales. Chapter 3 focuses on the sandfish (*Scincus scincus*), which is widely known for its special ability to swim in loose, aeolian sand without noticeable wear on its scales. The microscopic structural and tribological properties of single sandfish scales are characterized by atomic force microscopy (AFM) with various types of probe including sharp silicon tips, spherical glass tips, and sand debris. Snake scales together with several technical surfaces are also analyzed for comparison. The experimental analysis demonstrates that scales of sandfish and snakes show lower friction coefficients than most technical surfaces. However, their adhesion and abrasion resistant properties are not superior to those of technical surfaces. Sandfish scales do not show any exceptional tribological properties if compared to snake scales. Other reasons such as the elastic properties of its epidermis or the dynamics of its locomotion are supposed to be responsible for the observed low wear rates of sandfish scales during the sand swimming.

The multi-functionality of the scales from different regions of the snake bodies (*i.e.* dorsal, ventral, and spectacle scales) are investigated in the next chapter. For an individual snake species, the micro-ornamentations on these three types of scales were found to be very different. The dorsal scales of different snake species feature diverse microstructures. However, the ventral scales of most investigated snakes show very similar oriented micro-fibril structures, and the spectacle scales demonstrate stitching polygon like structures. Characterization of the cross sectional architecture indicates stacked, layered structures on snake scales of all body regions. Ventral scales are nearly three times as thick as dorsal scales of the same species. Wettability, adhesion force, and spectral transmittance property were characterized and correlated with the micro-ornamentations on the scales. Dorsal scales are considered as the self-cleaning surface and light scattering filter to protect snakes from contamination and solar radiation. Spectacle snake scales sacrifice self-cleaning capability for obtaining high spectral transmittance in visible light and near-infrared spectrum. They can also block harmful ultraviolet light. Although displaying similar wettability and spectral transmitting ability as spectacle scales, ventral scales are widely accepted as a frictional component for optimizing the locomotion performances of snakes.

The fifth chapter deals with the frictional anisotropy of snake and sandfish scales. A sharp AFM tip scanning along the micro-fibril structures on ventral snake scales (*i.e.* upward and downward the nano-steps at the fibril ends) reveals significant friction anisotropy. Scanning up and down the nano-step structures of dorsal sandfish scales shows the same effect. The friction for an AFM tip scanning upward a nano-step increases significantly with the step height, while the increase is not apparent for downward scans. This effect leads to a nano-step height dependent friction anisotropy. A larger step height causes a larger friction anisotropy. With the micro-fibrils pointing towards the tail, snakes move much easier in forward than backward direction, which is favorable for them when climbing slops. The same effect is also found on a polymeric replica of *N. atra* ventral scale. Experiments with micro-tribometer coincide with the above results. More interestingly, snakes vary nano-step height and therefore the subsequent friction anisotropy in different segments of their bodies. A general distribution pattern of friction anisotropy is observed along the body of the examined snakes, *i.e.*, larger friction anisotropy in the middle and tail section than in the other areas. Snakes might benefit from such design to realize optimized frictional performances during locomotion.

Inspired by the step height dependent friction anisotropy found on the ventral scales of snakes, a tunable friction anisotropy surface was fabricated with shape memory polymers (SMPs) via hot embossing in Chapter 6. The shape memory effect of the polymers enables the surface to reversibly switch between a flattened topography and a micro-fibril structured topography, resulting in tunable anisotropic friction along the micro-fibrils. AFM characterization shows that the shape-changing capability in terms of nano-step height and friction anisotropy can reach up to nearly 1000% and 300%, respectively. Moreover, the SMP topography recovers continuously and controllably with heating time allowing it to achieve desired step height and friction anisotropy on the surface by abruptly terminating the heating before full recovery. Long-term stability and reusability tests reveal that, at any arbitrary stage of the SMP programming/recovery cycle, the step height at the micro-fibril ends is highly stable in three months or after eleven programming cycles. Finally, the tunable friction anisotropy surface was utilized as a functional platform for unidirectional transport of micro-particles. As an example, a single PDMS microsphere was unidirectionally transported for nearly 5 mm on the structured SMP surface, while no significant movement (less than 0.1 mm) was observed on the flattened surface. The structured surface can also simultaneously transport many microspheres or micro sand particles towards a desired direction. This mechanism provides a promising prospect for applications such as dry self-cleaning coatings without liquids or particles sorting or separation devices.

Kurzfassung

Einige Reptilien überraschen den Menschen mit hervorragenden tribologischen Eigenschaften in Bezug auf Adhäsion, Reibung und Verschleiß, die aus der langen Entwicklungszeit in ihrem jeweiligen Lebensumfeld stammen. Durch die Nachahmung dieser einzigartigen tribologischen Eigenschaften können Forscher von Reptilien inspirierte Oberflächen mit ähnlichen oder noch fortgeschritteneren Fähigkeiten entwickeln. Daher sind Versuche, die tribologischen Eigenschaften von Reptilien zu untersuchen und sie auf künstliche Oberflächen zu übertragen, von großer Bedeutung, um neue Lösungen für technische Probleme zu finden, die mit Reibung und Verschleiß zusammenhängen.

Nach einer kurzen Einführung in das Thema und einem kurzen Rückblick auf die angewandten Methoden befassen sich vier Kapitel dieser Arbeit mit verschiedenen Aspekten der Reptilienschuppen. Kapitel 3 konzentriert sich auf den Sandfisch (*Scincus scincus*), welcher weithin bekannt ist für seine besondere Fähigkeit, in lockerem, äolischem Sand zu schwimmen, ohne dass sich die Schuppen merklich abnutzen. Diese Arbeit charakterisiert die mikroskopischen strukturellen und tribologischen Eigenschaften einzelner Sandfischschuppen durch Rasterkraftmikroskopie (AFM) mit verschiedenen Arten von Sonden, einschließlich scharfer Siliziumspitzen, kugelförmiger Glasspitzen und Sandtrümmern. Zum Vergleich wurden auch Schlangenschuppen zusammen mit mehreren technischen Oberflächen analysiert. Die experimentelle Analyse zeigt, dass Schuppen von Sandfischen und Schlangen niedrigere Reibungskoeffizienten aufweisen als die meisten technischen Oberflächen. Jedoch sind Ihre Haft- und Abriebfestigkeitseigenschaften denen technischer Oberflächen nicht überlegen. Sandfischschuppen zeigen im Vergleich zu Schlangenschuppen keine außergewöhnlichen tribologischen Eigenschaften. Andere Gründe wie die elastischen Eigenschaften der Epidermis oder die Dynamik der Fortbewegung sollen für die beobachteten geringen Verschleißraten der Sandfischschuppen während dem „schwimmen“ durch den Sand verantwortlich sein.

Die Multifunktionalität der Schuppen aus verschiedenen Regionen der Schlangenkörper (d. h. dorsale, ventrale, und Brillenschuppen) werden im nächsten Kapitel untersucht. Die Mikroornamente auf diesen drei Arten von Schuppen war für eine Schlange sehr unterschiedlich. Die Rückenschuppen verschiedener Schlangenarten weisen unterschiedliche Mikrostrukturen auf. Jedoch zeigen die ventralen Schuppen der meisten untersuchten Schlangen sehr ähnlich ausgerichtete Mikrofibrillenstrukturen auf, und die Brillenschuppen besitzen nähende polygonartige Strukturen. Die Charakterisierung der Querschnittsarchitektur zeigt, dass gestapelte Schichtstrukturen auf Schlangenschuppen in allen Körperregionen zu finden sind. Ventrale Schuppen sind fast dreimal so dick wie Rückenschuppen derselben Schlange. Benetzbarkeit, Adhäsionskraft und spektrale Transmissionseigenschaft wurden charakterisiert und mit den Mikroornamenten auf den Schuppen korreliert. Rückenschuppen gelten als selbstreinigende Oberflächen und als Lichtstreufilter, um Schlangen vor Verunreinigungen und Sonneneinstrahlung zu schützen. Brillenschlangenschuppen opfern die Selbstreinigungsfähigkeit, um eine hohe spektrale Durchlässigkeit im sichtbaren Licht und im nahen Infrarotspektrum zu erzielen. Sie können auch schädliches Ultraviolett blockieren. Obwohl sie eine ähnliche Benetzbarkeit und spektrale Übertragungsfähigkeit wie Brillenschlangenschuppen aufweisen, werden ventrale Schuppen als Reibungskomponente zur Optimierung der Fortbewegungsleistung von Schlangen allgemein akzeptiert.

Das fünfte Kapitel untersucht die Reibungsanisotropie von Schlangen und Sandfischschuppen. Eine scharfe AFM-Spitze, die entlang der Mikrofibrillenstrukturen, auf den ventralen Schlangenschuppen, abtastet (d. h. die Nanostufen nach oben und unten, an den Fibrillenenden), zeigt eine signifikante Reibungsanisotropie. Der gleiche Effekt zeigt auch das Auf- und Abscannen der Nano-Stufenstrukturen auf dorsalen

Sandfischschuppen. Die Reibung der AFM-Spitze, die die Nanostufe nach oben abtastet, nimmt mit ihrer Stufenhöhe signifikant zu, während bei der abwärts Stufe die Zunahme nicht erkennbar ist, was zu einer Nanostufenhöhe abhängige Reibungsanisotropie führt. Eine größere Stufenhöhe verursacht normalerweise eine größere Reibungsanisotropie. Wenn die Mikrofibrillen zum Schwanz zeigen, bewegen sich Schlangen viel leichter vorwärts als rückwärts, was für sie beim Klettern von Hängen günstig ist. Der gleiche Effekt findet sich auch bei einer polymeren Nachbildung von *N. atra* ventral. Experimente mit Mikro-Tribometrie stimmen ebenfalls mit den obigen Ergebnissen überein. Interessanter ist, dass Schlangen sogar die Höhe der Nanostufen sowie die Reibungsanisotropie in verschiedenen Segmenten ihres Körpers variieren. Ein allgemeines Verteilungsmuster der Reibungsanisotropie findet sich entlang des Körpers der untersuchten Schlangen, d. h. Eine größere Reibungsanisotropie herrscht im Mittel- und Schwanzabschnitt als in den anderen Bereichen. Schlangen könnten von einem solchen Design profitieren, um während der Fortbewegung optimierte Reibungsleistungen zu erzielen.

Inspiriert von der stufenhöhenabhängigen Reibungsanisotropie auf den ventralen Schlangenschuppen, wurde in Kapitel 6 eine einstellbare anisotrope Reibungsoberfläche mit Formgedächtnispolymeren (SMPs) durch Heißprägen hergestellt. Der Formgedächtniseffekt der Polymere ermöglicht es der Oberfläche, reversibel zwischen einer abgeflachten Topographie und einer Topographie mit Mikrofibrillenstruktur umzuschalten, was zu einer einstellbaren anisotropen Reibung entlang der Mikrofibrillen führt. Die Charakterisierung mittels AFM zeigt, dass die Formänderungsfähigkeit in Bezug auf Nanostufenhöhe und Reibungsanisotropie bis zu fast 1000% bzw. 300% erreichen kann. Darüber hinaus erholt sich die SMP-Topographie kontinuierlich und kontrollierbar mit der Erwärmungszeit, wodurch sie die gewünschte Stufenhöhe und Reibungsanisotropie auf der Oberfläche erreichen kann, indem die Erwärmung vor der vollständigen Wiederherstellung abrupt beendet wird. Langzeitstabilitäts- und Wiederverwendbarkeitstests zeigen, dass in jedem beliebigen Stadium des SMP-Programmier- / Wiederherstellungszyklus die Stufenhöhe an den Mikrofibrillenenden in drei Monaten oder nach elf Programmierzyklen hochstabil ist. Schließlich wurde die einstellbare anisotrope Reibungsoberfläche als funktionelle Plattform für den unidirektionalen Transport von Mikropartikeln verwendet. Als Beispiel würde eine einzelne PDMS-Mikrokugel fast 5 mm unidirektional auf der strukturierten SMP-Oberfläche transportiert, während auf der glatten Oberfläche keine signifikante Bewegung (weniger als 0.1 mm) beobachtet wurde. Die strukturierte Oberfläche kann auch gleichzeitig viele Mikrokugeln oder Mikrosandpartikel in die gewünschte Richtung transportieren. Dieser Mechanismus bietet vielversprechende Perspektiven für Anwendungen wie trockene selbstreinigende Beschichtungen oder Partikelsortier- oder Trennvorrichtungen.

Contents

List of figures

List of tables

List of abbreviations

AFM	atomic force microscope
Al	aluminium
Cu	copper
HOPG	highly oriented pyrolytic graphite
LFM	lateral force microscopy
NOA 88	Norland Optical Adhesive 88
PDMS	polydimethylsiloxane
PEEK	polyether ether ketone
PMMA	poly(methyl methacrylate)
PTFE, Teflon	polytetrafluoroethylene
SEM	scanning electron microscope
SMP	shape memory polymer
W	tungsten
A	contact area
A_{r}	total real contact area
C_{tor}	torsional force constant
C_{z}	spring constant
E	elastic modulus
E_{keratin}	elastic modulus of keratin
E_{NOA88}	elastic modulus of NOA 88
F_{adh}	adhesive friction force
F_{fric}	friction force
F_{load}	normal load
G	torsional modulus
H	hardness
K	wear coefficient

l	length of the tip
L	length of the cantilever
m	correcting parameter for AFM force calibration
R	wear rate
s	shear strength
S_{ver}	deflection sensitivity
t	thickness of the cantilever
T	temperature
T_{hard}	transition heating temperature of shape memory polymer
T_{switch}	switching temperature of shape memory polymer
U_{ver}	setpoint
U_{dis}	threshold voltage for zero normal load
ΔU_{lat}	difference of lateral voltage
v	sliding velocity
w	width of the cantilever
W_{AA}	work of cohesion of material A
W_{AB}	work of adhesion of interface between A and B
W_{BB}	work of cohesion of material B
β	constant for calculating contact angle
γ_{A}	surface energy of material A
γ_{AB}	surface energy of interface between A and B
γ_{B}	surface energy of material B
γ_{l}	surface energy of liquid
γ_{s}	surface energy of solid
θ	contact angle
θ_{gr}	granular friction angle
μ	sliding friction coefficient
μ_{gr}	granular friction coefficient

1 Introduction

Plants and animals are well optimized for their habitat through the principle of natural evolution. Some of them are equipped with functional surfaces featuring fascinating micro- or nanostructures. For a long time, these biological functional surfaces have offered infinite inspirations to humans for addressing challenges in engineering [1-5]. Mimicking the micro- or nanostructures from nature and transferring them to industrial applications, abundant artificial products have been developed such as strong adhesive tapes inspired by the gecko feet [4, 6], self-cleaning surfaces inspired by *Lotus* leaves [7], drag reduction aircraft wings or swimming suits inspired by the shark skin [4, 8, 9], anti-slippery vehicle tires inspired by tree frog toe pads [4, 10-12] and so on. Among these biological examples, reptiles are the group of tetrapod animals in the Class Reptilia including turtles, snakes, lizards, crocodilians and some other relatives [13]. They usually enlighten researchers and engineers with fabulous tribological properties in terms of adhesion, friction, wear, and lubrication due to their special living performances optimized to their surroundings [4, 5]. In fact, a major issue we are facing is that nearly 23% of the world's energy consumption is caused by tribological contacts [14], *e.g.*, energy loss from car engines or manufacturing processes. Therefore, developing new surfaces or elements for the reduction of the tribology-induced energy loss shows a huge economic potential. Reptiles are very likely natural prototypes who hold the key to this urgent problem.

One example is *Scincus scincus*, a lizard widely known for its talent of swimming in loose, aeolian sand [15] and thereby also commonly named sandfish. Living in the deserts ranging from North Africa through the Sahara into Arabian Peninsula [16], this lizard buries itself beneath the sand to protect from predators and extreme heat. The unique ability of this lizard is that it can also "swim" under the sand for several meters with the velocities of up to 30 cm/s [17-19], making it a more captivating species if compared to other reptiles. Furthermore, although conducting this "swimming" behavior many times every day, it surprisingly exhibits no visible wear on its skin. This is very astonishing considering that the sand grains can easily scratch most technical surfaces even the hard ones like glass or steel. Fascinating tribological properties such as low friction coefficients [19-24] and high abrasion resistance [17, 19, 23, 24] were observed on dorsal sandfish skin by a granular tribometer [23]. Several attempts have been made to explore the reason for these favorable properties. Initially, the nanoscale comb-like step structures on dorsal sandfish scales were suspected to enhance tribological properties [19]. However, a recent study pointed out that the neutral glycans in the chemical composition of the sandfish scales might induce a low adhesion [25-27]. Nonetheless, these friction and wear characteristics determined by the granular friction approach were all roughly evaluated from macroscopic analysis. The tribological performance of sandfish interacting with sand particles on a tiny scale was so far not conducted. Such studies will be important for investigating the tribological properties of sandfish when the contacts of sandfish scale and sand particles reduce to micro- or even nanoscale range. Besides this, it can also further clarify the function of the nano-step structures on dorsal sandfish scales.

Snakes (Squamata: Serpentes) are the most common reptiles in nature and until now, more than 3600 species have been described [28]. In difference to most lizards, snakes have no extremities and therefore have to locomote directly in contact with the substratum via their ventral side [29-33]. In this case, ventral snake scales unavoidably endure friction and wear during locomotion, which presumably evolved interesting tribological properties. In fact, the snakes' epidermis initially interested researchers to start with the observation of the micro-ornamentations on their "Oberhäutchen" nearly 150 years ago [34]. After that, for a long time the investigations grew slowly until the scanning electron microscopy (SEM) was introduced to image the micro-dermatoglyphic patterns on the snake scales [35-43], which greatly accelerated the studies. So far, hundreds of species have been examined and various micro-ornamentations have been found and characterized. The dorsal scales of snakes display diverse ultra-structures which were particularly summarized into several types: verrucate pattern [41], canaliculate ridges [40], cristate apical pattern [38], cross-hatched pattern [39, 43], papillate pattern [37], and reticulate or porous structure [36]. These microstructures were first recognized as the ecological indicator or taxonomical tool for correlating with their habitat preferences [37, 44]. However, in difference to the dorsal scales, the majority of snakes exhibit very similar oriented, spike-shaped, longitudinal ridge structures (micro-fibril structures) on their ventral scales [45-52]. In addition, widely known among biologists, snakes do not have movable eyelids but possess two fixed and transparent scales covering their eyeballs, which are commonly called spectacle scales [53]. This type of scale is a part of the whole snake scale and molts together with the other scales from every 20 days to a year depending on respective species and its age [54, 55]. The reported studies about the microstructures on spectacle snake scales were limited and obscure in explanation [56, 57]. A more detailed analysis of the spectacle scales is needed.

The functions of the microstructures on the scales of snakes and sandfish are of high interest, especially the structures which are related to tribological abilities. The early theory proposed that the microstructures on lizard scales act as a zip-fastener for connecting the new and old skin before molting [58] and can even mechanically strengthen the scale surface [6, 59]. Then due to their diversity in types, the dorsal scales of snakes attracted more attention and were widely discussed. Several designated capabilities have been detected depending on different species, such as scattering light to reduce solar radiation penetrating into the organism [41, 60], enhancing dark coloration [61], and harvesting water [62] or self-cleaning (anti-contamination) properties [44, 63, 64]. It seems that snakes carefully decorate the scales on their back with dedicated microstructures for particular, individual demands according to their habitat. Regarding the ventral scales, previous studies state that the micro-fibril structures on snake abdomen contribute primarily to improve frictional performance, *e.g.*, reducing friction [21, 65, 66] or creating friction anisotropy [45-52]. These results are mainly obtained by two common experimental methods, *i.e.*, measuring the angle of a tilted slope where the whole body of an unconscious (anesthetized or euthanized) snake slides down [31, 32, 67, 68] or measuring the friction coefficient on molted snake scales by a tribometer [45, 50-52, 69]. The first method can evaluate the averaged frictional properties of the whole snake belly, which is similar to the frictional performance of a real snake's locomotion. Friction measurement on molted snake scales (second method) cannot achieve this but allows to characterize friction on single scales. Studies by both methods found friction anisotropy on ventral snake skins (or scales), while only a few of them correlated this frictional property to the micro-fibril structures [31, 47, 49, 52, 69]. One study conducted frictional characterization at single micro-fibril ends by atomic force microscopy (AFM) and reported friction anisotropy for the AFM tip scanning forward and backward directions [49]. Despite this, the nanoscale mechanism of friction anisotropy originating from micro-fibril structures as well as the frictional performances along the snakes' bodies has not been clearly understood. These demands recall the frictional studies at atomic-scale step edges of crystal surfaces such as graphite, MoS_2, and NaCl [70-72], which was also conducted by AFM. Such studies might provide a new method for characterizing the frictional properties of single micro-fibrils to explore the origin of friction anisotropy on snake belly. Spectacle scales serving as the window for eye lens function as a mechanical protector and a spectral filter against solar radiation [53, 73-76]. So far, high-pass for visible light but low transmission for certain infrared spectrum [73] and even cut-off in the ultraviolet spectrum [74-77] was observed on the spectacle scales of more than 60 snake species. From the tribological aspect, another possible ability that spectacle scales might possess is a self-cleaning property. Snakes travel so close to the ground with dust or other contaminations all around, but they do not have any hands or legs to wipe their eyes. Thus, their unmovable spectacle scales might be able to self-clean considering that they are important for transmitting visible lights and thereby demand a constantly clean surface. A previous study which measured the water contact angle on the spectacles of *Gekko gecko* shows an equilibrium value of less than 100° [78]. As for spectacle snake scales, however, such type of examination is rarely reported.

Consequently, it seems that the scales in different regions of snakes and sandfish feature diverse microstructures to obtain multi-functional abilities for better adapting to their habitats. Besides this, it is also interesting to note that almost all scales might display at least one type of excellent tribological capabilities concerning the adhesion, friction, and wear resistance. These characteristics make the reptile scales an ideal biological example for biomimetic applications. Moreover, if comparing between ventral snake scales and dorsal sandfish scales, one can find that the micro-fibril structures featuring a nano-step at each fibril end are closely cognate with the step structures on sandfish (see Figure 1.1). Both types of scales are in contact with substrates (snakes sliding) or sand particles (sandfish "swimming") during their locomotion. This implies similar structure-induced-friction mechanism on these two reptiles. Thus, examining the friction at these nano-steps with a "nano-tribometer" is of utmost significance for comprehending the trick of reptiles manipulating friction and further finding the key to control friction on artificial surfaces.

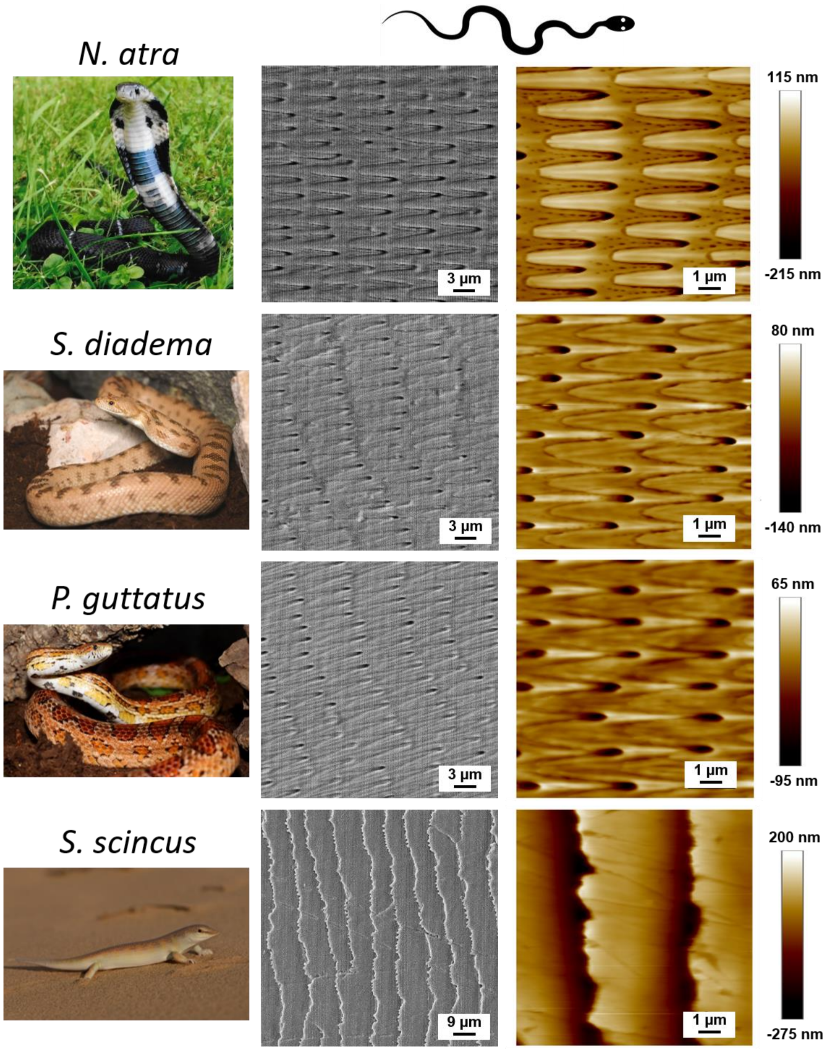

Figure 1.1: Micro-fibril and nano-step structures on ventral snake and dorsal sandfish scales. Photos of three snake species (*N. atra*, *S. diadema*, and *P. guttatus*) and sandfish (*S. scincus*) are shown in the left column. The second and third columns display their corresponding topography images obtained by the scanning electron microscopy and atomic force microscopy, respectively. Nano-steps at oriented micro-fibril ends on ventral snake scales resemble the step structures on dorsal sandfish scales. The schematic snake drawing on the top indicates the orientation of the micro-fibrils pointing towards the tail. Copyright of all snake photos is by Guillaume Gomard and of the sandfish photo by Gerrit Jan Verspui. Used with kind permission.

In addition, mimicking the nano-step structures of snake or sandfish scales and transferring their fascinating tribological properties to technical surfaces for engineering applications will be of high interest. Inspired by snakes, several artificially tribological surfaces have been designed and fabricated through replicating the arrangement of snake scales on a metal surface [66, 79] or mimicking the micro-fibril structures on the polymer [48], metal [51, 80], and even a ceramic surface [81] by different techniques. Friction coefficients on these snake-inspired artificial surfaces were found to be even lower than a flat reference of the same material, and fascinating friction anisotropy was observed in the opposite directions along the micro-fibrils. All these attempts illuminate the possibility of fabricating the microstructures of reptile scales onto technical surfaces for reducing friction or creating friction anisotropy, which will have a prospective future in industrial applications such as anti-slippery surfaces or snake-shaped robots. However, all these reported surfaces can only display a constantly reduced or anisotropic frictional performance. A more intelligent, tunable frictional surface, which possesses the ability of dynamically switching between isotropic and anisotropic friction, will open a new path for extended utilizations such as particle sorting or separation systems or dry self-cleaning coatings.

Based on all of the above, this work aims to characterize the structural and tribological properties of sandfish and snake scales in order to nail down the mechanism of their microstructure-caused tribological abilities, and make it applicable on technical surfaces for advanced tribological utilizations. Thus, the objectives of this thesis are:

1. Systematical characterization of the tribological properties of sandfish and snake scales.
2. Investigation of the function of the micro- or nanostructures existing on ventral, dorsal, and spectacle snake scales.
3. Analysis of the frictional performance of nano-step structures of ventral snake scales and dorsal sandfish scales.
4. Equipment of nano-step structures onto technical surfaces for intelligent tribological performances and exploration of their potential applications.

A series of theoretical and experimental analysis was conducted in this thesis to successfully achieve these objectives. The following chapter gives an overview of the theory as well as the methods and technical tools used in this thesis. Chapter 3 presents a comparison of the tribological properties including adhesion, friction, and abrasion resistance between sandfish scales, snake scales as well as some other technical surfaces. Next the structural properties, wettability, and spectral transmitting properties of scales from different regions of snake body are characterized and the multi-functionality of snake scales is discussed in Chapter 4. In Chapter 5 the frictional performance at the nano-step structures on ventral snake scales and dorsal sandfish scales is analyzed in detail by AFM and the nanoscale mechanism of friction anisotropy on these scales is clarified. Chapter 6 introduces the replication of the micro-fibril structures from the ventral side of snakes onto a shape memory polymer realizing a tunable friction anisotropy surface and its application for unidirectional transport of granular particles. Finally, Chapter 7 gives a summary of my study and an outlook on further possible developments.

2 Theoretical and methodological background

For the investigation of reptile scales and the employment of reptile-inspired tribological surfaces, a series of characterization, analyzation as well as fabrication processes was applied. This chapter introduces the basic theoretical and experimental methods used in this work. For the characterization of the tribological properties of reptile scales, a fundamental understanding of the tribology related theory is necessary. After that, the biological and technical samples acquired for characterization are reviewed. Finally, the relevant surface analysis tools together with the fabrication tools and techniques, which are exploited for the development of the artificially tribological surfaces, are presented.

2.1 Basis of tribology

Since Peter Jost coined the scientific name of "tribology" in 1966 to express "the science and technology of interacting surfaces in relative motion and of associated subjects and practices" [82, 83], the term became widely utilized in the field related to this topic. The invention of atomic force microscopy (AFM) [84] enabled the investigation of tribology down to nanoscale and extensive studies were conducted to find its physical origins [85-87]. Efforts were made to explore how tribology originates at the micro- or even nanoscale and inversely, how these tiny interactions eventually lead to the macroscale tribological phenomena [88]. Normally, tribology refers to a series of complicated interactions between the contacted surfaces. The study of this subject generally consists of following four aspects: adhesion, friction, wear, and lubrication [89], which are usually interconnected with each other.

2.1.1 Adhesion

Adhesion is one of the most common surface forces and different types of its definition can be found in different dictionaries. Nowadays, the most widely accepted one is described as the tendency of particles or surfaces to adhere together [90]. Adhesion is intimately related to surface energy [91], *i.e.*, the work of adhesion of material A corresponds to its surface energy by [89]:

$$W_{\mathrm{AA}} = 2\gamma_{\mathrm{A}}, \tag{2.1}$$

where W_{AA} is also called the work of cohesion and γ_{A} is the surface energy.

When material A is in contact with another material B, an energy γ_{AB} is associated with the emergence of the interface between them. The work of adhesion for this interface is defined as the variation of surface energy during the contacting process or the reversible work needed to separate them. It is labeled with W_{AB} and can be calculated from:

$$W_{\mathrm{AB}} = \gamma_{\mathrm{A}} + \gamma_{\mathrm{B}} - \gamma_{\mathrm{AB}} = \frac{1}{2}W_{\mathrm{AA}} + \frac{1}{2}W_{\mathrm{BB}} - \gamma_{\mathrm{AB}}, \tag{2.2}$$

which is called the *Dupré equation* [89]. Therefore, a conventional method to determine adhesion is to measure the surface energy.

In laboratory practice, solid surface energy can be calculated from contact angle measurements [92] by a sessile drop method. In such measurements the contact angle between the edge of liquid droplet and the sample surface is measured. Various approaches have been proposed to determine surface energy from the measured contact angle [93-95]. After a long-time development of these approaches, Kwok *et al.* [96] improved the work of Neumann *et al.* [95] and developed the so-called "equation of state":

$$\cos\theta = -1 + 2\sqrt{\frac{\gamma_\mathrm{s}}{\gamma_\mathrm{l}}}e^{-\beta(\gamma_\mathrm{l}-\gamma_\mathrm{s})^2}. \tag{2.3}$$

In this equation, θ is the contact angle between the liquid-air interface and the solid surface, γ_l and γ_s is the surface energy of liquid and solid, and β is a constant. Therefore, from Equations (2.1) and (2.3), it can be seen that low adhesion is normally a sign of low surface energy, which typically coincides with a high contact angle [88]. The setup and procedure of measuring contact angles by sessile drop method will be explained in the following Chapter 2.3.5.

Besides examining the contact angles, a much easier and more advanced method evolved with the development of the AFM. Its basic idea is to record and analyze the so-called force-distance curves of an AFM cantilever approaching and detaching from the sample surface [97]. This technique has the big advantage of directly measuring the adhesion forces or the work of adhesion by a sharp tip. The principle of determining adhesion forces with AFM will be illustrated in Chapter 2.3.1.

2.1.2 Friction

The practice of human beings exploiting friction goes as far back as to prehistoric humans using friction to start fires [89]. Normally, as soon as two objects slide against each other, friction emerges in their contact area. There are several types of friction according to different sliding conditions. In terms of the occurrence of the relative motion between the two objects, friction can be classified by static (the force needed to initiate sliding) and dynamic friction (the force needed to support sliding) [89]. Static friction is ordinarily greater than dynamic friction [89]. In the light of the existence of lubrication in the contact area, dry friction and lubricated friction are usually distinguished.

Although Leonardo da Vinci (1452-1519) has already systematically studied friction and recorded his results in his notebook [98], it was Guillaume Amontons [99] who first published the results about his study of friction in 1699, which is commonly accepted as Amontons' laws of friction:

First law of friction: The friction force is proportional to the normal load.

Second law of friction: The friction force is independent of the apparent area of contact.

Several decades after that, Charles-Augustin de Coulomb further noted that friction force is independent of the velocity. It is often referred to as [100]

Third Law of friction: Dynamic friction is independent of the relative sliding speed.

The three laws of friction can be summarized by the equation [101]:

$$F_\mathrm{fric} = \mu \cdot F_\mathrm{load}, \tag{2.4}$$

where μ is called friction coefficient, which is determined by the material properties of the surfaces. It is also influenced by the other factors such as humidity of the environment or roughness of the sliding surfaces. The friction coefficient is independent of the apparent contact area A and the sliding velocity v. F_fric and F_load represent the frictional force and normal load, respectively. Equation (2.4) works successfully in most instances for depicting friction at rubbing surfaces including both rough and smooth surfaces, both ductile and brittle contacts, as well as both macroscopic and microscopic contacts [102, 103]. However, it will become invalid in some specific cases such as large ranges of loads or sliding velocities [103], and for the contacts with strong adhesion [101, 104].

From a microscopic point of view, when two solid surfaces rub against each other, friction originates mainly via two mechanisms [89]. They comprise the adhesive friction needed to shear the contacting junctions where adhesion occurs and the plowing friction needed to plow the asperities of the harder surface through the softer surface. Among them, the adhesion contributes to friction through [89]

$$F_{\mathrm{adh}} = A_{\mathrm{r}} s. \tag{2.5}$$

F_{adh} is called adhesive friction force. A_{r} is the total real contact area between the two surfaces ($A_{\mathrm{r}} = \sum A_i$, $i = 1, 2, \ldots, \mathrm{n}$) and s is the shear strength (assumed the same for all the contacting junctions). Thus, in this case the adhesive friction is usually not independent of the real contact area.

At the interface of two contacting surfaces, the real contact area (A_{r}) consists of many small individual contacts between their surface asperities. Thus, it is typically much smaller than the apparent contact area (A). For the situation where Amontons' laws are valid, the real contact area is proportional to the applied normal load. Besides this, the hardness (H) of the sliding surfaces is also an important factor for real contact area. For plastic deformation, it can be expressed by [89]

$$A_{\mathrm{r}} \simeq \frac{F_{\mathrm{load}}}{H}. \tag{2.6}$$

Under conditions for elastic deformation, the Greenwood and Williamson model [105] is a simple method to estimate the real contact area. According to their result, the relationship between the real contact area, normal load, and the elastic modulus of the material (E) can be simplified as [89]

$$A_{\mathrm{r}} \propto \frac{F_{\mathrm{load}}}{E}. \tag{2.7}$$

Thus, from Equations (2.5) - (2.7) one can find that the adhesive friction is inversely proportional to the hardness or elastic modulus of the contacting surfaces. As an example of a hard surface sliding against a soft surface, the smaller hardness (or elastic modulus) of the soft surface will cause a more intimate contact (*i.e.* larger real contact area between two surfaces) resulting in a larger friction.

For characterizing friction forces or friction coefficients by experimental methods, a tribometer is usually used. This instrument exploits a standard, hard detector (probe) to pair against the sample surface under defined normal loads and at the same time records the corresponding lateral frictional forces. A detailed introduction of the setup and principle of the measurement by tribometry will be presented in the following Chapter 2.3.3. Additionally, as a versatile technique, AFM can also be employed to characterize friction properties especially on the micro- or nanoscale, which will be described in Chapter 2.3.1.

2.1.3 Wear

Wear is another fundamental but complex aspect of tribology. The general definition of wear refers to the surface damage such as deformation or material removal when two surfaces rub against each other [89]. Mankind benefits from wear in many cases in our daily life but also has to withstand the losses caused by it. For example, traditional manufacturing techniques such as cutting, grinding, and polishing processes take the advantage of wear to fabricate mechanical parts with high precision. However, machine or vehicle elements suffer from wear phenomena leading to functional failure, which will cause significant accidents if we do not replace them regularly.

The technical importance of wear encouraged studies on this topic [106-110]. Nevertheless, due to its multitude of complicated physical mechanisms, no universal model which can perfectly describe the wear process and explain the origin of wear occurring at the nanoscale has been developed so far. *Archard's wear equation* is a simple but practical model developed by Archard [111] to evaluate sliding wear.

$$R = \frac{KF_{\mathrm{load}}}{H}, \tag{2.8}$$

here, R is the wear rate defined as the volume of material removed per sliding distance. K is referred to as the wear coefficient, with a typical value ranging from 10^{-2} to 10^{-7} for unlubricated materials. F_{load} and H are the applied normal load and the hardness of the surface region, respectively. Based on the assumption that wear volume is proportional to the sliding distance, this model introducing wear coefficient K provides a valuable method for comparing the severity of wear between different materials [89]. From Equation (2.8) one can see that applying a larger normal load on a softer surface will cause a larger wear rate.

Another important subject in tribology is lubrication which plays a vital role for reducing friction and wear in many industrial applications. This topic, however, is behind of the scope of this thesis.

2.2 Materials

This section gives an overview of the materials and samples used in this thesis. Biological samples include molted scales from twelve different snake species as well as sandfish. Various technical materials (surfaces) such as different kinds of polymers or metals were also studied as a comparison. Besides this, shape memory polymers (SMPs) were introduced as a substrate for replicating micro-fibril structures on their surfaces to achieve smart frictional functions.

2.2.1 Biological samples

Snakes and lizards shed their scales regularly. The time period depends on the respective species and their ages [54]. This allows us to acquire abundant experimental samples without harvesting the living reptiles. In this thesis, the majority of biological samples (molted snake and sandfish scales) was provided by G. Gomard (IMT & LTI, KIT) and some sandfish scales were obtained from G. Gassner (Natural History Museum, Vienna, Austria). Snakes shed their skin as a whole piece, while sandfish molt their scales into lots of small, separated pieces.

Figure 2.1 shows the photographs of three snake species and of their corresponding molted scales. The first line illustrates the photos of snakes with their short name on the top. A segment of the cutted scales of the corresponding snakes is shown in the bottom line. The dorsal scales are on the left side of each image and the right side shows their ventral scales, as indicated in the images. The photos of spectacle snake scales will be shown in Figure 4.3 in Chapter 4.1.3. It can be seen that the dorsal and ventral scales of the same snake show very different shape and size, while the shape of the corresponding same regional scales on different snake species are very similar. The ventral scales usually have a rectangle shape with a large size. The dorsal scales are nearly circular and smaller than ventral scales. Both types of scales are closely linked by the soft tissues between single scales. The photos and molted scales of sandfish will be shown in Figure 3.1 in the following Chapter 3.1.

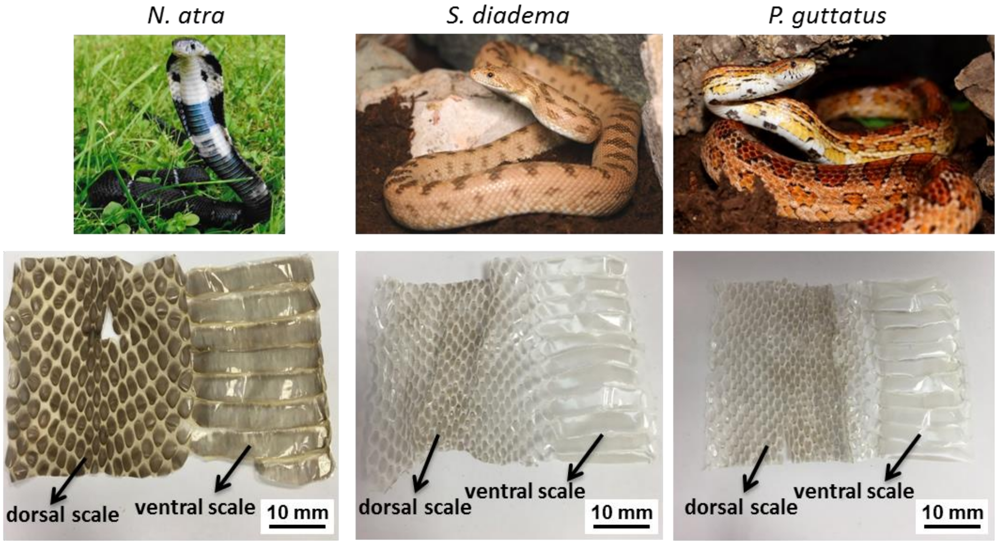

Figure 2.1: Photos of three snake species and their molted scales. The top line shows *N. atra*, *S. diadema*, and *P. guttatus* in their natural habitat. The bottom line represents their corresponding molted scales (a cutted segment). As snakes shed their scales as a whole piece, it is easy to distinguish their dorsal and ventral scales, as indicated in the images, respectively. Snake photos are taken by Guillaume Gomard and used with kind permission.

In this thesis, molted scales from twelve different snake species including 4 vipers, 3 pythons, 2 colubrids, 1 lamprophiid, 1 elapid, and 1 boa together with the scales of sandfish were examined. Table 2.1 summarizes some basic information of these biological samples such as the common name, belonging family, and living habitat, respectively [112, 113].

Table 2.1: Basic information of the investigated snake species and sandfish. Their corresponding common name, respective family, and living habitat are listed.

Species	Short name	Common name	Family	Habitat
Sistrurus miliarius barbouri	*S. miliarius*	ground rattlesnake	Viperidae	forests and swamps
Bitis arietans	*B. arietans*	puff adder	Viperidae	savannas and grasslands
Echis pyramidum	*E. pyramidum*	Northeast African carpet viper	Viperidae	grassland and rocky areas
Vipera aspis francisciredi	*V. aspis*	aspic viper	Viperidae	stony grounds and shrubby areas
Antaresia perthensis	*A. perthensis*	pygmy python	Pythonidae	savannas, shrubland and grassland
Aspidites ramsayi	*A. ramsayi*	woma python	Pythonidae	savannas, shrubland and grassland
Morelia spilota	*M. spilota*	carpet python	Pythonidae	rainforests and woodlands
Pantherophis guttatus	*P. guttatus*	corn snake	Colubridae	grass fields, forests and trees

Spalerosophis diadema cliffordii	*S. diadema*	diadem snake	Colubridae	arid and semiarid plains
Malpolon monspessulanus	*M. monpessulanus*	Montpellier snake	Lamprophiidae	shrubland and grassland
Naja atra	*N. atra*	Chinese cobra	Elapidae	woodland, shrubland and grassland
Corallus hortulanus	*C. hortulanus*	Amazon tree boa	Boidae	tropical forests, trees
Scincus scincus	*S. scincus*	sandfish	Scincidae	desert

The sandfish is a lizard native to the desert belts from northern Africa to southwestern Asia. However, most of the investigated snakes live in grasslands or forests, *i.e.*, *S. miliarius*, *B. arietans*, *E. pyramidum*, *A. perthensis*, *A. ramsayi*, *M. spilota*, *P. guttatus*, *M. monpessulanus*, *N. atra*, and *C. hortulanus*. Among them, interestingly, several species are found to be able to climb onto the trees (*A. ramsayi*, *M. spilota*, *P. guttatus*, and *C. hortulanus*). Besides in grasslands, *E. pyramidum* is also observed in the habitats of rocky areas. Similar to sandfish, *V. aspis* and *S. diadema* live in the stony or sandy environment for most of their time. Figure 2.2 shows the geographical distribution of the investigated twelve snake species and sandfish around the world [16, 112, 113].

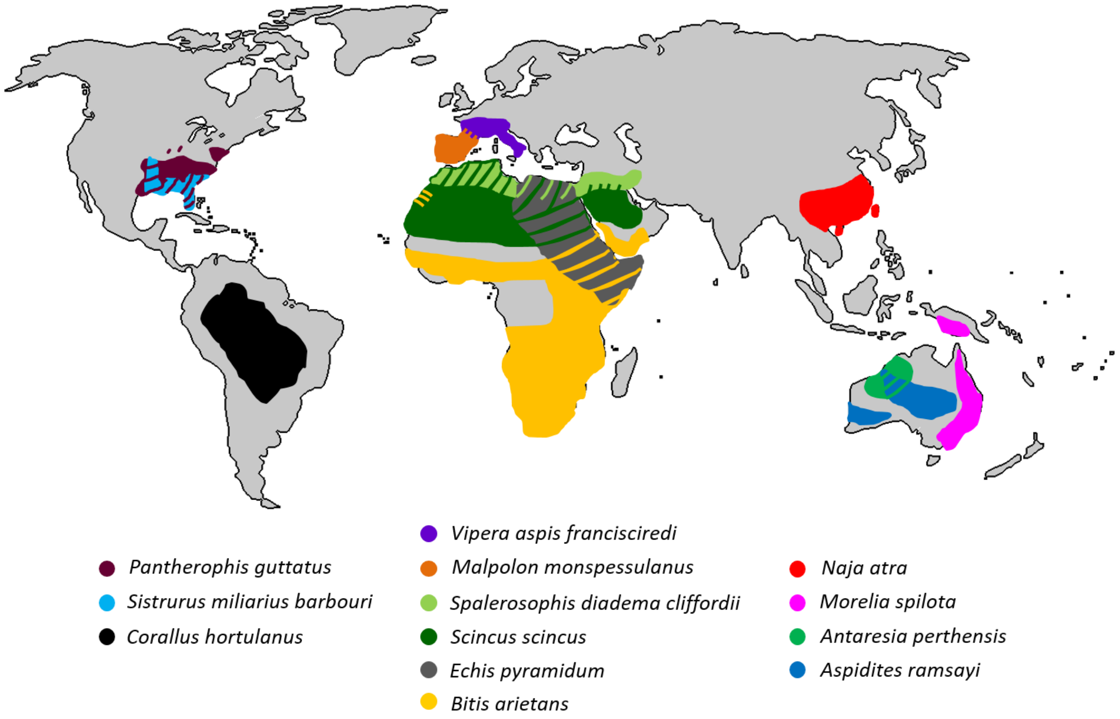

Figure 2.2: Geographical location of the investigated snake species and sandfish. The biological samples studied in this thesis are widely distributed over the five continents around the world.

All the biological samples of sandfish and snake scales were first separated into single pieces and then cut into a small size (around 10 mm × 7 mm). After that, they were carefully cleaned with high-pressure air before the experimental treatment or characterization.

2.2.2 Technical materials for friction analysis

Several technical materials including highly oriented pyrolytic graphite (HOPG), polytetrafluoroethylene (PTFE, Teflon), poly(methyl methacrylate) (PMMA), polyether ether ketone (PEEK), aluminium (Al), 100Cr6 (AISI 5210) bearing steel, and silicon were analyzed as a comparison to the biological reptile scales. Tribological properties including adhesion, friction, and wear resistance of these technical surfaces as well as sandfish and snake scales were characterized and compared. Polydimethylsiloxane (PDMS) was used as a negative mold for replicating the micro-fibril structures from ventral snake scales onto the surface of a UV-curing Norland Optical Adhesive 88 (NOA 88) via soft lithography technique.

To fabricate a smart tribological surface, shape memory polymers (SMPs) are employed as a substrate for replicating snake fibril structures. SMPs are a category of polymers which possess an ability of "memorizing" a predefined, permanent shape. With this permanent shape, they are able to be further manipulated into a temporary shape (programming process) and then change their shape back to the memorized permanent shape (recovery process) if triggered by an external stimulus such as light or heat [114-117]. Other recovery trigger mechanisms such as electric [118] and magnetic [119] excitation or humidity [120, 121] were also reported by recent studies [122, 123]. The general shape-changing principle of SMPs is caused by the two individual domains in their compositions, which are called hard segments (netpoints) and switching segments, respectively. Under the state of their original permanent shape, netpoints are linked together by the switching segments. In terms of thermoplastic SMPs, this state (permanent shape) can be defined while synthesizing or redefined after fabrication by melting them with a temperature of over their transition heating temperature (T_{hard}). After cooling down to room temperature, the SMPs are settled into their permanent shape. To further program them into a temporary shape, a temperature between the switching temperature (T_{switch}) and T_{hard} ($T_{\mathrm{switch}} < T_{\mathrm{hard}}$) is demanded to deform the switching segments but does not affect the hard segments. After deformation, cooling the polymer to the temperature below T_{switch} leads to a temporary shape. This shape will be constantly stable as long as its surrounding temperature is lower than T_{switch}. A recovery process of SMPs gradually switching back to their original permanent shape will happen only if the polymer is heated to or above T_{switch}.

Compared to shape memory alloys, SMPs exhibit many advantages such as high flexibility, easy processing, high shape changing capability, low cost and weight. Previous studies on this material indicate great potential for diverse applications in sensors, actuators, and smart devices [114, 124, 125]. More specifically, SMPs can play a promising role as switchable/recoverable optical elements [126-128], self-healing materials [129], biodegradable wound suture fibers [130], and self-peeling dry adhesive [131-133] in both industry and our daily life. Thus, it will be interesting to adapt the functional microstructures of snakes or sandfish onto SMPs to achieve tunable tribological properties for various applications. The SMPs utilized in this thesis are the thermally triggered cycloaliphatic polyether urethane block copolymer Tecoflex® EG-72D (Lubrizol, USA). Their hard segments are composed of 1,4-butanediol (1,4-BD) and 1-isocyanato-4-[(4-isocyanatocyclo-hexyl)methyl] cyclohexane ($H_{12}MDI$) with a high transition temperature of $T_{\mathrm{hard}} \approx 150\ ^{\circ}\mathrm{C}$. Their switching segments are combined with poly(tetramethylene ether) glycol (PTMEG) plus $H_{12}MDI$, which have a switching temperature range of $T_{\mathrm{switch}} \approx$ 40 °C - 70 °C [127]. All the biological and technical samples in this thesis were stored and measured in a temperature (21 °C - 23 °C) and humidity (50% - 70%) controlled environment.

2.3 Tools and techniques for surface analysis

To characterize the topographical, tribological, and spectral properties of the above mentioned biological and technical samples, a series of tools and techniques for analyzing their surfaces were employed in this thesis. This section gives a brief overview of their basic working principles and the advantages in their corresponding utilizations.

2.3.1 Atomic force microscopy (AFM)

Since its invention in 1986 [84], AFM has become one of the most indispensable and versatile tools for nanoscale imaging and the tribology-related analysis. Besides generating 3D topographical images with atomic resolution, this technique can also provide various other functions such as measuring contact (adhesion) or lateral forces (friction) [86, 134]. In this work, AFM was widely exploited to characterize the topography, adhesion, friction, and wear resistant properties of many sample surfaces including both biological reptile scales and technical surfaces. All the AFM experiments were conducted with a Dimension Icon AFM (Veeco Inc., USA). The AFM cantilevers for detecting the surfaces comprise commercial products (All-in-one-Al, BudgetSensors) as well as artificially fabricated customized probes. A schematic image of the working principle of the typical AFM measurement is illustrated in Figure 2.3.

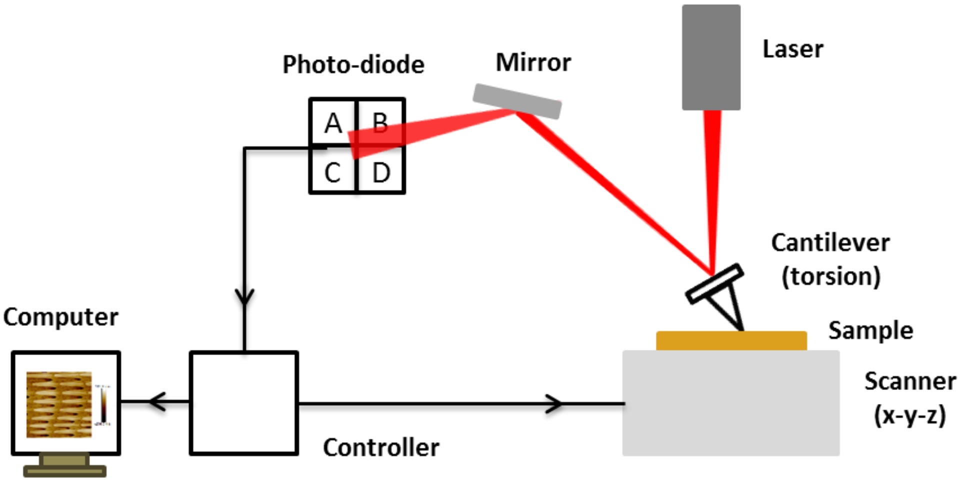

Figure 2.3: Schematic image of AFM measurements. A cantilever with a sharp tip at the end interacts with the sample surface (located on a movable stage) to detect its topographical or frictional information. The laser focused on the backside of the cantilever records the bending (topography) or twisting (friction) of the cantilever. After that, the laser with detected signals is guided into a photo-diode and finally visualized by a screen. Figure adapted from [135].

The basic idea of AFM measurements is to utilize the laser beam to detect the deformation of the cantilever such as deflection or torsion when it interacts with the sample surfaces. A sharp, pyramid structured tip exists at the cantilever end for sensing the expected information (*i.e.* topography, adhesion, or friction) of the sample surface. Before starting a measurement, the sample under investigation is placed on a controlled x-y-z scanner and the cantilever is amounted above the sample. The laser beam is set to directly focus onto the backside of the cantilever tip and the reflected laser is calibrated at the center of the photo-diode (Figure 2.4 a). Once the measurement starts, the cantilever tip is gradually brought into contact with the sample surface and subsequently scans over the surface (contact mode) or oscillates above the surface to measure the amplitude (tapping mode). For topography measurements, the deflection (bending) of the cantilever is recorded by the vertical movement of the reflected laser beam on the photo-diode (Figure 2.4 b). For friction measurements, the torsion (twisting) of the cantilever is measured, which is displayed as the lateral movement of the reflected laser beam on the photo-diode (Figure 2.4 c). This type of AFM measurement is also called lateral force microscopy (LFM). The detected signal from the photo-diode goes into a controller and is converted to the visualized results on a screen.

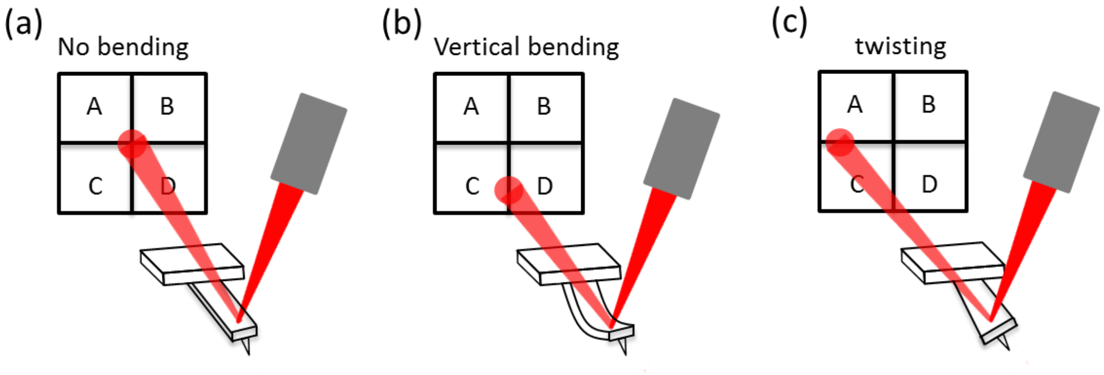

Figure 2.4: Illustration of cantilever deformation leading to a displacement of laser on the photo-diode. The laser is reflected on the cantilever backside to the photo-diode. (a) Before the deformation of cantilever, the laser was calibrated at the central position of the photo-diode. (b) The laser moves down with the cantilever vertically bending. (c) The twisting of the cantilever causes the laser moving to the left. Figure adapted from [134].

The principle of AFM measuring friction is based on the lateral twisting of the cantilever. When a cantilever is laterally scanning over a sample surface, its torsion is different in the opposite scanning directions (left scanning or right scanning). Even on a flat, homogeneous sample this difference exists in magnitude and probably the sign of the signal [134]. As shown in Figure 2.5, when the AFM tip scans from a low friction area to a high friction area, the torsion of the cantilever will increase leading to a higher lateral signal. This will also happen when the scanning direction reverses. Each cycle of the trace and retrace scanning is the so-called friction loop [85]. From an overall of view, the torsion difference in the two opposite scanning directions on the high friction area is larger than that on the low friction one. Therefore, the friction on the surface can be evaluated and compared by calculating the difference of the torsion signals between the forward and backward scans (in a friction loop).

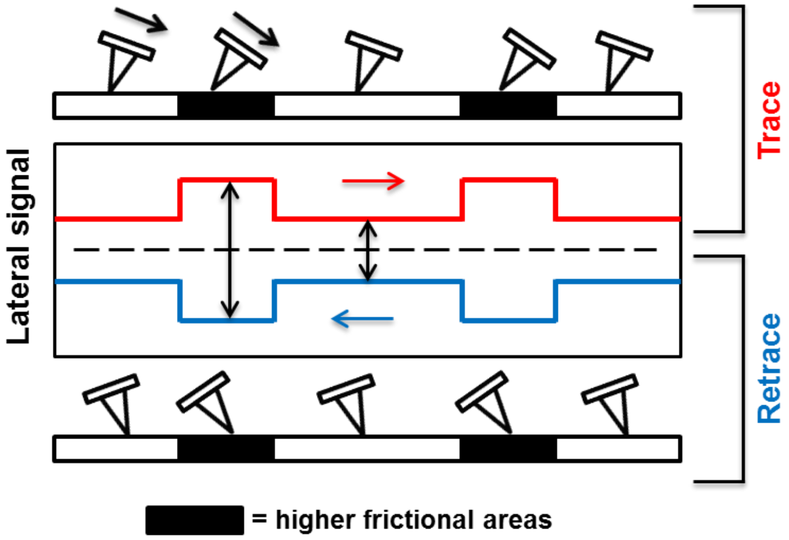

Figure 2.5: Schematic of the principle of measuring friction by AFM. The black areas represent the regions with higher friction than the white areas. When the AFM tip scans from the low friction area to the high friction area, the tip will twist more, and a higher lateral signal will be recorded. Calculating the difference of lateral signals between trace and retrace directions, the friction on these two areas can be evaluated and compared. Figure adapted from [134].

Before starting the friction measurement, a force calibration procedure [136] needs to be introduced to convert the deformation signals (deflection and torsion) of the AFM cantilever to the corresponding force signals (normal load and friction). So far, several force calibration methods [136-140] have been proposed. In this thesis, the calibration procedure from [140] was adopted. According to this method, the deflection sensitivity and spring constant of the cantilever are the crucial parameters for calibrating the forces. With them the normal load and friction force can be calculated as

$$F_{\mathrm{load}} = (C_{\mathrm{z}}/S_{\mathrm{ver}})(U_{\mathrm{ver}} - U_{\mathrm{dis}}) \tag{2.9}$$

and

$$F_{\mathrm{fric}} = \left(\frac{3C_{\mathrm{tor}}}{4L^2 l}\right)\left(\frac{1}{mS_{\mathrm{ver}}}\right)(\Delta U_{\mathrm{lat}}), \tag{2.10}$$

respectively. U_{ver} is called “setpoint” which can be manually set during the AFM measurement. U_{dis} is a threshold voltage at which the normal load is calibrated to be zero. ΔU_{lat} is the voltage difference of the AFM measured lateral signal in trace and retrace directions. S_{ver} is the deflection sensitivity of the employed cantilever. m is a correcting parameter of the displacement dependent voltage between the laser moving in vertical and lateral directions in the photo-diode. C_{z} and C_{tor} are the spring constant and torsional force constant of the cantilever. L is the length of the cantilever and l is the length of the tip at the cantilever end. For a rectangular cantilever with the length L, the width w, the thickness t, Young’s modulus E, and torsional modulus G, C_{z} is given by

$$C_{\mathrm{z}} = \frac{Et^3 w}{4L^3}. \tag{2.11}$$

Under the condition $t \ll w$, the torsional force constant is

$$C_{\mathrm{tor}} = \frac{Gwt^3}{3}. \tag{2.12}$$

Together with Equations (2.10) - (2.12), the friction force can be rewritten as

$$F_{\mathrm{fric}} = \left(\frac{GL}{El} C_{\mathrm{z}}\right)\left(\frac{1}{mS_{\mathrm{ver}}}\right)(\Delta U_{\mathrm{lat}}). \tag{2.13}$$

In this thesis, $E = 1.69 \times 10^{11}\ \mathrm{N/m^2}$ and $G = 5.09 \times 10^{10}\ \mathrm{N/m^2}$ are taken from [140]. L and l are adopt from the BudgetSensors$^{@}$ [141] (for commercial cantilevers) or characterized by the scanning electron microscope (SEM) for customized probes. m is calibrated by the experimental method similar to in [140]. S_{ver}, C_{z}, and U_{dis} are determined with the thermal tune method integrated into the corresponding AFM software before every measurement. ΔU_{lat} is calculated from the AFM measurement results (“Friction-trace” and “Friction-retrace” signal in the corresponding AFM panel). With all these parameters settled, the normal load and its corresponding friction force during the AFM cantilever laterally scanning on the investigated sample surfaces can be calibrated. For the measurement on each sample, the obtained friction force is plotted as a function of the applied normal load. The friction coefficient can be determined by conducting a linear fit between them and calculating the slope.

Besides imaging surface topography and friction, the AFM setup can also measure the adhesion through recording a so-called force-distance curve [142]. For that, the cantilever is fixed in x and y position while ramped in the z direction. The force between the cantilever tip and sample surface is calculated according to the spring constant and the deflection sensitivity of the cantilever as the tip approaches towards or retracts from the sample surface. Figure 2.6 illustrates a theoretical force-distance curve which demonstrates an adhesion force measurement of a pyramidal shaped tip at the end of an AFM cantilever interacting with a flat sample surface.

During the movement from A to B, the AFM tip is approaching but relaxed over the sample surface. With the tip going down to the surface at B, it is pulled onto the surface by the attractive forces (*e.g.* van der Waals forces) between the tip and sample surface. This behavior is also called "snap-in". After this, the force becomes repulsive as the tip continues to move down until reaching a defined end point C. This causes a linear deflection of the cantilever. Then the moving direction reverses and the tip starts to retract from the surface until at point D a "snap-out" occurs because the force applied to the cantilever overcomes the tip-sample adhesion. In this process the cantilever experiences another linear deflection in the opposite direction. Finally, the tip moves up to its original point A and a cycle of the adhesion measurement is finished. The approaching process from A to C is called the "trace" (marked in blue), and the retraction from C to A is called the "retrace" (marked in red). The slope of the linear deflection in retrace direction is the deflection sensitivity of the cantilever (S_{ver}). The force difference between the maximum point D and the relaxed point A is the measured adhesion force. If the recorded signal is expressed by voltage, the difference between point D and A will be the U_{dis}.

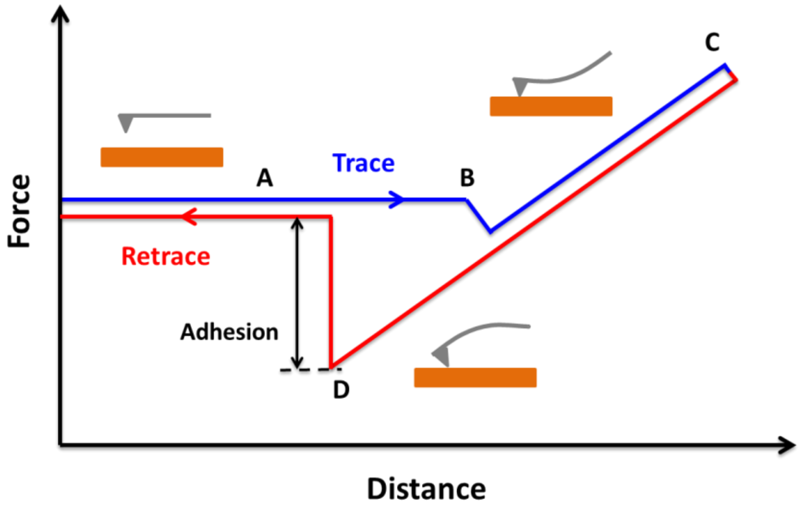

Figure 2.6: A theoretical force-distance curve shows an AFM tip measuring adhesion. The force on a sharp AFM tip changes as it approaches towards or retracts from a flat sample surface, into a typical force curve shape. The adhesion is evaluated as the maximum force required to retract the cantilever tip from the sample surface (at D point). Normally, when the cantilever is relaxed above the sample surface (A point), the force on the cantilever is initialized as zero (in both trace and retrace directions). This means that the horizontal part of the red and blue line is very close to each other, which represents the zero force. Figure adapted from [142].

To investigate the wear resistant performance of different samples by AFM, an abrasion resistant measurement with a hard AFM cantilever (*i.e.* high spring constant) is designed. The whole experimental procedure is very similar to the friction measurement except that the normal load applied on the sample surfaces was set to be very large for the aim of obtaining scratches (*i.e.* wear) on the surface. First, a small, defined area of the sample surface was scratched with a large normal load. After that, the topography of a large area was measured at the same position but with a reduced normal load (no observable wear). This allows to evaluate the volume of the removed materials (wear volume) by determining the scratching depth as well as the size of the defined scratching area. On each scratching area, the applied normal load and the conducted scratching time (distance) can be flexibly adjusted. With the same-sized scratching area, scratching depth is analyzed according to the variation of normal load or scratching time. The results are compared between different samples under investigation. A detailed abrasion resistant measurement on different samples will be designed and introduced in the following Chapter 3.5. To avoid the influence of the tip wear on the results, every experiment was started with a virgin cantilever with a fresh tip. Throughout this thesis, the topography of the sample surfaces was measured in tapping mode, while the adhesion, friction, and wear analysis were all conducted in contact mode.

2.3.2 Scanning electron microscopy (SEM)

SEM is another practical technique for examining surface topography or even cross section of the inner-structures of the samples [143]. It images surface by exploiting a focused beam of high energy electrons scanning over the investigated samples. Normally, the samples are placed and observed in high vacuum condition. Due to the electron-sample interactions, secondary electrons are excited by the electron beam from the atoms on the sample surface. SEM detectors collect these secondary electrons to image the surface information such as topography or chemical composition. Due to the advantage of using electrons, it can achieve the imaging resolution of single nanometers. However, this special working principle may also lead to imaging artifacts when measuring non-conductive samples because of the charging effects. The typical method to solve this problem is to sputter-coat a uniform layer of conductive metal such as gold or silver on the sample surfaces before SEM imaging. This procedure, however, in many cases prevents the further characterization or application of the surfaces afterwards. Another disadvantage of SEM is that it cannot directly deliver height information because images are usually taken from the top view. The examination of tilted surfaces allows the measurement of heights but this needs subsequent geometrical analysis. SEM can also be used to characterize the cross sections of the inner-structure of the samples by tilting the substrate during the measurement. Before this type of measurement, the samples are usually cut leaving a fresh edge for imaging. To obtain an optimized cross section, the samples are first frozen by liquid nitrogen and then cut by a sharp razor blade.

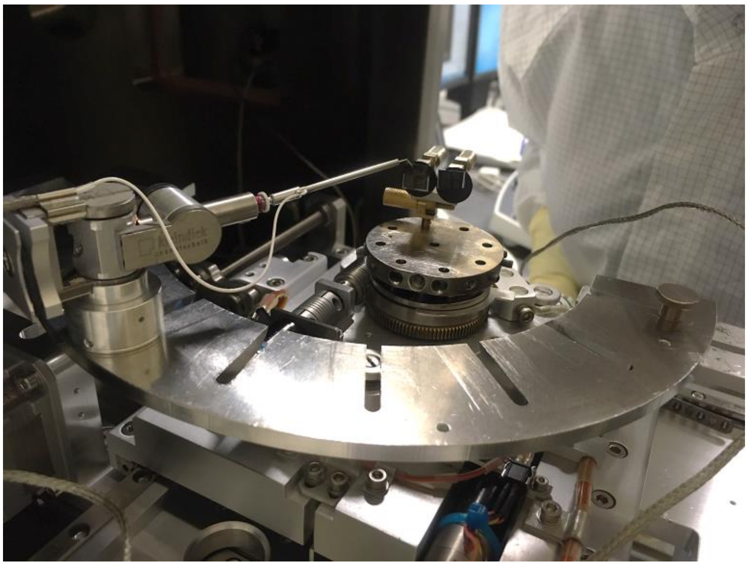

Figure 2.7: Setup for the micro-needle manipulation experiments in SEM. A micro-needle was mounted onto the stage and operated to interact with the sample surface. The whole setup was put into a high vacuum chamber and the manipulation process was observed under SEM investigation.

Besides imaging topography and cross sections, I also conducted a micro-manipulation experiment (see Chapter 5.4.2) with a micro-needle manipulator in SEM, which is accomplished with the help of Sanaz Rastjoo (IMT, KIT). Figure 2.7 shows a photo of the whole setup before it was put into the SEM vacuum chamber. The samples were vertically fixed on the stage with a conductive tape. A flexible, motion-controlled manipulator (micro-needle) was placed close to the sample surfaces with another end also fixed on the stage. Once all of these were prepared, the manipulation experiment can be started after putting the whole setup into SEM chamber and evacuating the chamber. The manipulator can be controlled to achieve several operations on the sample surface such as scratching on the surface, pushing the microstructures from the side view, and even bending the samples from the bottom. The whole manipulation process was imaged and recorded through SEM detector. All the SEM investigations in this thesis were conducted with a SUPRA 60 VP SEM from Zeiss, Germany.

2.3.3 Micro-tribometer

Besides nanoscale friction measurement by AFM, the frictional properties of different materials (both biological and technical surfaces) were also examined on the microscale with a home-built micro-tribometer (Christian Greiner's group, IAM, KIT), which is based on a reciprocating linear ball-on-plate setup [144, 145]. To measure friction, a polished sapphire sphere from Saphirwerk AG (Brügg, Switzerland) was utilized to pair against the investigated sample surfaces with a defined normal load which was applied by various standard weights. The lateral (friction) forces on the sphere during its travelling across the sample surface were detected and recorded with a strain gauge-based system. The friction coefficients were calculated and visualized by a custom-programmed LabView (National Instruments, Austin, USA) code. The measurement parameters including the sphere size (diameter), applied normal load, sliding speed and stroke, and the reciprocating cycle are adjustable, and can be set to appropriate values according to the requirements of the investigated sample surfaces (*e.g.* size or hardness). The whole setup is located on a vibration-absorptive platform and protected by a transparent cover with temperature and humidity controlling systems inside.

Normally, the friction coefficient of the sample surface is calculated as the average of the values measured from both trace and retrace directions of the sphere reciprocating cycles. Results obtained with the same sphere and normal load are compared between different surfaces. However, to characterize the friction anisotropy in the opposite directions of the same surface, the reciprocating measurement is conducted on two sample orientations (before and after the sample was turned 180 degrees). In this case, the friction coefficients in the same sample-tribometer relative moving direction are averaged to eliminate the friction deviation of the micro-tribometer in trace and retrace directions. More details of the micro-tribometer measuring friction anisotropy will be shown in the following Chapter 5.2.2.

2.3.4 Contact angle goniometer

As already mentioned in Chapter 2.1.1, contact angle measurement is an easy and practical method to determine the surface energy as well as adhesion force of solid materials. A contact angle goniometer allows this measurement on various surfaces including both biological and technical samples. To conduct such a measurement, the sample under investigation is first horizontally placed on a motion-controlled platform (x, y, and z direction). Then a liquid droplet with defined volumes is dispensed on the sample surface and at the same time the contour of liquid and sample surface is extracted and analyzed. The droplet is illuminated from the backside and recorded by a camera during the whole process. A movie sequence or a single image can be optioned with the extracted contour. Finally, the contact angle can be calculated by properly fitting the contour. In this thesis, deionized water droplets were utilized. An actuator driven syringe was used to control the precise volume and dispensing velocity of the required water droplet. All the contact angle measurements throughout this thesis were conducted with an OCA 40 system, and the contact angle values were calculated by the corresponding SCA20 software (DataPhysics Instruments, Germany) with the Young-Laplace fitting method.

2.3.5 Spectrophotometer

Spectrophotometry is a common tool for quantifying the spectral properties of samples interacting with light. In this work, spectral transmittances of snake spectacle scales together with its ventral and dorsal scales were characterized and compared. For this, A LAMBDA 1050 Ultraviolet-Visible-Near Infrared (UV-VIS-NIR) spectrophotometer (PerkinElmer Inc., USA) was employed. The deuterium and tungsten light sources equipped in this spectrophotometer are able to be calibrated to emit light spectrum in the range of from 175 nm to 3300 nm. In addition, the emitted light can be regulated into a circle or rectangle shape with an adjustable beam spot size of 2 mm - 4 mm. The highly reflective integrating sphere allows the measurement of the total (diffusive and specular) transmittance or reflectance of the investigated samples, which depends on the location of the sample surface relative to the photodetector of the spectrophotometer.

To measure the transmittances, the sample (snake scale) was amounted onto a sample holder at the entrance of the integrating sphere. After that, the light source was calibrated and then guided to the center of the sample surface. This also minimizes the influence of the sample edges on the results because the spectacle scales of snakes are normally in comparable size (diameter of about 4 mm - 5 mm) with the beam spot. For all the measurements in this work, the characterized spectrum range was set to 300 nm - 1200 nm. The data recording resolution was 2 nm. The beam spot was regulated into a circle shape and set to the minimum size (about 2 mm).

2.4 Fabrication tools and techniques

The AFM cantilevers mentioned before are usually equipped with a sharp tip at their end, which were purchased from BudgetSensors$^{@}$ (Sofia, Bulgaria). However, in some cases measurements of contacts between sample surfaces and some special substances are demanded. Thus, customized probes at AFM cantilever ends are necessary. One of the advantages of AFM technique is that its cantilever tip can be interchanged with tips like grafted debris or spheres [146, 147] to achieve desirable contacts between probes and sample surfaces. In this thesis, micro-objects including glass spheres and sand debris were glued to the end of a commercial tipless AFM cantilever (BudgetSensors$^{@}$) by our home-built manipulation setup for the investigation of the adhesion forces between these probes and sample surfaces (*e.g.* sandfish scales).

Additionally, this section also introduces several replicating techniques for fabricating the micro-fibril structures of ventral snake scales onto different polymeric surfaces. Soft lithography and hot embossing are presented according to the different replicating parameters (*e.g.* temperatures and pressures) required to imprint the aimed polymers. Before conducting the hot embossing procedures, an electro-plating technique was employed beforehand to fabricate a mold insert for the replication.

2.4.1 Fabrication of various AFM probes

Figure 2.8 shows the photo of the setup for grafting debris or spheres onto a cantilever end. Before starting the transfer process, all the necessary samples including the prepared two-component glue, isopropanol, silica spheres or sand debris, and the tipless AFM cantilever are placed on a glass slide from left to right. Then the glass slide is carefully amounted to the manipulation stage which is under the observation of an optical microscope. In front of the manipulation stage, a micro-needle with an extremely sharp tip (about 10 µm diameter at the end) is utilized to conduct the transfer procedures.

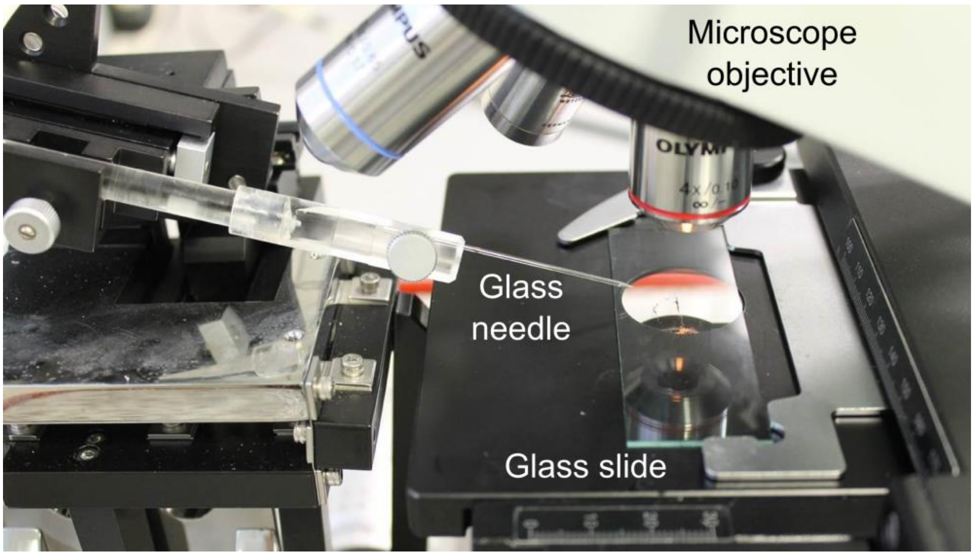

Figure 2.8: Photo of our home-built micro-manipulation setup for grafting AFM probes. Customized AFM probes with glass sphere or sand debris as the tip were fabricated through a glass needle transferring the desired particles onto a tipless cantilever end. The glass needle and the manipulation stage are freely movable in x-y-z directions. The whole grafting procedure was observed under an optical microscope with various magnifications (4×, 20×, and 40×). Figure adapted from [148].

The two components of the glue were mixed in advance, which has a drying time of around 90 minutes. A tiny droplet of the glue mixture was deposited on the glass slide. The isopropanol was prepared to clean the contaminated micro-manipulator needle tip. The micron-sized sand debris was selected after breaking the sand particle by a plier. The silica spheres (diameter ranging from 20 µm to 40 µm) were in an isopropanol solution and after the evaporation of isopropanol solution left the spheres on the glass slide. The tipless AFM cantilevers were purchased from BudgetSensors$^{@}$.

Once everything is prepared properly, the transfer (graft) procedure can be started. First, the needle tip is moved to the two-component glue and a tiny amount of glue is cautiously picked up. Then the needle tip with glue goes to the tipless cantilever and gets contact with the cantilever end leaving some glue on the position where the micro-objects (silica spheres or sand debris) will be released. After this, the manipulator needle is brought into the isopropanol to get rid of the contamination (glue) on that. Subsequently, the needle tip can be moved to the micro-objects and collect either a silica sphere or a sand debris. With this micro-object the needle goes to the tipless cantilever again and releases it in the area with glue on the cantilever. The needle is retracted after the position of the micro-object on the cantilever is desirable. Finally, the grafted probes are collected after the glue is totally cured. All these manipulating operations are observed with an optical microscope.

Besides this, chemical modification such as sputtering a layer of metal [149] or polymer [150, 151] onto the cantilever tips is another method to create probes with different surface energies for adhesion measurements by AFM. In this thesis, copper (Cu) or tungsten (W) is sputter-coated on the spherical probes with a thickness of about 50 nm to obtain such probes. Figure 2.9 shows the SEM images of the various probes used in this thesis including a sharp tip cantilever, a sand debris probe, a silica sphere probe, and a Cu-coated silica sphere probe, respectively. All these probes will be used in Chapter 3.3 to characterize the adhesion properties of sandfish scales, while in the other AFM measurements (*e.g*. friction and wear characterization) a sharp silicon tip is usually adopted.

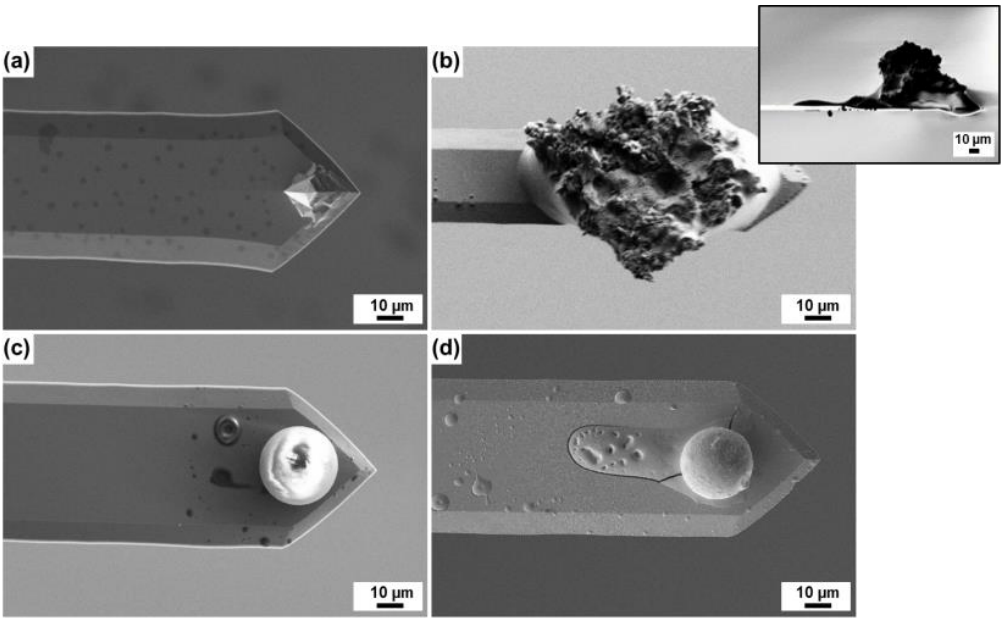

Figure 2.9: SEM images of the various AFM probes utilized in this thesis. (a) A sharp silicon tip of a conventional AFM cantilever. (b) A sand probe with sand debris glued on a tipless cantilever end. The inset image shows a side view of the same probe. (c) A silica sphere probe with a glass sphere glued to the cantilever end. (d) A copper coated silica sphere probe.

2.4.2 Soft lithography technique

Polymer replication techniques allow manufacturing and repeatedly reshaping polymers with desired microstructures on their surfaces. For the polymers which do not require high temperatures and pressures during their reshaping process, a soft lithography technique using a polydimethylsiloxane (PDMS) mold is introduced [152-154]. The micro-fibril structures of Chinese cobra ventral scale are replicated onto a UV-curing polymer layer (Norland Optical Adhesive 88, NOA 88). A schematic diagram of the replication process is displayed in Figure 2.10.

First, the snake scale (Figure 2.10 a) is cut into a rectangle shape (around 10 mm × 7 mm) and glued on a silicon wafer with a double-sided adhesive tape. Then the wafer with snake scale on the surface is place into an aluminum container. A mixture of Sylgard Silicone Elastomer 184 and Sylgard Curing Agent 184, which is mixed by a weight ratio of 10:1, is stirred evenly and placed into an evacuated desiccator for 20 min for the purpose of removing the air bubbles introduced during the stirring process. After that, the mixture is slowly poured over the snake scale (Figure 2.10 b) in the aluminum container. Subsequently, the aluminum container together with the inside mixture and snake scales is carefully placed on a hotplate. After curing for 10 hours under a constant temperature of 45 °C, which is chosen to prevent the snake scales from damaging, the hardened PDMS mold (Figure 2.10 c) is separated from the snake scale and then cleaned by an ultrasonic bath with isopropanol to remove the scale remnants. The whole curing process is conducted without applying any pressure. A droplet (around 50 µL) of UV-curing adhesive NOA 88 is dripped on a glass slide and afterwards the cleaned PDMS mold is carefully pressed into the droplet to avoid introducing air bubbles on the resulted replica (Figure 2.10 d). After exposure under UV light at 1.5 $\mathrm{mW \cdot cm^{-2}}$ UV radiation power for about 20 min, the NOA 88 polymer is cured and the replica with snake micro-fibril structures on the surface is obtained (Figure 2.10 e) after separating the PDMS stamp. The replication quality is finally checked by AFM.

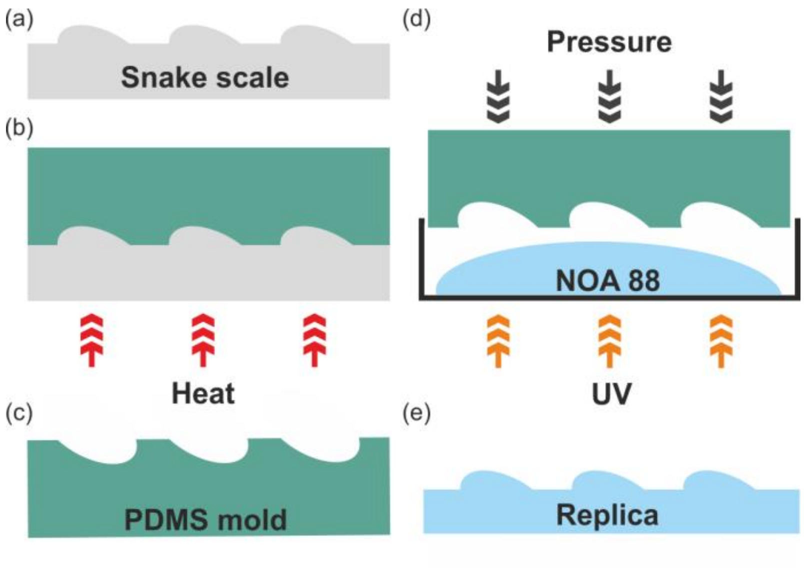

Figure 2.10: Schematic image of the soft lithography process. The micro-fibril structures on the ventral scales of Chinese cobra are replicated to a polymeric NOA 88 surface with a PDMS mold. (a) Snake scale with micro-fibril structures on the surface. (b) The mixture of Sylgard Silicone Elastomer 184 and Sylgard Curing Agent 184 is poured onto the scale surface. (c) After hardening on a hot plate at 45 °C for 10 hours, the PDMS mold is peeled off from the snake scale. (d) The obtained PDMS mold is pressed into a NOA 88 droplet, which will be subsequently cured with UV light. (e) Finally, the polymeric replica with a micro-fibril structured surface is acquired.

2.4.3 Electro-plating technique

For those polymers which need high temperature as well as high pressure during the replication process, the hot embossing technique is utilized. To replicate the micro-fibril structures of ventral snake scales onto the surface of SMPs by hot embossing, temperature of more than 150 °C and force of several kilo-newtons are applied. The PDMS mold used in the soft lithography technique is not applicable anymore. Thus, a new mold insert (Nickel shim) with the negative pattern of the desired structures, which can also withstand high temperatures and pressures, should be fabricated. The success of the replication depends on the mold quality even more than on the actual hot embossing steps. To fabricate such a mold insert, the electro-plating technique is introduced.

The ventral scale of Chinese cobra (*N. atra*) is chosen as a biological sample, from which the micro-fibril structures are replicated onto the SMP surface. First, the molted snake scales are cut into small pieces (around 10 mm × 7 mm) and cleaned with pressurized air for about 5 s to blow off the contaminations on the surface. Prepared snake scales are carefully fixed on the center of a silicon wafer by a two-component glue. Then the wafer with snake scales is evaporated with full metallization method by first 8 nm of chromium (adhesive layer) and afterwards 40 nm of gold (conductive plating base). Before the start of plating, the metal evaporated substrate is artificially masked around its edges by nonconductive tapes, leaving the central area an 85 mm diameter circular plating window. This defines the resulting electro-plated shim size. Subsequently, the masked substrate is mounted to a special plating holder and immersed into the electroplating system with boric acid containing nickel sulfamate electrolyte (T = 52 °C, pH ranging from 3.4 to 3.6), which is developed especially for nickel electroforming of micro- and nanostructures [155]. During the plating process, a gradual increasement of the current density from 0.1 $\text{A}\cdot\text{dm}^{-2}$ to 1 $\text{A}\cdot\text{dm}^{-2}$ is conducted to allow the nickel to slowly cover the snake scales, resulting in a stiff homogenous, free-defect nickel layer with a thickness of about 600 µm. Such a Nickel shim is able to repeatedly endure huge forces (several tens of kilo-newtons) for hundreds of times in the following hot embossing process. After the plating, the substrate silicon wafer is removed by dissolving it in 30% KOH solution. Snake scales and the glue is dissolved with chloroform in an ultrasonic bath (40 °C, 30 min). Finally, the obtained Nickel shim is mechanically cut into 78 mm diameter and cleaned by oxygen plasma (STP2020, R3T, Germany) for 60 min at 22 °C, 800 W, 450 mTorr. The electro-plating process was kindly conducted by Markus Guttmann's group, IMT, KIT. The cutting and cleaning of the Nickel shim was accomplished with the help of Alexandra Moritz and Uwe Köhler, IMT, KIT.

2.4.4 Hot embossing technique

Hot embossing is a versatile technique to fabricate microstructures on the surfaces of thermoplastic polymers and several other materials such as bulk metallic glasses [156] or ceramics [157]. The fundamental working principle of this technique is to press a hot mold insert into the sample surface with a constant pressure and temperature until the melt sample completely flows into the mold's cavities and solidifies after cooling. To achieve this, a hot embossing machine generally consists of one fixed and one vertically movement-controllable plate. The fixed plate at the bottom serves as a substrate. The movable plate on the top exhibits a stamp mounted with a metallic insert mold (*e.g.* Nickel shim) which contains the negative desired microstructures. Both plates can be precisely heated and cooled.

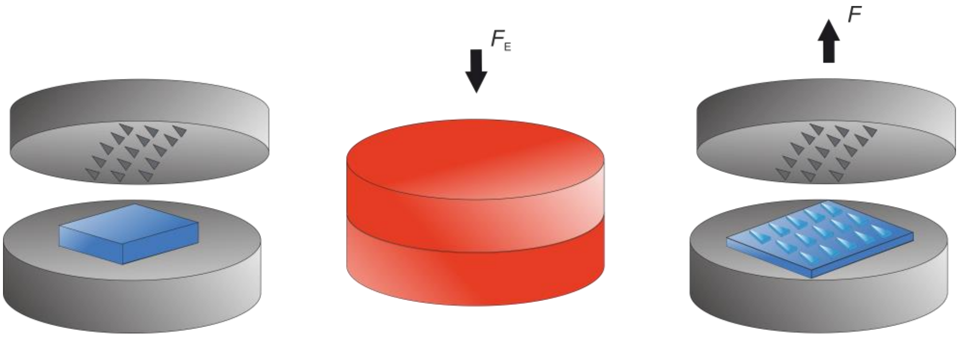

Figure 2.11: Schematic illustration of the hot embossing procedure. First, the polymeric sample such as a SMP is put between a movable plate with the electro-plated Nickel mold insert and a fixed substrate. Then both plates are heated up to the temperature of reshaping the polymer and the mold insert is pressed into the polymer with a constant force. After cooling down to room temperature and demolding the movable plate, the SMP foil with desired microstructures on the surface is obtained.

Figure 2.11 illustrates a schematic image of the hot embossing procedure. More specifically, there are three main steps to conduct hot embossing on a thermoplastic polymer: assembly process, embossing process, and demolding process. First, the mold insert is mounted to the movable plate serving as a stamp tool. The prepared polymer is subsequently placed between the substrate and movable plate. Then the tool plate approaches to the substrate plate and presses into the polymer surface under a controlled force and temperature. After an appropriate waiting time which allows the melted polymer to completely flow into the mold cavities, the system is cooled down and the polymer solidifies with the replicated microstructures from the mold insert onto its surface. Lastly, the tool plate is withdrawn from the substrate and one can collect the structured polymer film from the mold insert or the substrate plate depending on the adhesion between the polymer and the two plates. Compared to the other polymer processing techniques, hot embossing has the advantages of high material universality, low cycle time, and therefore, high throughput [157], making it an attractive replication method. The main drawback of hot embossing is that it cannot replicate complex, three-dimensional structures with undercuts, which limits it to the fabrication of structures with arbitrary planar geometries but with particular requirements in the height direction. In this thesis, the hot embossing technique is used to replicate the micro-fibril structures from ventral snake scales onto SMP surfaces. The experimental operation is conducted with a partly home-built hot embossing machine based on Zwick 1488 universal testing equipment (Matthias Worgull's group, IMT, KIT).

3 Microscopic tribological properties of dorsal sandfish scales

With its extraordinary capability of "swimming" in sand (see Figure 3.1 a and b), the sandfish features fascinating tribological properties, *e.g.*, low friction and high abrasion resistance which are of great interest to scientists for developing new tribological elements. However, the majority of the current tribological analysis on sandfish is based on experiments conducted with a non-standard granular tribometer. It measures granular friction angles determined with loose granular sand where no external load is applied. This chapter introduces a series of detailed, standard structural and tribological investigations on the molted sandfish scales by AFM with several types of probe shape. Snake scales as well as some other common technical surfaces are also analyzed to make a meaningful comparison.

3.1 Micro-structural analysis

To investigate the microstructures on sandfish by AFM or SEM, the molted sandfish scales were collected from kept animals (provided by G. Gassner, Natural History Museum, Vienna, Austria) and properly prepared for further examinations. The obtained scales were cleaned with pressurized air for 30 s and individually singled or cut into small pieces (Figure 3.1 c). In some cases, the ventral and dorsal scales can be distinguished by their different colors. The skin on the back of sandfish exhibits dark color (see Figure 3.1 a), so the scales molted from this area have some dark areas (the scales on the left in Figure 3.1 c). The ventral skin is opaque leading to the opaque molted scales (the right-side scales in Figure 3.1 c). However, in most cases the scales should be distinguished by the microstructures as a previous study [25] indicates that the dorsal scales of sandfish feature comb-like step structures while the topography of its ventral scales is nearly planar. The prepared scales were glued on a glass slide by a double-sided adhesive tape for AFM characterization.

Figure 3.1: Photos of sandfish and its molted scales. (a) A sandfish (*S. scincus*) is resting above the ground of the desert in its natural habitat. (b) The sandfish is half-buried in the sand. Photos are from Gerrit Jan Verspui and used with kind permission. (c) Photos of the molted scales of sandfish. Scales were cut into small pieces or individually singled for further measurements.

The topography of the dorsal and ventral scales of sandfish was examined by AFM and shown in Figure 3.2. On the dorsal scales, the step structures with comb-like substructures at the edge (Figure 3.2 a) were observed, which conforms the previous reports [22, 25]. The step height was measured ranging from 200 nm to 300 nm and the distance between two neighboring steps was determined as approximately 5 µm. However, the direction of the step structures on sandfish body cannot be recognized as it does not molt its scales as a whole piece like snakes but sheds them as many small pieces. No obvious scratches or hurts were observed in the image. Figure 3.2 b) shows the topography of ventral sandfish scales revealing a comparably smooth surface with no recognizable steps. Nonetheless, meticulous µm-scale groves were frequently imaged, which might originate from scratches. No further regular micro- or nanostructures were observed.

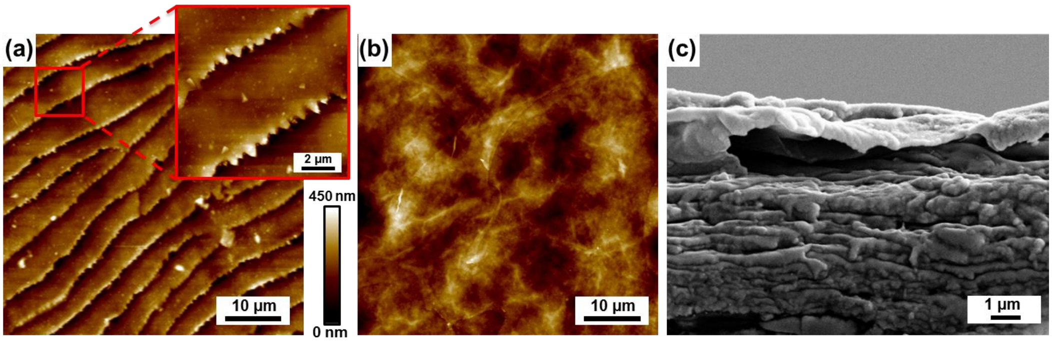

Figure 3.2: Structural analysis of the sandfish scales examined by AFM and SEM. (a) The topography of a dorsal scale measured by AFM reveals step structures which have a saw-tooth like shape magnified in the inset. (b) On the ventral scale no step structures are observed. (c) A cross section of dorsal sandfish scale recorded by SEM suggests a layered internal structure.

Besides the surface topography, the cross sectional architecture is another important structural property which may help sandfish to achieve desirable tribological performances. Figure 3.2 c) displays the cross section of a dorsal sandfish scale imaged by SEM. An inner structure consisting of several thin layers was imaged, which is very similar to snakes [158]. Nano-indentation experiments on snake's multi-layered scales demonstrated both structural and material gradient to dispense pressure and reduce abrasion [159, 160]. The similar inner structure of sandfish might possess the same function as snakes. Nevertheless, the thickness of dorsal sandfish scale (about 8 µm) is much thinner than ventral snake scales (usually about 20 µm or even more) but resemble dorsal snake scales (see Chapter 4.2, Figure 4.4).

3.2 Wettability

Some of lizards living in the extreme dry and waterless desert are optimized with the ability of harvesting water from the surroundings [62], which commonly coincides with low contact angles on their scale surfaces. However, very low or nearly vanishing adhesion was reported on the dorsal sandfish scales by Baumgartner *et al*. [25, 26] indicating low surface energy and typically corresponding to high contact angles [88]. Thus, it is necessary to examine the wettability of sandfish scales.

First, the water contact angle measurement was conducted on single dorsal sandfish scales and the results are summarized in Figure 3.3 a) and b). A 1 µL water droplet was dropped on the scale surface revealing an initial contact angle of 101°. Further monitoring the droplet on the scale in the following 10 min, the droplet shape remains stable and finally behaves a contact angle of 98°. This indicates that the wettability of single sandfish scale is neither superhydrophobic nor superhydrophilic implying a "normal" adhesion property. Despite this, more details about the adhesion property of sandfish scales will be discussed in the following Section 3.3.

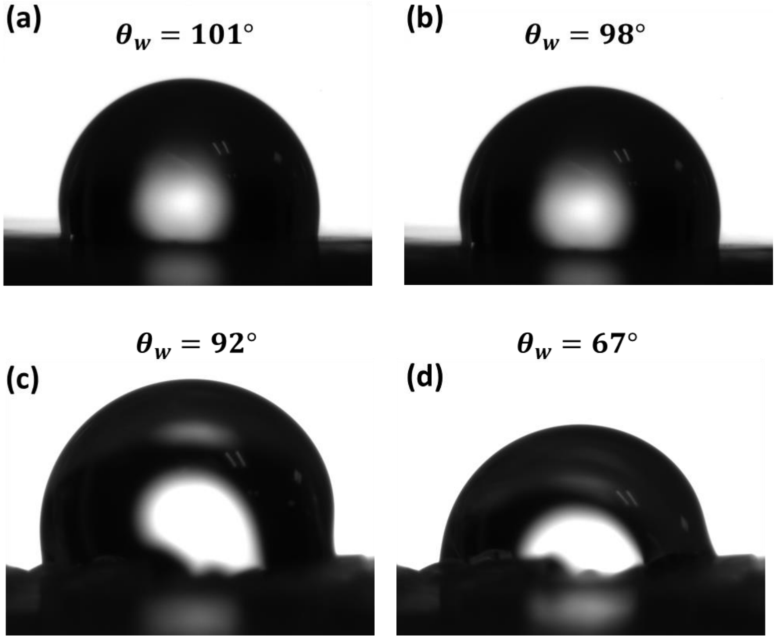

Figure 3.3: Water contact angle on sandfish scales and its variation with time. (a) On single scale an initial contact angle of 101° is observed (droplet volume 1 µL). (b) After 10 min the value reduces to 98°. (c) A 5 µL water droplet covering several scales shows an initial contact angle of 92°. (d) The value decreases significantly to 67° after 10 min.

Furthermore, using larger volumes of 5 µL water droplets the same measurement on multi-scales was conducted to allow the droplet contacting with several scales as well as the tissue between the neighboring scales at the same time. Figure 3.3 c) and d) display the results at the beginning of the experiment and after 10 min, respectively. In this case, the initial contact angle is 92°, which is smaller than that on a single scale. The value decreases significantly with time to 67° after 10 minutes (Figure 3.3 d). It can be seen that the water droplet on multiple scales is not as stable as on a single scale. This is probably caused by the water spreading over the scales and flowing into the connecting tissue between scales. The same phenomenon was also observed by a previous study [62] on sandfish together with some other reptiles, which concludes that these reptiles optimize their scales, *i.e.*, arrangement or ultra-structures to harvest water from their extremely dry living habitat. Nonetheless, the experimental results show that sandfish scales do not exhibit remarkable high or extremely low contact angle if compared to other reptiles. The low adhesion property reported by Baumgartner *et al*. needs to be further checked. Therefore, in the next section I examine the adhesion property of sandfish scales in more detail.

3.3 Adhesion properties characterization

Previous studies [25, 26] contribute the outstanding low friction and high abrasion resistant properties of sandfish skin to the low adhesion ability of its dorsal scales. To further verify this, AFM measurements were conducted to investigate the adhesion properties of sandfish scales. Some technical surfaces as well as snake scales were additionally examined as a comparison. The working principle of AFM for the characterization of adhesion forces has already been described in Chapter 2.3.1. To achieve a meaningful characterization, various types of AFM probes including a sand probe, spherical probe in different sizes, and a sharp silicon tip were used, which were prepared beforehand in Chapter 2.4.1.

3.3.1 Adhesion measurement with different types of AFM probes

Considering that the sandfish "swims" in the sand of deserts, it might possess unique adhesion properties with sand particles. Hence, dorsal sandfish scales were first characterized by a sand probe with a diameter of about 60 µm. Then two additional spherical probes in different diameters (40 µm and 20 µm) and a conventional sharp silicon tip were also utilized to enrich the characterization. Figure 3.4 displays the representative force vs. distance curves on dorsal sandfish scales obtained by the above four probes. All curves show a typical shape as mentioned in Chapter 2.3.1. The negative adhesion peak during the probe retraction (red curve) is clearly visible, which is different for different probes distinguished as their corresponding adhesion force F_{ad} marked by the black arrow in each graph. The adhesion forces on dorsal sandfish scale obtained with the sand probe, 40 µm spherical probe, 20 µm spherical probe, and sharp tip are 288.3 nN, 144.7 nN, 121.3 nN, and 68.2 nN, respectively. One can see that the adhesion force decreases with the probe size due to the decrease of the contact area. However, comparable adhesion force can be detected on dorsal sandfish scales even with a sharp AFM tip, which indicates that there is no vanishing or low adhesion on dorsal sandfish scales.

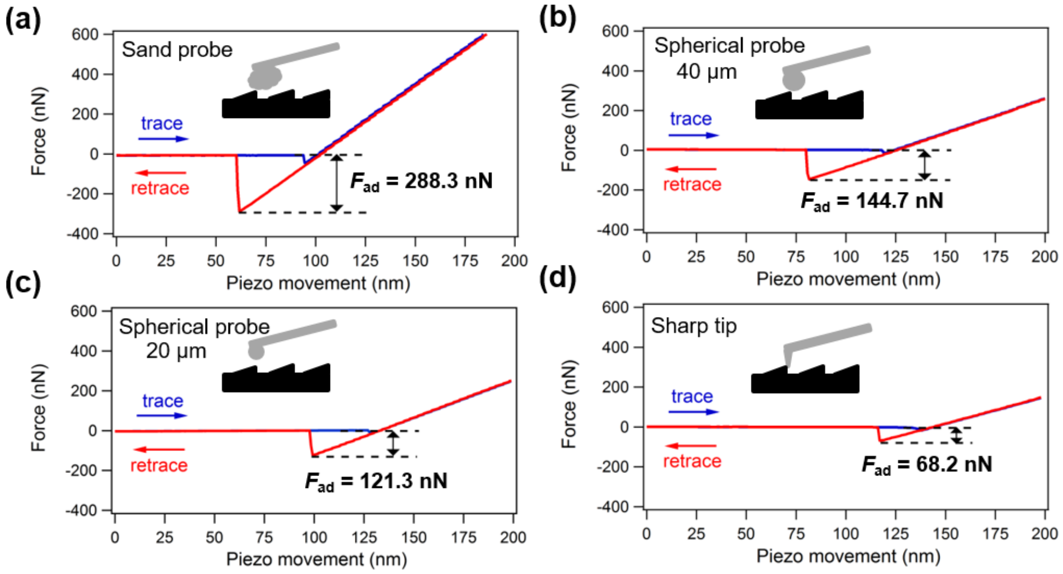

Figure 3.4: Typical force distance curves obtained with various AFM probes. (a) With a sand probe. (b) and (c) with spherical glass probe in different sizes (40 µm and 20 µm). (d) With a conventional sharp silicon tip.

To further validate this, 15 arbitrary positions on dorsal sandfish scales were selected and measured by the above four probes, while the measured positions for each probe were not identical. At each position, ten measurements were repeatedly conducted to calculate the averaged adhesion force and its corresponding statistical error bar. The results are summarized in Figure 3.5 a). The average adhesion of the total 15 positions (represented by the respective dashed lines) obtained with the four probes are 290.8 nN (sand probe), 145.4 nN (40 µm spherical probe), 121.0 nN (20 µm spherical probe), and 67.3 nN (sharp tip), respectively. This result coincides with the force vs. distance curves in Figure 3.4, indicating the decrease of adhesion force with the contact area. Furthermore, the same experimental procedure on sandfish scales was conducted with two other spherical probes which had the same diameter (20 µm) but were sputtered with metal coatings (copper and tungsten, respectively). Figure 3.5 b) shows the adhesion results obtained by the two metal-coated spherical probes as well as a same-sized bare spherical probe with no coatings. It can be seen that the averaged adhesion force for these three probes are nearly alike (105.0 nN for copper coated probe, 115.5 nN for tungsten coated probe, and 124.9 nN for bare probe). This indicates that the metal coating only moderately influences the adhesion values if compared to the probe size (*i.e.* contact area).

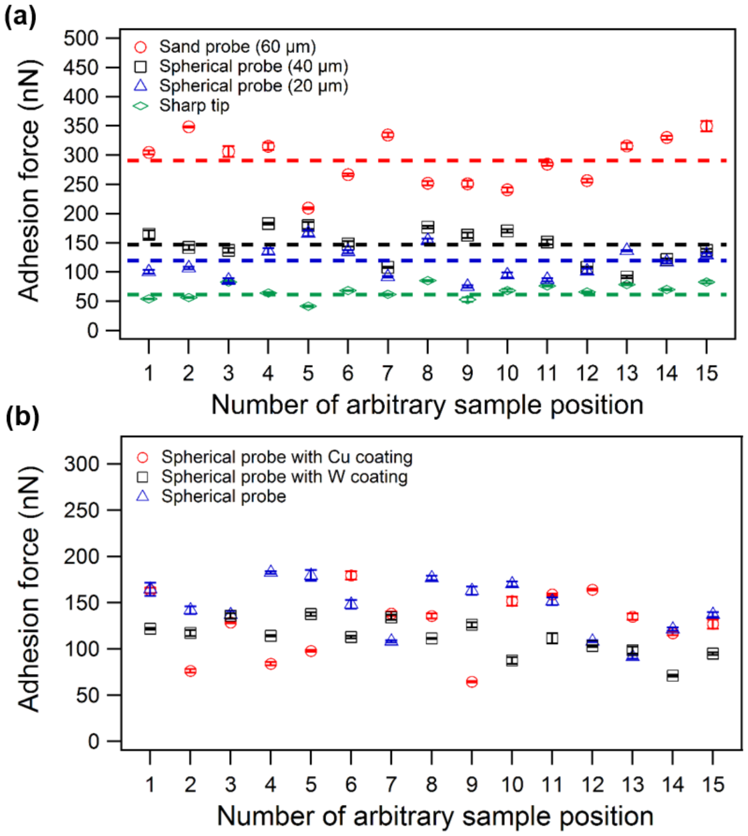

Figure 3.5: Adhesion characterization of sandfish scales by AFM. Various AFM probes in different size or surface chemistry were used. (a) With four different sized probes indicating different contact areas. (b) With 20 µm diameter spherical probes which are without or with copper or tungsten coating. For each probe, 15 arbitrary positions were measured on dorsal sandfish scales and at each position the adhesion forces were measured 10 times to calculate an average value (one data point in the graph) and its corresponding error bar. The overall average adhesion of all 10 × 15 = 150 measurements obtained with each probe was calculated and represented by the corresponding dashed line.

3.3.2 Adhesion comparison with snake scales and other technical surfaces

Since adhesion between AFM probes and dorsal sandfish scales obviously exists, it will be of high interest to compare this with other materials to further evaluate the adhesion properties of sandfish scales. Additional adhesion experiments on a biological reference (*S. diadema* ventral scales) and four tribological relevant surfaces (PMMA, Teflon, HOPG, and silicon) together with dorsal sandfish scales were conducted with a sharp silicon tip to check if sandfish show superior adhesion behavior. The results of all these samples are illustrated in Figure 3.6 a). Similar to in Figure 3.5, averaged adhesion forces from ten repeated measurements on 15 arbitrarily chosen positions were calculated on each sample. The overall averaged values for sandfish (67.3 nN) are slightly larger than that for *S. diadema* (41.3 nN), Teflon (46.1 nN), and silicon (54.2 nN). However, the adhesion on technical surfaces like PMMA (98.2 nN) and HOPG (225.2 nN) is even higher than for sandfish, especially that on HOPG is nearly 3.4 times of that on the sandfish scale. Consequently, despite that sandfish, to some degree, display low adhesion forces for sharp tips if compared to technical surfaces like PMMA or HOPG, this adhesion is not exceptionally low.

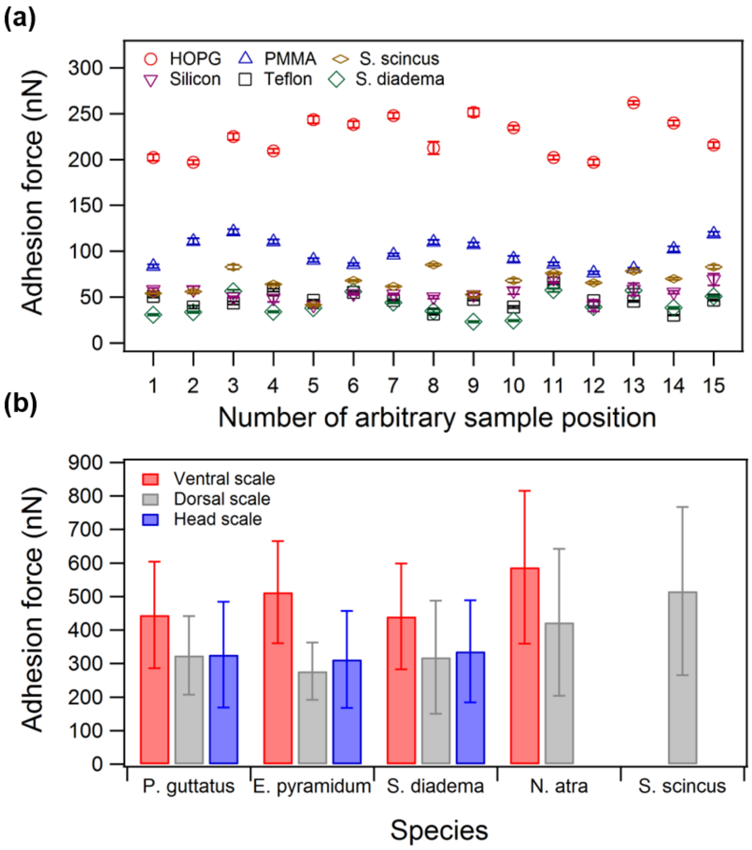

Figure 3.6: Adhesion comparison between sandfish scales and other materials. Snake scales as well as some other technical surfaces were examined for comparison. (a) Adhesion forces on sandfish scales, Clifford's diadem snake (*S. diadema*) and four technical surfaces measured with a sharp AFM tip. The experimental procedure is same as in Figure 3.5. (b) Direct comparison of adhesion between dorsal sandfish scales and snake scales in their ventral, dorsal and head regions. Four snake species (*P. guttatus*, *E. pyramidum*, *S. diadema*, and *N. atra*) were measured. A sand probe was utilized for characterization. Every data point (represented by a column) is averaged from five force vs. distance curves at fourteen different positions, *i.e.*, n = 70 measurements.

It is interesting to note that the adhesion on *S. diadema* ventral scales is lower than that on dorsal sandfish scales. In this case, a more detailed analysis of a sand probe interacting with the scales from different regions of snakes and sandfish is presented (Figure 3.6 b). More specifically, the adhesion forces were measured on the ventral, dorsal, and head scales of *S. diadema*, *E. pyramidum*, *P. guttatus*, and *N. atra*, respectively, and compared with the results of dorsal sandfish scales. For the investigated snakes, adhesion forces between the sand probe and dorsal scales are nearly equal to that on the head, which are both smaller than that on their ventral scales. In addition, the adhesion of the four snake species is very similar in terms of the scales from the same region even if they are native in different types of habitat, *e.g.*, *S. diadema* and *E. pyramidum* live in or near sandy environments while *P. guttatus* and *N. atra* are native in forests. Although living with sandy surroundings, *S. diadema* and *E. pyramidum* do not show any advanced adhesion properties with sand particles. More surprisingly, the dorsal scales of sandfish show even larger adhesion forces for the sand probe than the dorsal scales of all other examined snakes. This result demonstrates that the analyzed sandfish scales do not feature exceptional low adhesion if compared to the investigated snakes.

Overall, sandfish scales do not possess superior adhesion properties which might help them to achieve the fabulous low granular friction and wear rates. Some other reasons such as elastic properties of their epidermis or dynamics of sandfish "swimming" might be the cause for this. Consequently, further studies are needed. Despite this, it is still necessary to characterize the friction properties of dorsal sandfish scales with a standard method to specify their frictional performance.

3.4 Friction properties characterization

Generally, the macroscopic frictional coefficient μ, which is defined as the ratio between the measured lateral friction and applied normal load ($\mu = F_{\mathrm{fric}} / F_{\mathrm{load}}$) on the surfaces, was calculated to describe the friction properties of technical surfaces. However, during sandfish "swimming" in the sand, numerous microscale contacts are generated simultaneously and the friction occurs without a defined load. As a result, previous studies characterized friction on sandfish skin by a granular tribometer which allows sand particles pouring through a funnel from a high position directly onto the tilted animal body. The tilted angle at which the sand particles stop to slide off the animal is called granular friction angle (θ_{gr}). This granular tribometer is of high practical value for field studies where classical tribometer experiments with animals are challenging. However, with this method the granular friction angles are roughly determined by loose sand particles but with no external load applied on the animal bodies. The granular frictional coefficient is estimated by $\mu_{\mathrm{gr}} = \tan\theta_{\mathrm{gr}}$, but this does not allow a classical load vs. friction analysis. Therefore, to analyze the friction properties of sandfish, exhaustive friction examinations were carried out on the molted scales of sandfish with a micro-tribometer and AFM.

3.4.1 Friction characterization by AFM

First, microscopic measurements recording friction vs. load curves on dorsal sandfish scales were conducted by AFM with various probes. The sand probe, spherical glass probe, and sharp silicon tip were utilized to scan on the sandfish scales creating different types of contacts. The scanning size was set to 20 µm × 20 µm. For each measurement, a friction loop (see Chapter 2.3.1, Figure 2.5) [140] was recorded for the AFM tip scanning in forward and backward directions with varying normal load. The averaged friction forces for both directions were calculated. This procedure neglects the friction anisotropy caused by the step structures on dorsal sandfish scales [49]. This type of friction anisotropy at the nano-step structures will be emphatically discussed in Chapter 5. For each sample, three different positions were analyzed, and the results were averaged into each single data point in Figure 3.7. The error bars correspond to the standard deviations from averaging. Increasing the defined load F_{load} and recording the frictional force F_{fric}, the friction coefficient μ can be calculated by linearly fitting the applied load and its corresponding friction data ($F_{\mathrm{fric}} = F_{\mathrm{adh}} + \mu \times F_{\mathrm{load}}$).

Figure 3.7 a) shows the resulting friction vs. load curves of the dorsal sandfish scales recorded with a spherical probe, a sand probe, and a sharp tip. With each probe, the data sets manifest a nearly linear relationship between the normal loads and friction forces. The friction coefficient μ was calculated as the slope of this linear fit (provided in the legends) and compared between the results from different probes. The value obtained with the spherical probe (0.28) and sand probe (0.27) is very close to each other and slightly larger than that obtained with a sharp tip (0.22). This means that, on the one hand, dorsal sandfish scales do not show unique or exceptional low friction properties with sand debris if compared to other tips. On the other hand, the contact area during the friction measurement may cause a small influence on the obtained friction coefficient.

Furthermore, biological and technical samples including a *S. diadema* ventral scale, Teflon, PMMA, silicon, and HOPG were also investigated with the same sharp tip (*i.e.* a small contact area) as a comparison. The results are displayed in Figure 3.7 b) (the data sets for sandfish were replotted from Figure 3.7 a). Similarly, conducting the linear fit and calculating the gradient, one can observe that the friction coefficient for

Teflon (0.78) is the largest, followed by PMMA (0.63) and silicon (0.50). The smallest friction coefficient is obtained on HOPG (0.02), which is expected for this well-known dry lubricant. Interestingly, the friction coefficient of the *S. diadema* ventral scale (0.07) is nearly as small as that for HOPG. Friction for sandfish scales under the same normal load, however, is found to be between these two groups, *i.e.*, the friction coefficient for dorsal sandfish scales (0.22) is significantly lower as for technical materials such as Teflon, PMMA, and silicon but considerably higher as for HOPG and a psammophile snake like *S. diadema*. This outcome shows that sandfish scales exhibit good but not exceptional low frictional behavior as it might be expected at the microscale, at least they are not as good as snake *S. diadema*.

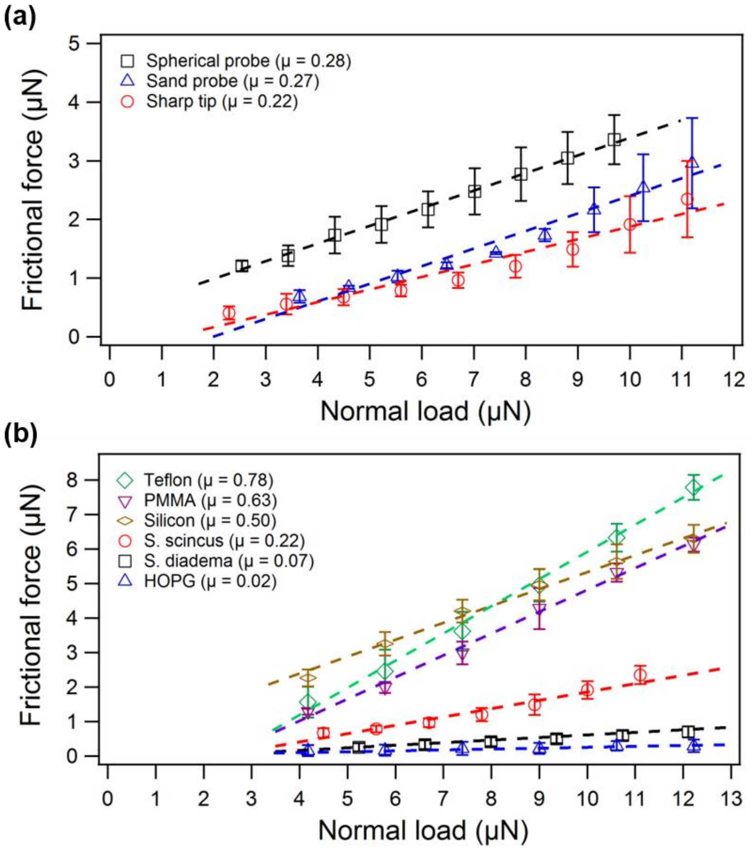

Figure 3.7: Friction vs. normal load analysis on dorsal sandfish scales and some other materials. Various AFM probes were used. Snake scales and several technical surfaces were characterized for comparison. (a) Measurements on dorsal sandfish scales with a spherical glass probe, a sand probe, and a sharp silicon tip, respectively. (b) Comparison between dorsal sandfish scale and ventral snake scale together with four technical surfaces with the same sharp silicon tip. The data sets of each measurement were linearly fitted (represented by the dashed lines in the plots) and the microscopic frictional coefficient μ was calculated as the gradient of the fitting (given in the legends).

3.4.2 Friction measured by micro-tribometry

Moreover, I also characterized the friction properties of dorsal sandfish scales with a reciprocating linear ball-on-plate micro-tribometer in the group of Christian Greiner, IAM, KIT. *S. diadema* ventral scale and technical surfaces such as 100Cr6 (AISI 5210) bearing steel, PEEK, silicon, HOPG, PMMA, and Teflon were also investigated for comparison. Snake and sandfish scales were cleaned with pressurized air for about 30 s. All non-biological samples were prepared by grinding with SiC papers of #800 down to #4000 grids together with mechanical polishing with a 3 µm diamond suspension (5 min) and 1 µm diamond suspension (8 min) purchased from Struers, Willich, Germany. This leads to a scratch-free surface with roughness of Ra < 0.01 µm determined by optical profilometry (Sensofar Plµ neox, Barcelona, Spain). A polished, 1 mm diameter sapphire sphere from Saphirwerk AG (Bruegg, Switzerland) was used to pair against the sample surfaces under observation. For all experiments, the normal load and the sliding speed were set to 0.1 N and 0.5 mm/s, respectively. On each sample, three reciprocating lines with a stroke of 10 mm were measured for 10 cycles. The recorded friction forces were averaged and divided by the set normal load to calculate the friction coefficient μ_{tri}. All measurements were conducted at room temperature and relative humidity of 50%.

Figure 3.8 presents the average friction coefficients measured by AFM and micro-tribometer on all the samples mentioned above, respectively. The settings of AFM measurements are the same as that in Chapter 3.4.1. For all measurements, the friction coefficients of each surface were averaged, and the results obtained with AFM and micro-tribometer were compared. The friction coefficients measured by the micro-tribometer demonstrate that when in contact with a 1 mm sapphire sphere, dorsal sandfish scales exhibit approximately the same friction coefficient as PEEK which is a polymer widely used in tribological applications. Sandfish shows larger values than most of the other technical surfaces such as PMMA, Teflon, HOPG, and 100Cr6 bearing steel. However, the friction coefficient of *S. diadema* ventral scales is comparably smaller and roughly equal to that of 100Cr6 bearing steel. Therefore, from the results obtained with the micro-tribometer, dorsal sandfish scales do not feature exceptional friction properties if compared to technical surfaces or ventral snake scales. Interestingly, the friction coefficients of all technical surfaces (except HOPG) characterized by AFM are considerably higher than the ones obtained by micro-tribometry, while the values of the biological surfaces from the two characterization methods are very similar. Besides this, comparing between the results of different samples characterized by AFM, one can find that sandfish shows lower friction coefficient than most technical materials with the exception of HOPG, but not as low as the snake *S. diadema*, which also corresponds to the results in Chapter 3.4.1.

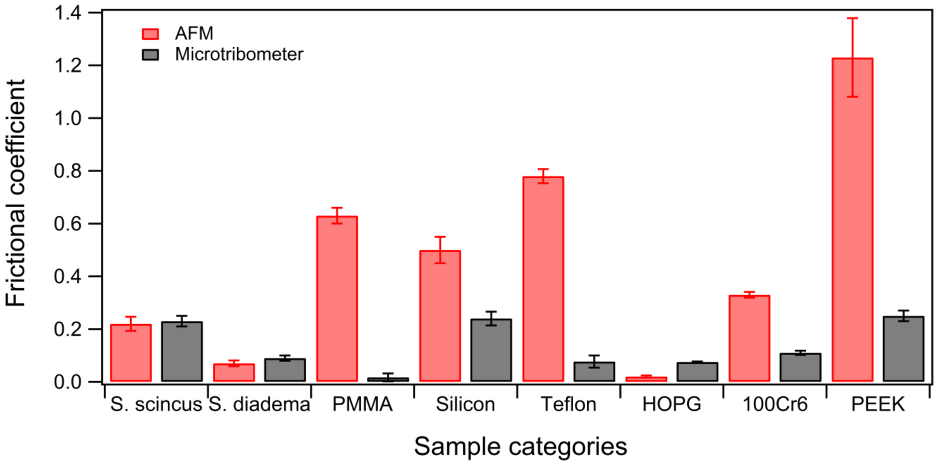

Figure 3.8: Comparison of the friction coefficients obtained with AFM and micro-tribometry. Two biological samples and six technical surfaces mentioned in the text were tested. The results of the same material examined by the two characterization methods are compared. The AFM measurement settings are the same as in Chapter 3.4.1. Average friction coefficient in each measurement was compared and the corresponding error deviation was calculated.

The different friction coefficients between the measurements on the same technical surface conducted by micro-tribometry and AFM might be caused by the resulting sub-micron topography features during the sample preparation process. High wave-vector components of the power spectral density on the surface topography were produced during the grading and polishing procedure. This probably causes significantly frictional influence on the nanoscale, which can be detected by AFM but cannot be sensed by the micro-tribometer [161]. Thus, AFM characterization shows larger friction coefficients. Nevertheless, in both cases, sandfish scales do not display the reported unique friction properties and they behave even not as good as the analyzed snake scales.

3.5 Scratch resistance properties characterization

Another fact of sandfish swimming under sand, which cannot be ignored, is that the sand grains scratch its epidermis acting as a sharp abrasive. Numerous contacts and scratches will happen all over the animal body once it submerges into the sand particles every day. A granular abrasion resistant test on dorsal sandfish skin together with technical surfaces such as Teflon, glass, and steel revealed that sandfish skin got less damage and could resist wear better than the investigated technical surfaces [19, 23, 24]. In this section, the abrasion resistance of dorsal sandfish scales is examined on the microscale based on a direct scratching experiment conducted by AFM. A comparison with *S. diadema* ventral scales and other technical surfaces was also carried out.

The procedure of the scratch resistance experiment is very similar to that of the friction measurements, but very large normal load is applied to provoke wear on the surface. In order to achieve this, several commercial, very hard AFM cantilevers (nominal spring constant of 40 N/m, All-in-One-Al, BudgetSensors) with a sharp tip at the end were utilized. Various samples including dorsal sandfish scales, *S. diadema* ventral scales, PMMA, Teflon, and aluminium (Al) were tested. For each sample, a fresh cantilever with a virgin tip was employed to avoid the influence of the tip wear when scratching on different samples. Nine small squared areas (size: 5 µm × 5 µm), which are evenly located on a 40 µm × 40 µm examined area, were scratched on each surface. The normal load or the scratching time was systematically increased for each subsequently scanned small area. The number of scanning lines was 128 × 128 and the scanning velocity was set to 0.8 Hz.

3.5.1 Scratching forces

Figure 3.9 shows the wear patterns on the five investigated samples, which were scratched with nine increasing normal loads on each surface, respectively. Their corresponding relationships between the scratching depth and the applied normal load are also summarized in the last image. According to the linear increase of the friction force with normal load (see Section 3.4.1), the scratching forces were increased in the nine squared areas on each sample. In all AFM images in Figure 3.9, the normal load was increased from left to right and top to bottom by increasing the "setpoint" (see Section 2.3.1) in voltage steps, *i.e.*, $F_{\text{load}} = C_z \times S_{\text{ver}} \times (U_{\text{ver}} - U_{\text{dis}})$, while all the other scratching conditions were fixed. However, due to the slight difference of the deflection sensitivity (S_{ver}) of each virgin cantilever used for scratching each sample, the normal load on each surface was also not exactly the same. The final largest normal load in the lower right corner of each AFM image ranges between 35 µN and 60 µN according to the deflection sensitivity of the AFM cantilever. Nonetheless, it is obvious to see that on every surface, materials in at least two squared areas were, more or less, scratched. However, the normal load at which the surface started to be scratched on each sample is different.

To quantitatively analyze the abrasion resistant ability of the investigated samples, the scratching depth in each scratching area was measured and plotted as a function of its corresponding applied normal load. The results are summarized in the last graph in Figure 3.9. It can be seen that all the investigated samples were finally scratched after the normal load reached a certain threshold, while for each sample this threshold differs slightly except the Al which got scratched until the normal load increased to above 25 µN. For all samples, the scratching depth shows a linear increase with normal load after reaching its scratching threshold. Similar abrasion resistance with normal load ability is found on PMMA, ventral snake scales, and dorsal sandfish scales, while their scratching resistance is not as good as for Teflon and Al.

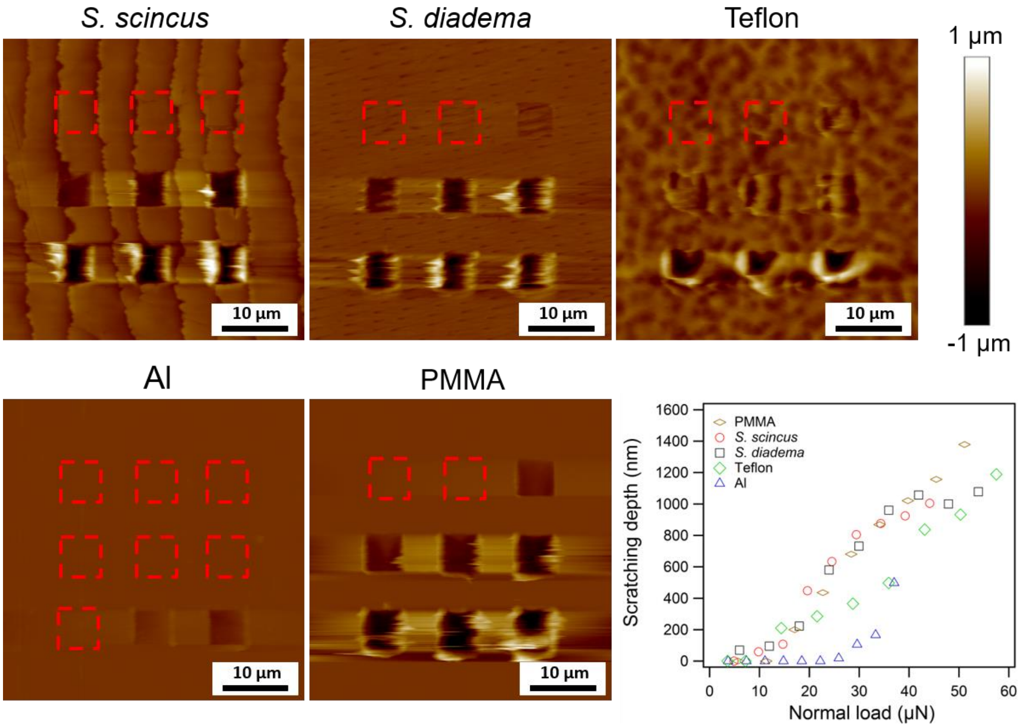

Figure 3.9: Abrasion resistance experiments on five different materials characterized by AFM. A hard cantilever was used to scratch nine squared areas (5 µm × 5 µm) on each sample. The normal load was increased in each subsequently scratched area from left to right and top to bottom. For each material, a virgin sharp tip cantilever was utilized to start scratching. The AFM images (first five images) show the wear pattern of the investigated surfaces with normal load increasing in steps on the nine areas. The dashed, red rectangles on the AFM images represent areas with no obvious wear observed. The last graph demonstrates the scratching depth plotted as a function of normal load extracted from the wear patterns in the AFM images.

3.5.2 Scratching time

Besides abrasion resistance with normal load, the endurability with scratching time was also examined on the investigated samples. A same experimental procedure with constant load but increasing scratching time in every scratched area was conducted. For experiments on all the samples, the normal load was kept the same at 19.6 µN while the scratching time was increased stepwise by 2.5 minutes. Figure 3.10 shows the AFM images with wear patterns on the corresponding sample surfaces and the quantitative analysis of the scratching depth increasing with scratching time.

Since the applied normal load is larger than the scratching threshold of most investigated samples except Al, the wear patterns on these surfaces are very apparent. Similarly, the scratching depth on each scratching area was extracted from the wear patterns in AFM images and plotted as a function of its corresponding scratching time to evaluate the endurability of abrasion resistance of each sample (the last graph in Figure 3.10). On PMMA, Teflon, and dorsal sandfish scales the scratching depth grows constantly with the scratching time, while on Al no wear is observed because 19.6 µN of normal load is too small to get any scratches on this surface. Interestingly, the scratching depth first increases nearly linearly with scratching time and then reaches a plateau after 12 min scratching on the ventral scales of snake *S. diadema*. This phenomenon was also found in its normal load dependent scratching experiment (see Figure 3.9). This is probably caused by the inhomogeneity of the layered construction from the inner structure of the snake scale, *i.e.*, a layer with higher abrasion resistant ability might be finally reached at the scratching depth of 1000 nm to 1300 nm.

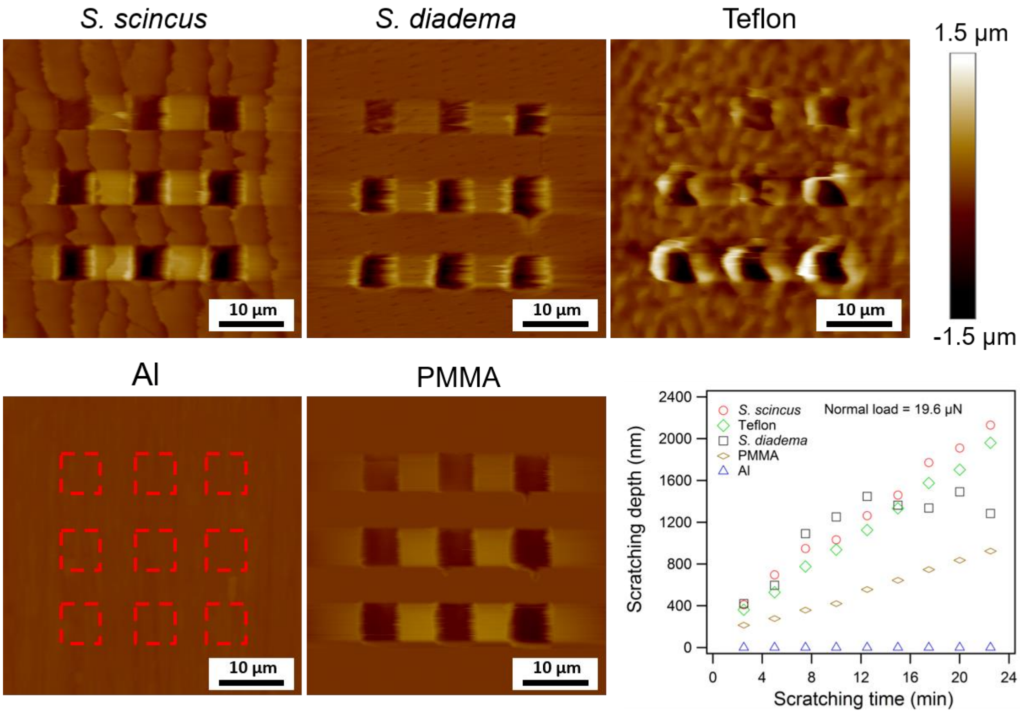

Figure 3.10: Similar wear testing procedure as in Figure 3.9 but with scratching time increasing. The scratching time increased in the corresponding nine squared areas (from left to right and top to bottom) with the same normal load applied on their surfaces. For all the scratching experiments, the normal load was fixed to 19.6 µN, but the scratching time was increased stepwise by 2.5 minutes. AFM images show the wear patterns on each sample. The last graph displays the scratching depth plotted as a function of the scratching time, which were extracted from the corresponding wear patterns in the AFM images.

Therefore, from the results of the scratching experiments by AFM, the overall wear resistance of sandfish scales against a sharp silicon tip is not superior to the investigated technical surfaces or the scales of snake *S. diadema*. Finally, as a short conclusion of this chapter, at least on the microscale the tribological properties including adhesion, friction, and abrasion resistance of sandfish scales do not reveal exceptionally advanced features.

A shortened version of this chapter was published as the article [21] "Characterization of the microscopic tribological properties of sandfish (Scincus scincus) scales by atomic force microscopy", by Weibin Wu, Christian Lutz, Simon Mersch, Richard Thelen, Christian Greiner, Guillaume Gomard, and Hendrik Hölscher, Beilstein Journal of Nanotechnology, 9, 2618-2627 (2018).

4 Multi-functionality of snake scales

The scales of snakes do not only act as protection isolating the body from the environment, they are also important as functional interfaces. Scales covering different regions of snakes, *i.e.*, dorsal, ventral, and spectacle scales, show different appearance (*e.g.* shape, color, size, *etc*.) indicating multiple types of functions. Particularly, the ventral scales of snakes frequently enduring friction and wear might possess fascinating friction reducing or wear resistant abilities; the spectacle scales functioning as a window for the eye lens might help to filter harmful or to enhance useful light spectrum; the dorsal scales on the backside of snakes are probably able to self-clean since snakes do not have extremities to clean themselves. Similar to many biological cases, all these potential functions very likely coincide with specific types of surface micro-ornamentations. Thus, in this chapter, starting with imaging the micro-ornamentations on the scale surfaces, the multi-functionality of scales in different regions of the snake body (*i.e.* dorsal, ventral, and spectacle scales) is characterized on the twelve snake species presented in Table 2.1. The structural properties including topography and cross sectional design, wettability, adhesion properties as well as the spectral transmittance properties are studied by various characterization techniques to systemically investigate the multi-functionality of snake scales.

4.1 Micro-ornamentations on the ventral, dorsal, and spectacle scales

Before characterizing their functions, the topography of the scales in different regions of the snake body was imaged by SEM. To better analyze the topographical features of different snake species, the micro-ornamentations of scales from the same regions were summarized and compared between the twelve species. In this section, the results of the ventral, dorsal, and spectacle scales are presented.

4.1.1 Ventral scales

Due to their special locomotion style, snakes are in direct contact with the substratum by ventral scales which have to, unavoidably, endure friction and wear every day. This might encourage snakes to evolve the micro-ornamentations beneficial to reducing friction or enhancing wear resistance on this type of scales. Thus, the topography of the ventral scales of the mentioned twelve snake species was first imaged. The results are shown in Figure 4.1. Comparing between different species, it can be seen that a common pattern of oriented micron-sized fibril structures is found on most investigated snake species except *C. hortulanus* and *E. pyramidum* (see Figure 4.1 h and i).

For all images in Figure 4.1, the snake body proceeds horizontally with their head pointing towards the right side. Hence, for the snakes featuring micron-sized fibril structures on the ventral scales, the micro-fibrils are unidirectionally oriented and the fibril ends always point towards the snake's tail. Nonetheless, the shape of the micro-fibrils on these snakes is slightly different for each species, *e.g.*, a special, willow leaf shaped fibril was found on *S. diadema* (Figure 4.1 g). The fibril end on this snake exhibits a sharp tip while that on the other species with micro-fibril structures is similarly rounded (see Figure 4.1 a - f). Both types of micro-fibril structures are typically parallel-organized along the snake bodies. The length of these fibril structures ranges from 1.5 µm to 4 µm depending on different species and the width ranges from 0.6 µm to 1.5 µm.

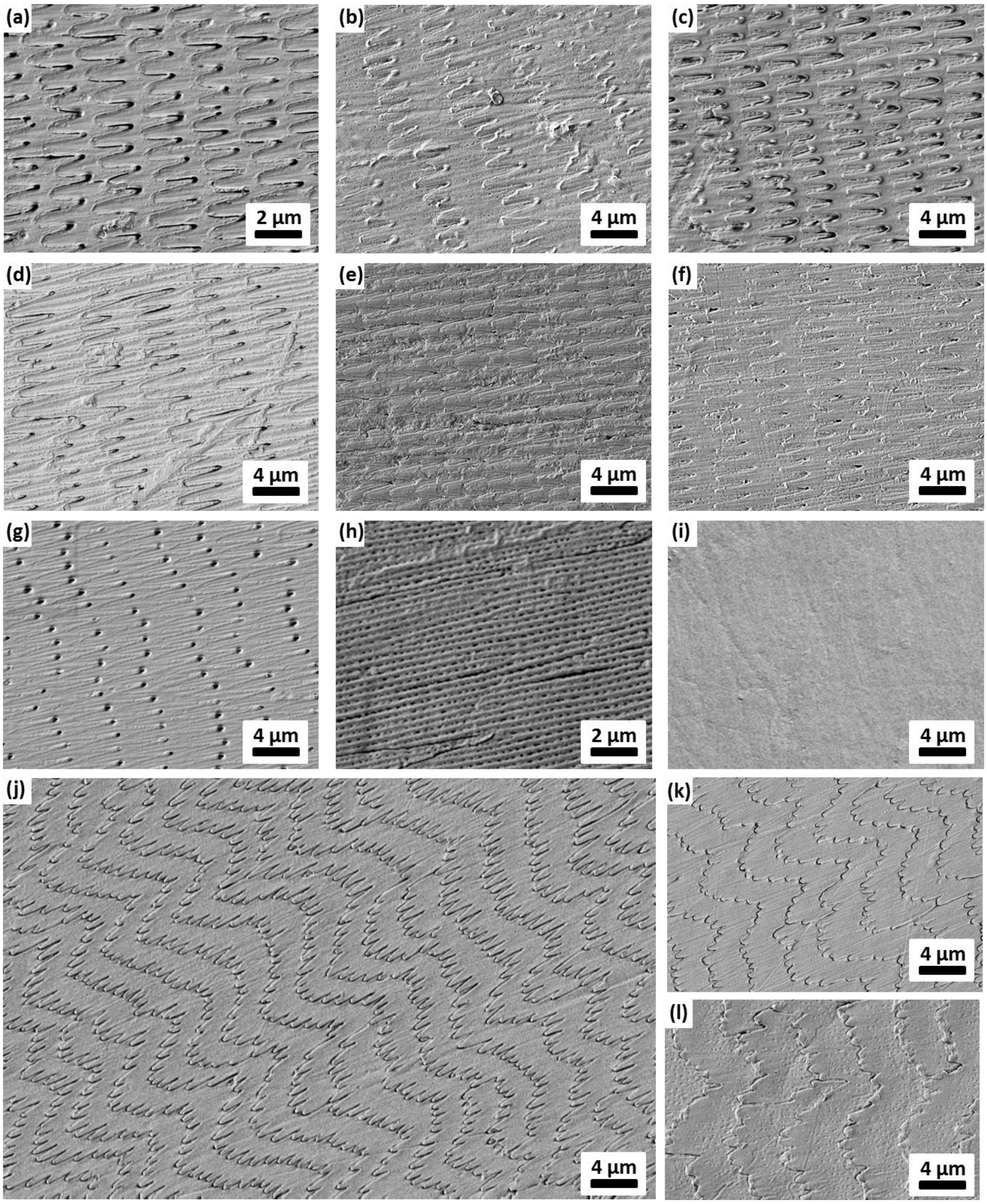

Figure 4.1: Topographical images of ventral snake scales characterized by SEM. Twelve snake species were examined. For most snakes including (a) *P. guttatus*, (b) *B. arietans*, (c) *N. atra*, (d) *V. aspis*, (e) *M. monspessulanus*, and (f) *S. miliarus*, a common pattern of oriented micron-sized fibril structures is observed. The micro-fibrils on the ventral side of (g) *S. diadema* display a slightly different shape like a willow leaf with a sharp fibril tip. However, (h) *C. hortulanus* and (i) *E. pyramidum* show totally different micro-ornamentations. A reticulate structure (smaller size than micro-fibril structures) with nanoridges is found on *C. hortulanus* ventral scale. *E. pyramidum* shows a flat topography with no apparent micro- or nanostructure, which is very similar to sandfish. More interestingly, three Australian pythons of (j) *A. perthensis*, (k) *A. ramsayi*, and (l) *M. spilota* exhibit more delicate, hierarchically organized micro-fibril structures. The size of these hierarchical fibrils is much smaller than the normal fibrils in (a) - (g). For all the SEM images, the snake body is oriented from the left (tail) to the right (head).

However, it is interesting to note that on the last three species (see Figure 4.1 j - l, corresponding to *A. perthensis*, *A. ramsayi*, and *M. spilota*, respectively) the micro-fibril structures are hierarchically organized.

One can observe about 5 - 15 small fibrils located on a relative larger fibril structure (*i.e*. the triangle-shape structure in Figure 4.1 j). More interestingly, all these three species are pythons from Australia. This indicates that, probably, some special functions or abilities exist on their ventral scales for better adapting to their habitat in Australia. Furthermore, the size of the micro-fibril structures on these three snakes is much smaller than on the above-mentioned species which show micro-fibrils (the first seven species, Figure 4.1 a - g). The fibril length and width is normally in the range of 0.4 µm -1.5 µm and 0.4 µm, respectively.

If comparing between the micro-fibril structures of ventral snake scales and the step structures of the dorsal scales of sandfish, a common structural characteristic of these reptiles can be found, *i.e*., the micro-fibril structures produce nanoscale steps at their fibril ends (tips) which are similar to the step structures. Although ventral snake scale does not exhibit continuous step structures as sandfish, the micro-fibrils longitudinally oriented in the same direction show many distributed nano-steps on its surface. These nano-steps might cause the same frictional effect as the continuous step structures during locomotion, which indicates very similar mechanism of controlling friction between snakes and sandfish. A more detailed analysis of the frictional behavior of the step structures on scales of snakes and sandfish will be introduced in the following Chapter 5.

Finally, there are also two snake species which show totally different micro-ornamentations on their ventral scales. *C. hortulanus,* with the common name Amazon tree boa, is a species form South America. As its common name indicates, this snake possesses the ability to climb trees. A pattern of reticulate structure with ridges oriented along the longitudinal body axis is observed on this species (Figure 4.1 h). The size of this reticulate structure is in the range of several tens or hundreds of nanometers, which is even smaller than the hierarchical fibril structures on the Australian pythons. Some other species (*e.g. A. ramsayi*, *M. spilota*, and *P. guttatus*) can also climb trees. Considering that these species show the common micro-fibril structures on their ventral side, the reticulate structure on *C. hortulanus* might not be particularly developed for this function. However, previous studies indeed reported friction anisotropy on the ventral scales of *C. hortulanus* [65, 160]. As for *E. pyramidum,* this species is commonly called carpet viper and found in the area from Northeast African to Arabian Peninsula which is in the same geographical area as sandfish. Moreover, also similar to sandfish, the ventral scales of this snake show a relative flat surface without any micro- or nanostructures (see Figure 4.1 i and Figure 3.2 b). We, therefore, speculate that their same living conditions might force *E. pyramidum* and sandfish to evolve similar absent micro-ornamentations on their ventral side.

4.1.2 Dorsal scales

Dissimilar to ventral scales, the dorsal scales of snakes are usually decorated with various colors or patterns in terms of different species. On the one hand, these decorations may help snakes to better hide themselves in their respective surroundings (camouflage) and protect them from the predators. On the other hand, these decorations also indicate special microstructures on the scale surface, which might be evolved for the aim of providing unique wettability or reflecting harmful light spectrum. Hence, the topography of the dorsal scales of the investigated twelve snake species was imaged by SEM and summarized in Figure 4.2. It can be seen that for different species the micro-ornamentations on their dorsal scales vary considerably in shape and size. In difference to the ventral scales, various types of microscopic patterns were observed on the surface of dorsal scales.

Some of the investigated species show very similar micro-ornamentations. For example, the indistinguishable foveate (basin-like) patterns with reticulate and porous structures on *S. miliarus* and *B. arietans* (Figure 4.2 a and b). *V. aspis* and *M. monspessulanus* also show a similar type of canaliculated micro-dermatoglyphics with crosshatching ribs on their dorsal scales (Figure 4.2 d and e). Despite this, the micro-ornamentation patterns between these two groups are totally different. More specifically, *V. aspis* and *M.*

monspessulanus are the species commonly found in southwestern Europe (see Figure 2.2). The close geographical location as well as the same living habitat (both snakes live in shrubby areas) might be the reason for the similar microstructures on the dorsal part of these two snakes. Both snakes evolved similar microstructures on their backside to better adapt to their living surroundings. As for *S. miliarus* and *B. arietans*, although native in different continents (North America and Africa, respectively), they both belong to the family Viperidae and their dorsal scales exhibit very similar, extreme black patterns. The microstructures on these two snakes might help to absorb visible light and as a result, to enhance the dark color. However, there is no evidence showing any relationship between these two groups of snakes (*i.e*. group of Figure 4.2 a, b and group of Figure 4.2 d, e), leading to totally different micro-ornamentations on their dorsal scales.

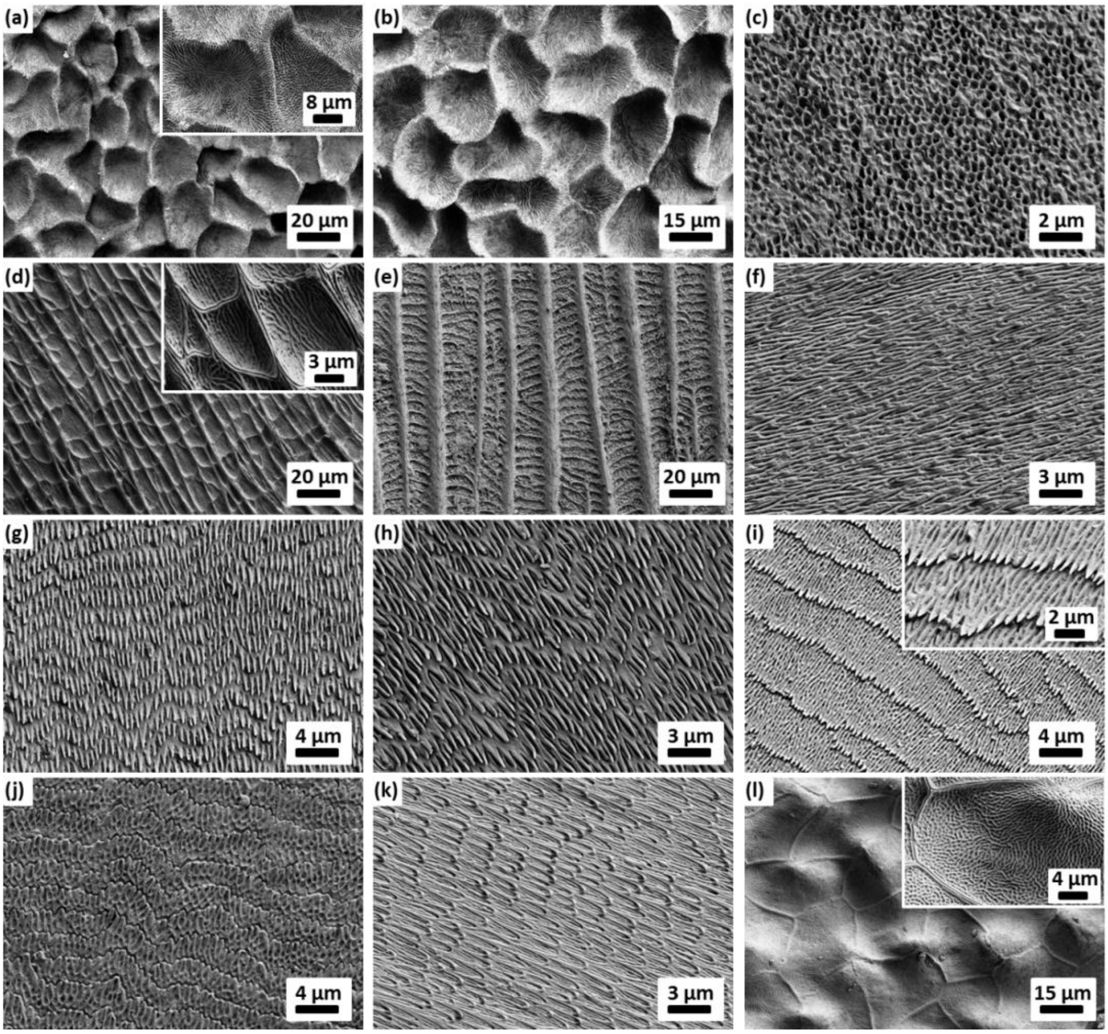

Figure 4.2: Topographical images of dorsal snake scales characterized by SEM. The same twelve snake species as in Figure 4.1 were examined. The results show various types of hierarchical microstructures on the investigated species: (a) *S. miliarus* and (b) *B. arietans* (foveate/porous); (c) *C. hortulanus* (polygonal); (d) *V. aspis* and (e) *M. monspessulanus* (canaliculated/ribs); (f) *P. guttatus* (reticulate); (g) *A. perthensis* and (h) *A. ramsayi* (lamellate imbricate/echinate); (i) *S. diadema* (lamellate imbricate/reticulate); (j) *M. spilota* (lamellate imbricate/papillate); (k) *N. atra* (imbricate/echinostriate) and (l) *E. pyramidum* (verrucate/ reticulate). In some subfigures, an inset image representing an enlargement of a small area of the image is embedded to show more details about the substructures.

Furthermore, several different types of micro-ornamentations were found on the other species such as a polygonal juxtaposed or honeycomb like pattern on *C. hortulanus* (Figure 4.2 c) and a reticulate pattern on

P. guttatus (Figure 4.2 f). A major type of lamellate imbricate pattern was observed on five species but the substructures are diverse: echinate pattern (*A. perthensis* and *A. ramsayi*), reticulate and echinate pattern (*S. diadema*), papillate structures (*M. spilota*), and echinostriate pattern (*N. atra*), which corresponds to Figure 4.2 g) - k), respectively. Figure 4.2 l) reveals another very different verrucate and polygonal juxtaposed pattern with a reticulate fine structure on *E. pyramidum*. Various micro-ornamentations are found on the dorsal scales of the investigated snake species, which might be used to achieve different functionalities according to their individual demands from the living environment.

Despite this, from the SEM images, one common characteristic of these micro-ornamentations is that most snake species exhibit at least two levels of hierarchical microstructures (*i.e.* major type and subtype) except *C. hortulanus* (Figure 4.2 c) and *P. guttatus* (Figure 4.2 f). Table 4.1 summarizes the detailed classification of the major and sub hierarchical patterns on the dorsal scales of the investigated snakes. The size of the microstructures at the same hierarchical level on different species varies moderately from hundreds of nanometers to several micrometers. This type of exquisite structural characteristic indicates dedicated functions such as excellent wettability or spectral regulating ability, which will be further examined in the following sections.

Table 4.1: Description of the hierarchical micro-ornamentations on the dorsal scales of the investigated twelve snake species.

Species	**Major pattern type**	**Subtype pattern**
S. miliarius	foveate with raised cell borders	reticulate and porous
B. arietans	foveate with raised cell borders	reticulate and porous
C. hortulanus	polygonal juxtaposed	none
V. aspis	canaliculated	crosshatching ribs and reticulate
M. monpessulanus	canaliculated	crosshatching ribs
P. guttatus	reticulate	none
A. perthensis	lamellate imbricate	echinate
A. ramsayi	lamellate imbricate	echinate
S. diadema	lamellate imbricate	reticulate and echinate
M. spilota	lamellate imbricate	papillate
N. atra	lamellate imbricate	echinostriate
E. pyramidum	verrucate and polygonal juxtaposed	reticulate

4.1.3 Spectacle scales

Besides the scales on the ventral and dorsal side, snakes also possess two special pieces of scales for covering and protecting their eyeballs, which are commonly called spectacle scales [162, 163]. As a window for the eye lens, the spectacle scale might be important for regulating light spectrum such as blocking detrimental light into the eye lens. In addition, the lack of movable eyelids as well as hands or feet impedes the snake cleaning their spectacle scales. No evidence has shown any specific behavior which indicates how snakes clean their eyes. Thus, self-cleaning capability is suspected on such scales. Both light spectrum regulating and self-cleaning abilities are usually appeared with typical microstructures on the surface.

Figure 4.3 summarizes the photos of the spectacle scales of two snake species as well as the SEM and AFM images revealing the microstructures on the surfaces. Two photos of the molted scales from the head of *V. aspis* (top image) and *B. arietans* (bottom image) are shown in Figure 4.3 a). In each photo, two spherical-shaped spectacle scales are observed at the location of the eyeballs. On each snake, the spectacle scales look more transparent than the surrounding scales, which indicates good spectral transmittance ability of the spectacle scales. If comparing between the two species, the size of the spectacle scales of *V. aspis* (about 4 mm in diameter) is slightly smaller than that of *B. arietans* (about 5 mm in diameter). Several reasons can be accounted for this difference, *e.g.*, their different age period or the original body size difference between the species. However, it is also interesting to note that the spectacle scales of these two species show similar appearance even though the scales in the surrounding areas display significantly different colors or patterns between them. This implies similar micro-ornamentations on the spectacle scales of different snake species.

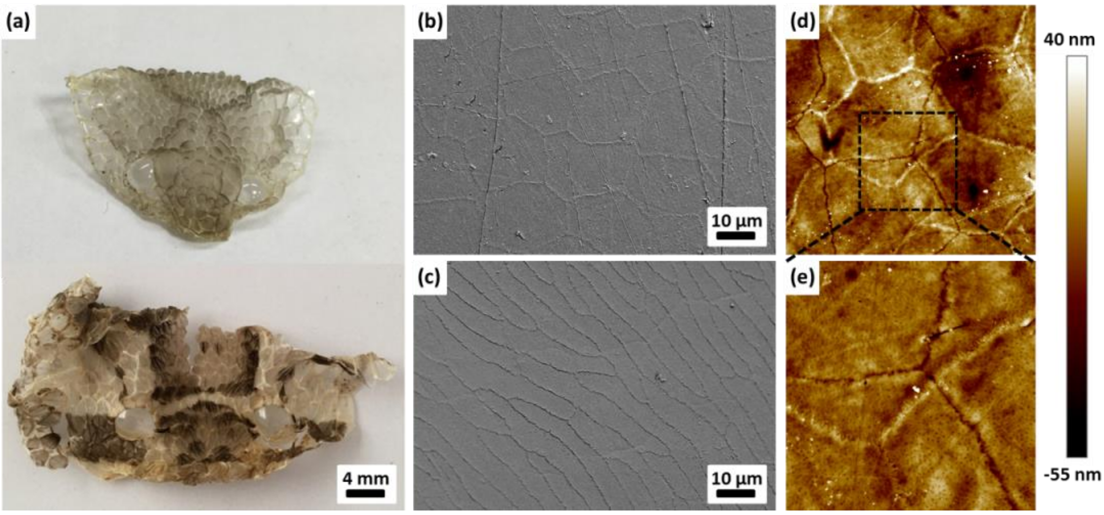

Figure 4.3: Photographs together with SEM and AFM images of spectacle snake scales. The photos of molted spectacle scales are from two species (*V. aspis* and *B. arietans*). The SEM and AFM images are from spectacle scales of a corn snake (*P. guttatus*) indicating the micro-ornamentations on the exterior surfaces. (a) Two transparent spectacle scales at the position of covering the eyeballs on the molted scales (head part only) of *V. aspis* (top image) and *B. arietans* (bottom image), respectively. SEM images reveal stitching pentagon or hexagon patterns on the spectacle scale of *P. guttatus*: (b) in the spherical central area and (c) at the edge region. Interesting narrow channels linking into polygon shapes are also observed in (c). (d) An AFM measurement on the same species (*P. guttatus*) shows a clear insight of the two different polygon borders: narrow channels and stitching boundaries. (e) The enlargement of a small area marked by the black dashed square in (d) shows micro-fibril structures at the stitching boundary, while these structures are not obvious at the narrow channels. Numerous nanoscale pits are also found on the surface. The scanning size of image (d) and (e) is 50 µm and 20 µm, respectively.

The micro-ornamentations on the surface of the spectacle scale of a corn snake (*P. guattatus*) are imaged by SEM. The results of the spherical central and edge area of the scale are summarized in Figure 4.3 b) and c), respectively. In the central area (Figure 4.3 b) stitching pentagon or hexagon micro-ornamentations are observed, while at the edge of the spectacle the polygon structures become stretched in the direction of perpendicular to the spectacle radius (Figure 4.3 c). The size of the polygon structures in the spectacle central region is about 20 µm - 30 µm in diameter. This is much larger than the micro-ornamentations on the ventral (less than 5 µm) and dorsal (hundreds of nanometers for the smallest hierarchical level) scales as reported before. Then at the edge of the spectacle scale, the polygon structures transform into a stretched shape with about 40 µm - 60 µm in length and 5 µm in width. Besides this, interestingly, in Figure 4.3 c) several narrow channels crossing the stitching polygon structures are observed and these channels are also linked into a polygon shape. A study which investigated the microstructures on the eye scales of Papua snake lizard (*Lialis jicare*) considers these two types of polygon structures as the borders of “Oberhäutchen” cells and clear layer cells from the shed overlaying skin, respectively [56]. No other specific functions are supposed regarding these polygon shape micro-ornamentations as polygons are usually found as basic elements of spherical-shaped objects.

To show more details of the two different polygon borders, a spectacle scale of the same corn snake was cut into small pieces (about 2 mm × 2 mm) and imaged by AFM with a sharp tip. Figure 4.3 d) and e) show the resulting images. In Figure 4.3 d), one can clearly see the narrow channels and the stitching boundaries of the polygon structures on the scale surface, which are shown as black and white borders in the image, respectively. This image coincides with the observations of the SEM images. A small area represented by the black dashed square in Figure 4.3 d) was rescanned by AFM to have a clear insight of the two different borders. An enlarged image of this area is shown in Figure 4.3 e). At the stitching boundaries micro-fibril structures similar to those on the ventral scales are observed, while at the channel border the micro-fibrils are not easily distinguishable. Most of these micro-fibrils are smaller than 1 µm in length, which are much smaller than that on the ventral scales. Finally, it is also interesting to observe that a huge number of nano-pits exists on the surface in Figure 4.3 e). These nanoscopic pits might be important for spectral functions such as enhancing the transmittance of the visible light spectrum into eye lens. Such type of investigation will be conducted in the following Chapter 4.5.

4.2 Cross section of inner-structures

The cross sectional design is important for the mechanical properties of snake scales [160]. Even though consisting of the same material, differences in cross section of snake scales may lead to a very different friction and wear performance during locomotion. Snakes native in different habitats probably evolved specifically individual cross section of inner-structure for the optimized tribological contacts with the substrates. Besides this, the thickness of the scales is also vital for wear properties. In general, on the same substrate, the thicker scales show less abrasive wear than the thinner ones due to the dissipation of the shear force in the deformations of thicker scales [160]. Thus, it is necessary to investigate the cross section as well as the thickness of snake scales. A comparison between the dorsal, ventral, and spectacle scales of two snake species was conducted.

Figure 4.4 summarizes the cross sectional design of these three types of regional scales from a Chinese cobra (*N. atra*) and a corn snake (*P. guttatus*), which are imaged by SEM. The image from top to bottom corresponds to the cross section of the dorsal, ventral, and spectacle scale, respectively. The left column displays the results from *N. atra* and images of *P. guttatus* are shown on the right side. In all images, parallel layered internal structures are observed. This is most apparent on their ventral scales (see Figure 4.4 c and d). However, the thickness of each single layer and the quantity of total layers differ for different regions of snakes (*i.e.* dorsal, ventral, and spectacle scales). It can be imagined that this kind of layered structures are able to show superior friction and wear performance in contrast to bulk materials, which is due to their potential ability of dissipating energies and forces with the help of several supportive layers under the outermost surface. Such effect has been widely reported on technical layered materials such as graphite [164-166] or MoS_2 [164, 167].

Ventral scales of both snake species show very typical multilayered structures in the cross sections. Several layers stacking one after another build up a type of fractured cross sectional structure (see Figure 4.4 c and d). Once external forces are exerted on the scale surface, this multilayered architecture might be beneficial to redistributing the pressure and ultimately reducing it into a minimum value at a certain interface (layer) [158, 160, 168]. This is very practical for snakes since they traverse on different types of terrains and sometimes on harsh substrates causing large pressure on their ventral scales due to their large body mass. It is also interesting to observe many similar tiny nano-pipes, inside which long fibers grow (about

0.5 µm - 1 µm in diameter), on the top layer (the most exterior layer) of ventral scales of both snakes. These nano-pipes and fibers are oriented along the body's longitudinal direction and are probably able to enhance the mechanical strength of scales in snake's locomotion direction. Nonetheless, these fiber-filled nano-pipes also indicate high elasticity when forces are applied normally onto the scale surface. Such an arrangement can disperse pressure on the body surface and protect the inner-body organs. The other layers loosely piled up beneath the top layer may also achieve the same function.

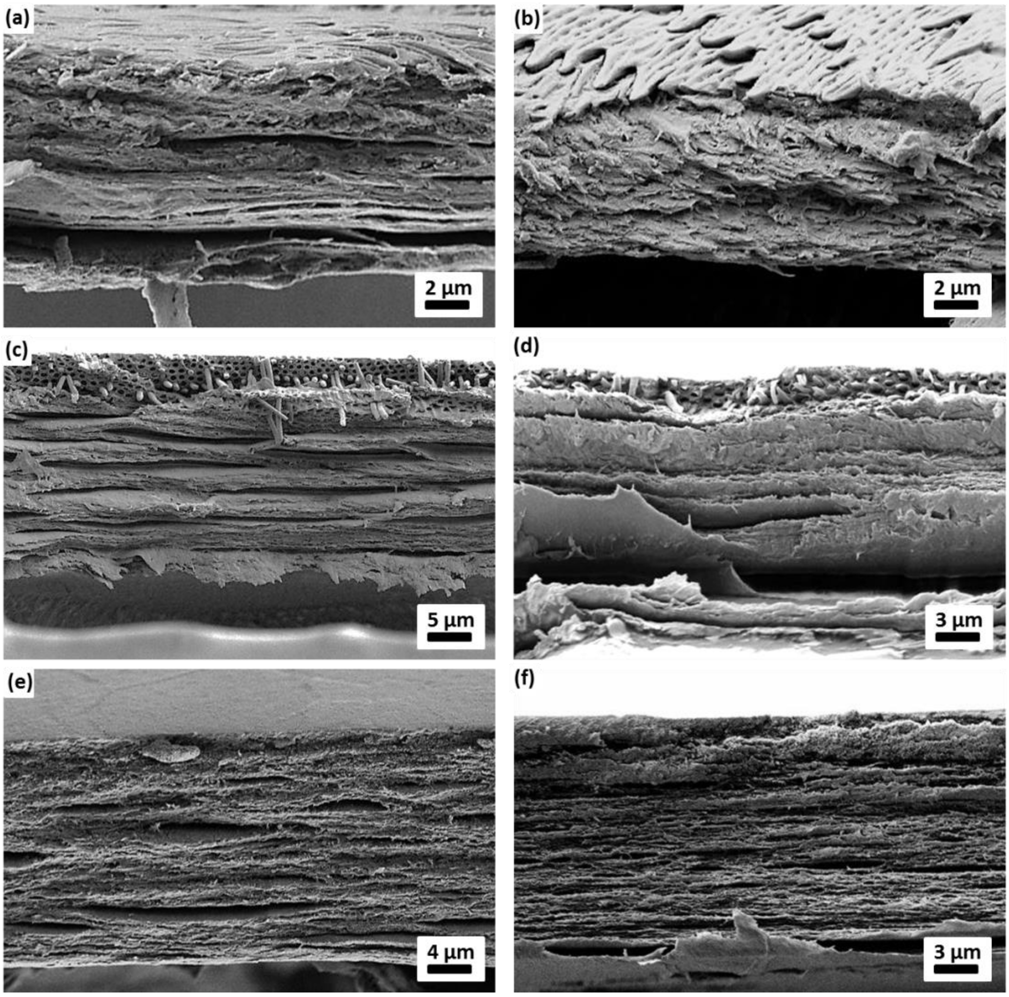

Figure 4.4: SEM images show the cross sectional design of snake scales. The dorsal, ventral, and spectacle scales of *N. atra* (left) and *P. guttatus* (right) were examined. (a) and (b) show the results of the dorsal scales of the two species. On *N. atra* the cross section displays a multilayered structure, while *P. guttatus* does not show a very apparent layered cross section. (c) and (d) are the ventral scales demonstrating a similar, typical multilayered structure on the two species. (e) and (f) show the spectacle scales with more compact layered structures than the ventral scales. The top of each image represents the most exterior surface of each snake scale.

The cross section of the dorsal scales of two snake species are a little bit different (see Figure 4.4 a and b). Similar to its ventral scales, Chinese cobra (*N. atra*) also features loosely stacked, multilayered structure in its dorsal scales. However, no nano-pipes or inside nano-fibers are observed on the exterior layer and the quantity of the layer is less than that on the ventral scale. On *P. guttatus* dorsal scale, the cross section does not reveal a layered structure and looks more compact than the dorsal scale of *N. atra*. This outcome is reasonable as the dorsal scales are not in direct contact with the substratum and usually endure much less friction and wear than their ventral scales. However, the layered structures on the dorsal scale might be also helpful for increasing the flexibility of the snake skins.

Figure 4.4 e) and f) show the SEM images of the spectacle scales of the two snake species revealing very similar cross section. The inner structure of this type of scale appears to be very compact demonstrating many thin layers closely clinging to each other. This compressed structure might be important for providing high hardness as a mechanical protection for the eye lens. Besides this, it is also probably beneficial to the enhancement of the spectral transmittance as loose cross sectional architecture would significantly scatter the light going into the eye lens. The existed gaps between the layers in the image might be enhanced or produced during the cutting process for the preparation of samples for SEM imaging. The spectral transmittance properties of spectacle snake scales will be examined in the following Chapter 4.5.

In addition, if comparing between the dorsal, ventral, and spectacle scales of the same snake, it is interesting to note that the thickness of the scales differs among the regions of the same snake. Moreover, both snake species exhibit a similar trend: the ventral scale is the thickest (30.2 µm and 18.7 µm for *N. atra* and *P. guttatus*, respectively), then the spectacle scale is slightly thinner (20.1 µm and 16.3 µm), and the dorsal scale is the thinnest (9.8 µm and 6.9 µm). As already mentioned before, a thicker surface would withstand less abrasive wear. The large thickness of ventral snake scales, therefore, can help to improve the wear resistant ability of snakes when traversing on complicated, tough terrains. The dorsal snake scales are normally not used for anti-wear purpose, thus the thickness of this type of scale is comparably small. This can also increase the flexibility of snake body for other purposes such as the body curvature for camouflage or predation. Snakes might need the intermediate thickness for the aim of enhancing the mechanical hardness of spectacle scales to protect the eye lens from possible damages (*e.g.* shrubs or sand grains).

4.3 Wetting properties

Although equipped with the smallest thickness leading to poor tribological capability (*e.g.* wear resistance) in contrast to ventral and spectacle scales, dorsal snake scales feature more exquisite, hierarchical microstructures on their external surface. This suggests a fascinating interfacial function of this type of scale. Moreover, the diverse, hierarchical microstructures on different snake species indicate dedicated functions for individual tasks according to the demand for adapting to the respective habitat. For example, self-cleaning (anti-contamination) [63, 64] or water-harvesting [62] properties can be expected on surfaces with such complicated micro-ornamentations. Thus, the wettability should be examined on the dorsal scales of snakes. Moreover, to answer the question how snakes clean their eyes without extremities or movable eyelids, which was discussed in the Introduction, checking the wettability of snake spectacle scales is also of high interest. Therefore, a series of water contact angle measurements was conducted on the dorsal, ventral, and spectacle scales of all snake species to investigate their wetting properties. A comparison between the results of these different scales was made.

Figure 4.5 shows the images of a 1 µL water droplet on the exterior surface of a single dorsal, ventral, and spectacle scale of the snake *S. miliarius*, which reveals that the equilibrium contact angles on the corresponding scales are 143°, 111°, and 103°, respectively. The droplet was placed on flat dorsal or ventral scales to measure the contact angle, while for the spectacle scale the droplet was carefully dropped onto the spherical top of an intact scale. The results show that the dorsal scale of *S. miliarius* is more hydrophobic than the scales from the other regions. The chemical composition of the scales in different regions of the same snake is supposed to be similar. Thus, the difference of contact angle on different regional scales is very likely caused by the microstructures on their surface. The foveate (basin shape) pattern with reticulate and porous structures on the dorsal scale helps *S. miliarius* to achieve a comparably large water contact angle on the exterior surface, possibly realizing a self-cleaning function. On the ventral scales, however, the oriented micro-fibril structures do not show the same ability. It is also interesting to note that the water contact angle on the spectacle scale is the smallest among the three values. It seems that the spectacle scales of *S. miliarius* do not possess self-cleaning capability. Besides this, a side-view camera shows a similar shape of water droplet (see the inset image in Figure 4.5 c) as front view demonstrating an isotropic wetting property. All these results show a normal wettability on the exterior surface of *S. miliarius* spectacle scales.

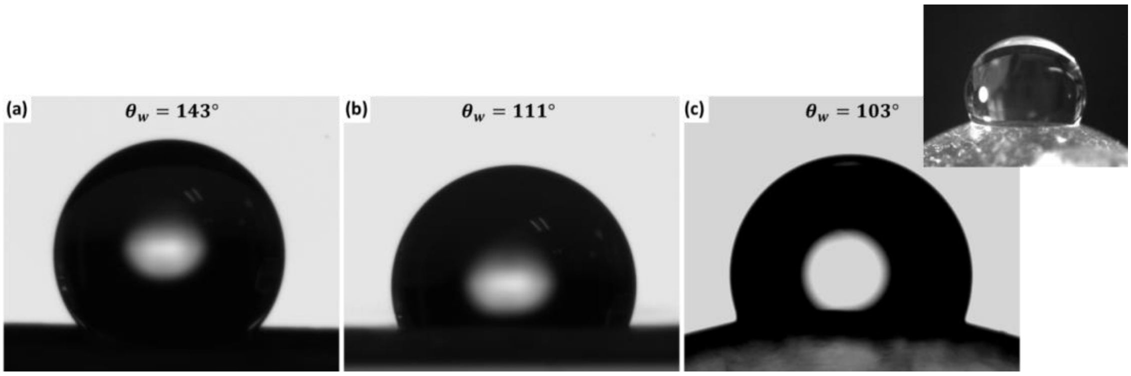

Figure 4.5: Contact angle measurements on the molted scales of *S. miliarius* in different regions. (a) On a flat dorsal scale. (b) On a flat ventral scale. (c) On the spherical top of an intact spectacle scale. The inset graph in (c) is an image of the water droplet on the same spectacle scale obtained by a side-view camera revealing an isotropic wetting property. The droplet volume is 1 µL.

Furthermore, the same experimental procedure was repeatedly conducted on the other eleven snake species. Singled dorsal, ventral, and spectacle scales of each snake were examined except that some scales are too small to drop a water droplet onto the surface (*i.e. E. pyramidum*). No samples of *C. hortulanus* spectacle scale were obtained. The results of all the investigated samples are shown in Table 4.2. Twelve measurements were conducted on each sample and the averaged values together with the statistic errors were calculated. One can see that, for all the investigated snakes, the water contact angles on the dorsal scale (ranging from 121° to 145° according to different species) are larger than those on the ventral side (98° - 118°). The smallest values are observed on the spectacle scales (89° - 104°).

Regarding the results on the dorsal scales of each snake species, *B. arietans*, *S. miliarius*, and *V. aspis* show the most hydrophobic dorsal scales with an average contact angle of above 140°. Similar hierarchical microstructures (foveate patterns with reticulate and porous structures, see Figure 4.2 a and b) produce a hydrophobic surface on the dorsal scales of *S. miliarus* and *B. arietans*, leading to almost equal contact angle values on these two species. However, the same effect does not appear on *V. aspis* and *M. monspessulanus*. Although they feature similar microstructures (see Figure 4.2 d and e), the contact angle on *V. aspis* (141°) is slightly larger than that on *M. monspessulanus* (130°). In addition, a relatively larger contact angle value on the ventral scales of *M. monspessulanus* is observed if compared to other species. It seems that snake *M. monspessulanus* has special wetting properties on its scales for individual purpose. The least hydrophobic dorsal scales are found on three species, which are *N. atra*, *S. diadema*, and *C. hortulanus*, respectively. The contact angles on these three snakes locate between 120° and 130°. The values for the other snakes range from 130° to 140°.

Interestingly, most investigated snake species exhibit water contact angles of around 110° on their ventral scales except *A. ramsayi* (102°), *M. monpessulanus* (118°), and *C. hortulanus* (98°). Among them, *A. ramsayi* and *M. monpessulanus* show micro-fibril structures on their ventral side, which are similar to the other snakes (those with around 110° contact angle on the ventral scales). The ventral scales of these two snakes might possess some special chemical composition causing the slightly different contact angles. Nonetheless, *C. hortulanus* shows very different micro-ornamentations on its ventral side (see Figure 4.1 h). The smaller values on this snake might be caused by the reticulate structures on its ventral scale through which the water can probably seep into the scales, leading to a small contact angle on the surface. To recapitulate, the micro-fibril structures on ventral snake scales are not as excellent as the hierarchical microstructures on the dorsal scales in terms of enhancing water contact angle on the scale surface for self-cleaning utilization. These micro-fibril structures should be responsible for the other functions.

Table 4.2: Water contact angle values on the scales of twelve snake species. On each snake, the exterior surface of the dorsal, ventral, and spectacle scales was examined, respectively.

Species	Dorsal	Ventral	Spectacle
S. miliarius	143 ± 5°	111 ± 3°	103 ± 3°
B. arietans	145 ± 3°	109 ± 4°	104 ± 2°
C. hortulanus	121 ± 4°	98 ± 8°	-
V. aspis	141 ± 4°	111 ± 1°	103 ± 1°
M. monpessulanus	130 ± 7°	118 ± 5°	101 ± 3°
P. guttatus	133 ± 2°	108 ± 1°	98 ± 6°
A. perthensis	135 ± 5°	110 ± 2°	89 ± 4°
A. ramsayi	133 ± 4°	102 ± 6°	*
S. diadema	126 ± 5°	109 ± 2°	96 ± 6°
M. spilota	134 ± 6°	108 ± 2°	92 ± 2°
N. atra	122 ± 4°	111 ± 1°	102 ± 2°
E. pyramidum	*	*	*

* the sample scales were too small to get reliable results.

\- no sample scales were available.

Ultimately, the contact angles on spectacle scales are not as high as on dorsal scales. With two exceptions of *A. perthensis* and *M. spilota* showing slightly smaller values (89° and 92°, respectively), most snakes show a water contact angle of around 100°. This effect is similar to that on ventral scales (110°) but with a smaller value. This outcome also coincides with the micro-ornamentations on scales. Most snakes show similar microstructures on their ventral scales (micro-fibril structures) or spectacle scales (polygon like structures) leading to a similar contact angle value on the surface, respectively. However, the various micro-ornamentations on the dorsal scales of different snakes cause a wide variation of contact angles on the surface according to individual demands. To conclude, the dorsal scales of some snakes (*i.e.* those with high contact angles) might be able to self-clean, but the ventral and spectacle scales are not decorated for this function.

4.4 Adhesion properties

As shown in Chapter 2.1.1, a large water contact angle corresponds to a low adhesion energy (force) of the surface material [92, 95, 96]. Thus, the contact angle results can be confirmed by measuring the adhesion forces on the scale's surfaces. To achieve this, adhesion forces of a sharp AFM tip (made from silicon) interacting with the dorsal, ventral, and spectacle scales of all the investigated snake species were recorded. On each sample 10 arbitrary positions were measured and at each position 10 measurements were repeatedly conducted. The adhesion force on each sample was calculated from the force vs. distance curve obtained in each measurement and averaged from the total of 100 measurements. Figure 4.6 summarizes the results of the twelve snake species.

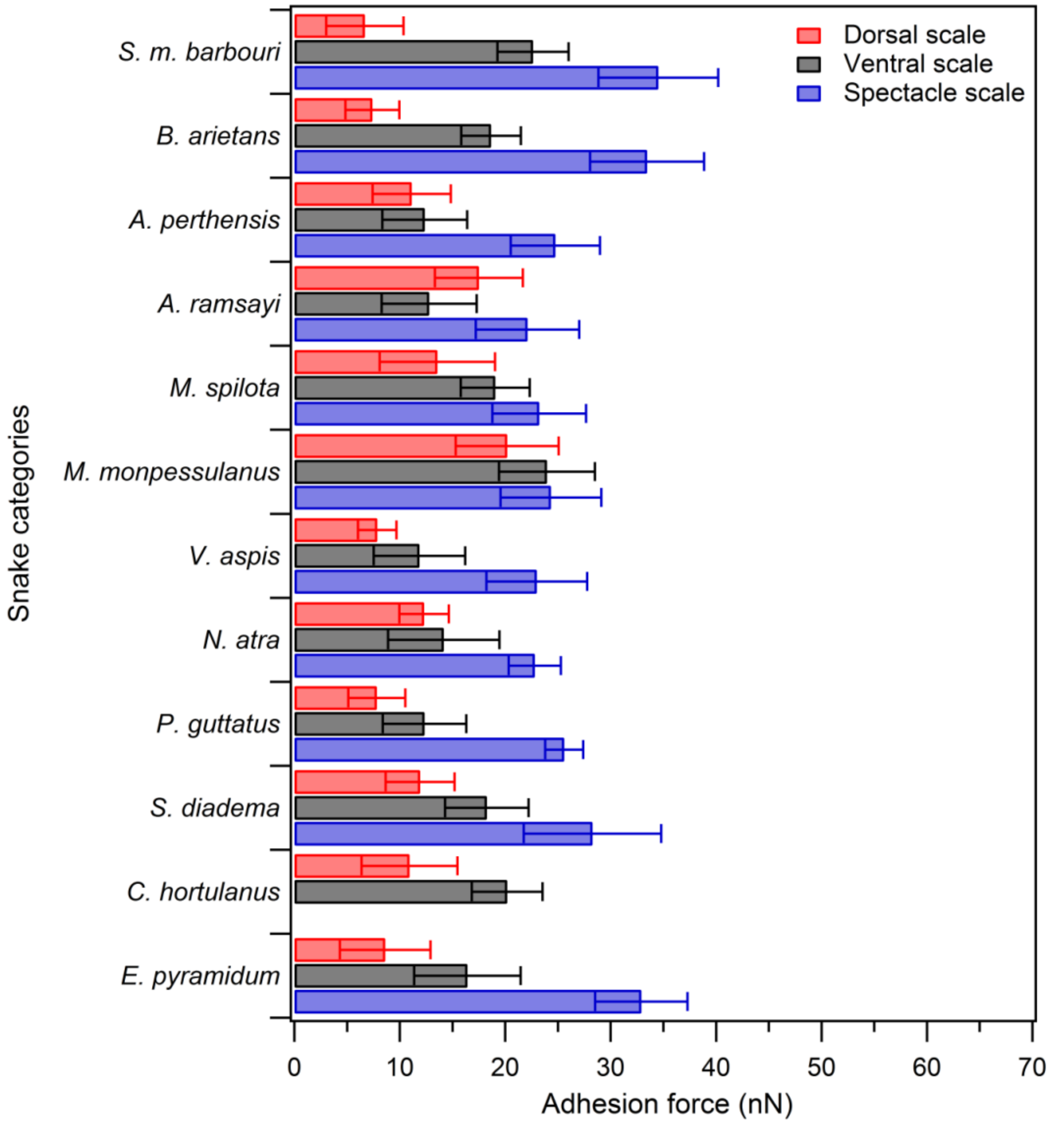

Figure 4.6: Adhesion forces of a sharp AFM silicon tip interacting with snake scales. The dorsal, ventral, and spectacle scales of twelve snake species were examined. On each sample, the adhesion forces were measured at 10 arbitrary positions and 10 measurements were repeated at each position. The resulting adhesion force of each sample was averaged from all 100 measurements and the error bars correspond to the respective statistical error. Comparably large adhesion values are found on the spectacle scales while those on the dorsal scales are very small. There is no data for the spectacle scale of *C. hortulanus* due to the lack of this sample.

For all the investigated snakes except *A. ramsayi*, a similar trend is observed in Figure 4.6, *i.e.*, on each snake the measured adhesion forces are the largest for the spectacle scales while they are smallest for the dorsal scales. The values obtained on the ventral scales are between these two groups. The adhesion forces on the ventral and spectacle scales of *M. monpessulanus* are very close to each other. For *A. ramsayi*, the adhesion forces on the dorsal scales are larger than that on the ventral scales but still not as large as that on spectacle scales. Nevertheless, this outcome, revealing a common trend of adhesion properties of the scales in different regions of snake body, also coincides with the contact angle results in the last section. Both adhesion and contact angles indicate a possible self-cleaning capability existing on the dorsal scales of snakes. However, the spectacle scales do not possess this ability and their performance is even not as good as the ventral scales. Besides this, if comparing the results of the same type of regional scales between different snake species, one can find various adhesion performances even though all the measurements in

Figure 4.6 were conducted with the AFM tips from the same batch. The adhesion forces on dorsal scales of different snakes are close to each other. The values for most snakes are less than 13 nN whereas *A. ramsayi* and *M. monpessulanus* show slightly larger results (nearly 20 nN). Spectacle scales exhibit a similar trend as dorsal scales. The adhesion forces on most snake species are around 25 nN except three species (*S. miliarius*, *B. arietans*, and *E. pyramidum*), which show the values of more than 30 nN. As for ventral scales, the adhesion forces are fluctuating for different species and can be roughly divided into two main groups: around 10 nN (*A. perthensis*, *A. ramsayi*, *V. aspis*, *N. atra*, and *P. guttatus*) and around 20 nN (all other species).

4.5 Spectral transmittance properties

It is unexpected that spectacle scales of the investigated snakes feature such comparable high adhesion and small contact angles preventing wet self-cleaning. This means that snakes cannot easily clean their eyes unless they shed the old scales and replace them by the new ones. Nonetheless, this is also reasonable as self-cleaning properties are always happened with complicated, exquisite microstructures (*e.g.* microstructures on the dorsal scales), which usually reduce the spectral transmittance of the scale causing diminution of vision. It can be assumed that snakes might have to abandon self-cleaning ability for obtaining a better spectral visibility on their spectacle scales during the long time of environmental selection. Hence, in order to verify this assumption, the spectral transmittances of the dorsal, ventral, and spectacle scales of eight snake species (the name of each species is indicated in each sub-image) were investigated and summarized in Figure 4.7.

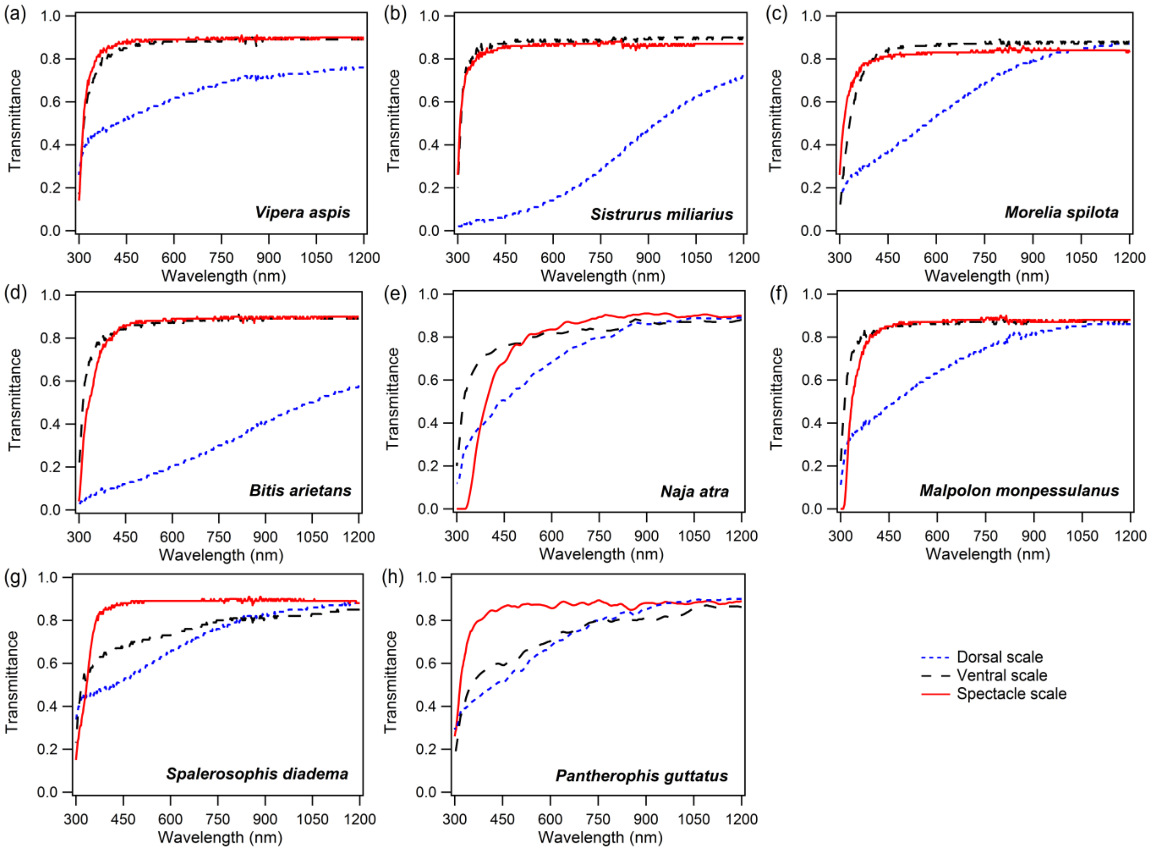

Figure 4.7: Spectral transmittances of the molted scales from eight different snake species. The specific name of each snake is indicated in the lower right corner of each sub-image. The dorsal, ventral, and spectacle scales were examined on each snake.

The investigated wavelength is in the range of 300 nm - 1200 nm. The characterizing resolution for most snakes was 2 nm while for *N. atra* and *P. guttatus* it was 5 nm.

It can be seen that on the dorsal scales of all investigated snakes the spectral transmittances manifest a gradual decreasing relationship with lower wavelengths. One possible reason for this outcome might be the scattering effects of the complicated micro-ornamentations on their surfaces. Although displaying various microstructures, the dorsal scales of different species show a very similar spectral transmittance pattern. The transmittances of spectacle scales show another general pattern among the eight investigated snakes. In difference to the dorsal scales, they remain a constantly high transmittance (nearly 90%) in visible light and near-infrared spectrum, while the value will reduce significantly once the wavelength reach the range of ultraviolet spectrum. Regarding the ventral scales, most snakes (see Figure 4.7 a - f) show very indistinguishable spectral transmittance as their spectacle scales with an exception of two species (*S. diadema* and *P. guttatus*). The results of ventral scales of both snakes exhibit a similar trend as their dorsal scales (Figure 4.7 g and h).

For almost all curves in Figure 4.7, a cutoff in the ultraviolet spectrum exists, below which the transmittance decreases sharply to less than 30%. This outcome is particularly typical for the spectacle scales. For three snake species, the transmittance of spectacle scales reaches nearly 0% (*B. arietans*) or is completely blocked (*N. atra* and *M. monpessulanus*) when the wavelength reduces to 300 nm. The dorsal scales of *S. miliarus* and *B. arietans*, which are black colored in most areas, do not show cutoff pattern but display a gradually decreasing transmittance until reach nearly 0% at the wavelength of 300 nm. Extremely low transmittance in the ultraviolet spectrum is found on all the regional scales. This indicates a function of anti-ultraviolet to protect snake skin as well as the inner organisms from the harmful solar radiation. Among them, dorsal scales are directly exposed under sunlight and receive more solar radiation than the other scales. Thus, they are good at scattering light to reduce the radiation within the investigated spectrum. The spectacle scales are important for snake’s vision. A study investigating the visual pigment genes of snakes [76] reported that snakes are dichromatic and can see two primary colors, *i.e.*, blue and green (corresponding to 470 nm - 560 nm wavelength). In this case, the spectacle scales function as a high pass filter allowing the visible light and near-infrared spectrum going into the eye lens while cutting down the harmful ultraviolet spectrum. The ventral snake scales are in contact with the substratum for most of time, which do not have necessary requirements for high spectral transmittance. However, it is interesting to note that the ventral scales of most snakes show a similar spectral transmittance pattern as their spectacle scales. This might be due to the micro-ornamentations on the scale surfaces, *i.e.*, the microstructures on the dorsal scales are capable to scatter light while those on the ventral and spectacle scales cannot achieve the same functionality. As a result, the ventral scales show the same high spectral transmittance as spectacle scales.

4.6 Functions of snake dorsal, ventral, and spectacle scales

The structural properties including micro-ornamentations on scale topography and cross section of innerstructures were investigated on the dorsal, ventral, and spectacle scales of twelve snake species by SEM. For an individual snake, the micro-ornamentations on the surfaces of its different regional scales were found to be totally different. This indicates that the scales in different regions of snake body are probably equipped with different functions. Interestingly, if comparing between different snake species, the dorsal scales of different snakes show diverse micro-ornamentations. However, on the ventral scales (oriented micro-fibril structures) as well as on the spectacle scales (stitching polygon structures) the microstructures on the same regional scale are very similar for most investigated snakes. The cross sectional architecture of all the regional scales (*i.e.* dorsal, ventral, and spectacle scales) shows similar stacked layered structures, while the respective quantity of the layers is very different. On the same snake, the thickness of ventral scale is nearly three times as that of its dorsal scale. This reveals better frictional and wear resistant properties on ventral snake side. Therefore, the differences of the topographical microstructures and cross sectional inner-structures between the dorsal, ventral, and spectacle scales of the same snake imply multi-functional abilities on these scales. Moreover, the similarity of the structural characteristics on the same regional scales between different snake species indicates a general principle of these multi-functional abilities.

Although widely discussed, the function of dorsal snake scales has not reached a unanimous agreement. Previous studies showed several examples of dorsal snake skin functioning as light filter [41, 60], color enhancement [61], or anti-wetting surface [44, 64]. Diverse micro-ornamentations found on different snake species indicate dedicated functions for individual snakes in order to better fit into their living surroundings. Water contact angle on the exterior surface of dorsal scales of different snake species varies in the range of 120° - 145°, while the results on the ventral and spectacle scales are relatively stable at the value of around 110° and 100°, respectively. Measurements of adhesion forces through a sharp AFM tip interacting with the scale surface also show a same trend as the contact angle results. Hence, the dorsal part of snakes is more likely to possess a self-cleaning or anti-contamination ability if compared to the scales in the other regions. Contact angles of more than 140° were even observed on three species (*V. aspis*, *S. miliarus*, and *B. arietans*). Besides this, dorsal snake scales also show the capability of scattering light in the examined spectrum of 300 nm - 1200 nm wavelength. A reduction of spectral transmittance for decreasing wavelength was observed. This property might protect the snake skin as well as its inner organism from the everyday solar radiation. Especially for *S. miliarus* and *B. arietans*, the spectral transmittance of their dorsal scales is lower than 20% within most part of the visible light spectrum and even reaches nearly zero in ultraviolet spectrum.

As for the function of the micro-fibril structures on ventral snake scales, the water contact angle on this type of scales indicates a “normal” wettability (110°) without self-cleaning property. Although most snakes show high spectral transmittance on their ventral scales (similar to their spectacle scales), no spectral related functions can be imagined since they are in direct contact with the substratum for most of time. On this account, the most widely accepted theory of the function of ventral snake scales so far is to improve frictional properties like friction anisotropy [49-52, 65] during snake’s locomotion. Australia pythons (*A. perthensis*, *A. ramsayi*, and *M. spilota*) even feature more delicate, hierarchical micro-fibril structures on their ventral scales. Due to the small size of their micro-fibrils, they have more quantities of fibrils in contact with the substratum for the same contact area. This might allow them to show a more refined frictional performance during locomotion. A detailed analysis of the friction anisotropy on ventral snake scales as well as the relationship between friction anisotropy and the micro-fibril structures will be presented in the following Chapter 5. In difference to most investigated snakes, *C. hortulanus* shows a reticulate structure with longitudinal oriented ridges on their ventral scales. Some studies [65, 160] investigated the frictional properties of this species by a self-built friction angle tribometry and found a smaller friction coefficient on its ventral scale than on its dorsal and lateral side. Moreover, a slight friction anisotropy in moving forward and backward directions was also reported [65].

Spectacle scales are initially suspected with self-cleaning properties considering that snakes do not have extremities or movable eyelids to wipe eyes by themselves. However, unexpectedly, water contact angle examination on the spectacle scales of twelve snake species only shows a contact angle of around 100°, which is much smaller than the results on the dorsal scales (120° - 145°) and even smaller than that on the ventral scales (around 110°). Adhesion force measurements using a sharp AFM tip interacting with the dorsal, ventral, and spectacle scales of the investigated snake species also coincide with this outcome. It seems that snakes cannot self-clean their spectacle scales. They have to renew their dirty spectacles by the periodically molting behaviors when necessary. As a window for the eye lens, spectacle snake scales might possess another potential ability of filtering harmful light spectrum (*e.g.* ultraviolet) or enhancing the transmittance of visible light. Snakes probably choose to sacrifice self-cleaning capability to achieve desirable spectral transmittance through the long time of evolution because self-cleaning property usually arises with exquisite and complicated micro- or nanostructures, which might reduce the spectral transmittance of the scale. The measurements of the spectral transmittance on the spectacle scales of eight snake species reveal a relatively high transmitting value (nearly 90%) within the visible light and near-infrared spectrum. In the ultraviolet spectrum, however, a cut-off was frequently observed, below which the transmittance reduces significantly to lower than 30%. Therefore, it can be concluded that spectacle snake scales featuring very simple, flat topography causing poor self-cleaning property to obtain better spectral visibility in visible light and near-infrared spectrum and more importantly, to filter the harmful ultraviolet into eye lens.

A shortened version of this chapter is in preparation as the article "Multifunctional snake scales: the structural property, wettability, and spectral transmittance of the dorsal, ventral, and spectacle scales of twelve snake species", by Weibin Wu, Felix Buck, Shudong Yu, Richard Thelen, Guillaume Gomard, and Hendrik Hölscher.

5 Friction anisotropy caused by step structures on snake and sandfish scales

From the analysis of last two chapters, an interesting, common structural characteristic can be observed on the topography of snake and sandfish scales, *i.e.*, both snakes and sandfish possess nanoscale step structures on their scale surfaces. The ventral scales of most snakes feature micro-fibril structures with several distributed nanoscale steps (see Figure 4.1) and the dorsal scales of sandfish show comb-like nano-step structures (see Figure 3.2 a). Considering that both types of scales play an important role as a tribological interface during their locomotion, the cognate step structures on their scales might function as a typical component for advanced frictional properties. This suggests a universal principle of reptiles (at least for snakes and sandfish) optimizing friction for locomotion. Several prior studies have reported friction reduction or friction anisotropy on ventral snake skins [45, 65, 169, 170]. However, only a few publications correlated the frictional performance of snake skins to the corresponding microstructures on their surface [31, 52, 69]. The studies focusing on the frictional performance of nano-step structures on snake or sandfish scales were even less [47, 49]. In this chapter, therefore, a detailed frictional analysis of the step structures of ventral snake scales and dorsal sandfish scales was conducted by AFM to determine their function on the nanoscale.

5.1 Nano-step structures on snake and sandfish scales

The micro-ornamentations on both ventral snake scales and dorsal sandfish scales, although having a different appearance, can be simplified as a similar type of nano-step structure. Figure 5.1 a) shows the AFM images of the micro-fibril structures on the ventral scales of the snake *N. atra*. Oriented, discrete micro-fibrils are evenly distributed on the surface. Each fibril shows two end-points. At the left end-point (fibril tip, see Figure 5.1 a), an extremely steep nano-step is demonstrated from the fibril top surface to the bottom base surface. The other end-point (right end-point), however, only shows a gradual slope (ramp shape) from top to bottom. A more detailed description can be seen in the inset image of Figure 5.1 a). This anisotropic structural characteristic might be the potential reason for the above-mentioned friction anisotropy on ventral snake scales. Moreover, the steep step ends are always oriented towards the tail of snakes. If several fibrils arranged in the same line along the snake body were considered, a small particle moving from the snake's tail to the head would need to overcome the extremely steep steps at these fibril tips (upward the step direction). On the contrary, if the particle moved from the snake's head to the tail (downward the steps), it would only need to "climb" the gentle slopes, which will be much easier. This indicates that the nano-steps at the micro-fibril ends help snakes to increase friction for backward motion, in other words, to enhance traction and avoid slipping in their forward motion. In difference to snakes, the step structures on dorsal sandfish scales are continuously located and feature a larger step height than snake scales (Figure 5.1 b). As a result, a more advanced frictional function can be imagined. Nonetheless, a detailed, nanoscale comprehension of step structures and their frictional performance on both snake and sandfish scales is needed. Such an analysis will be helpful for validating the assumptions made above as well as for further clarifying the mechanisms how snakes and sandfish manipulate friction during locomotion. Therefore, in the next sections the friction anisotropy on ventral snake scales and dorsal sandfish scales will be characterized by micro-tribometry and AFM.

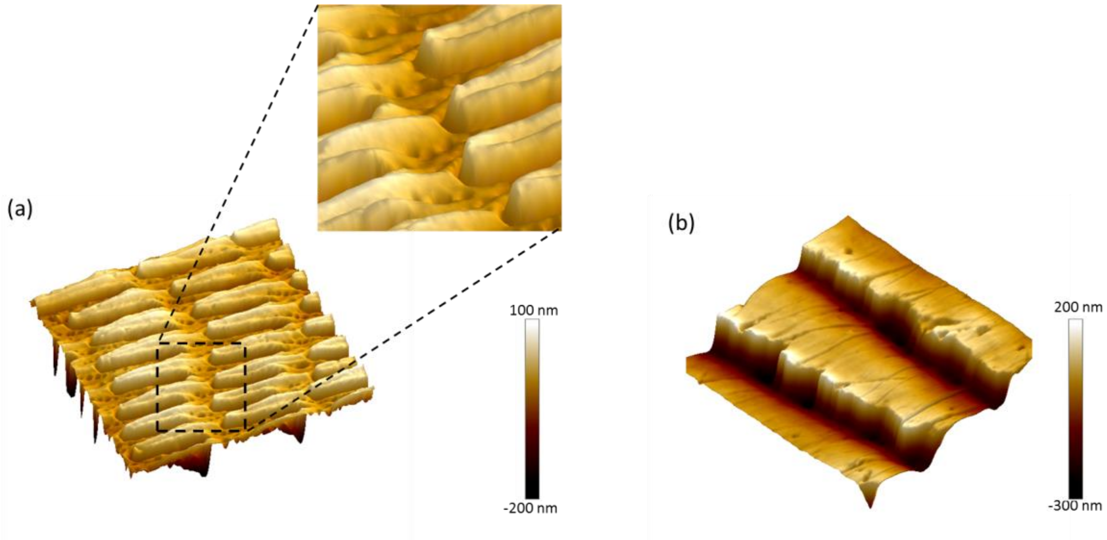

Figure 5.1: AFM images showing nano-steps on ventral snake and dorsal sandfish scales. (a) Micro-fibril structures on snakes with extremely steep nano-steps at fibril tips (see the inset image). (b) Continuous step structures on sandfish scales. Scan size of both images is 10 µm.

5.2 Friction anisotropy on ventral snake scales characterized by micro-tribometry

As reported before, friction anisotropy is frequently found on ventral snake scales [49-52, 65]. However, very few studies show evidence proving if this friction anisotropy is caused by the material properties of the snake's integument or the micro-fibril structures on the scale surface. A suitable method to answer this question is to fabricate micro-fibril structures on a technical surface and check the friction anisotropy. Compared to metals or other materials, polymers have the advantages of easy manufacturing and low prices. In our case, a polymeric replica, which means a polymer surface with micro-fibril structures replicated form ventral snake scales, was fabricated with a UV-curing optical adhesive (NOA 88). Furthermore, as a reference for comparison, a flat NOA 88 surface was prepared by imprinting a flat PDMS mold into the polymer. The friction anisotropy on the ventral scales of seven snake species together with a polymeric replica and a flat reference was characterized to verify:

1. The existence of friction anisotropy on ventral snake scales.
2. The causation of friction anisotropy due to structural properties of the micro-fibrils or material properties of snake scales.

5.2.1 Replication of snake fibril structures on polymer surface

A soft lithography technique was used to replicate the snake micro-fibril structures into a NOA 88 polymer layer [154] as described in Chapter 2.4.2. A polydimethylsiloxane (PDMS) mold containing the negative pattern of micro-fibril structures was first fabricated and then utilized to transfer the microstructures onto a NOA 88 surface. A small piece of ventral scale from *N. atra* was cut to 10 mm × 7 mm and fixed on a silicon wafer by a double-sided adhesive tape. An aluminum container was placed onto the silicon wafer leaving the fixed snake scale at the center. A mixture of Sylgard Silicone Elastomer 184 and its Curing Agent 184 (weight ratio of 10:1) was stirred evenly in ambient air and then placed into an evacuated desiccator. After 20 min, the air bubbles in the mixture were completely removed and the mixture was slowly poured onto the snake scale in the aluminum container. After that, the whole setup was put on a hotplate with a constant temperature of 45 °C for 10 hours without applying any pressure. The low temperature and no pressure conditions allow a slow curing process but avoid damaging the snake scales. The hardened PDMS mold was separated from the scale and cleaned by an ultrasonic bath with isopropanol to remove scale remnants. A droplet of about 50 µL NOA 88 was dripped on a glass slide, into which the hardened PDMS mold was carefully pressed to avoid air bubbles in the replica. After 20 min of UV exposure at 1.5 mW cm^{-2} UV radiation power, the cured NOA 88 replica of *N. atra* scale was obtained by the subsequent separation of the PDMS stamp. The replication quality of the surface was checked by AFM imaging and will be shown in the following Section 5.3.3. Figure 5.2 shows a photography of the *N. atra* scale used for replication, the PDMS mold, and the corresponding NOA replica on a glass slide from left to right.

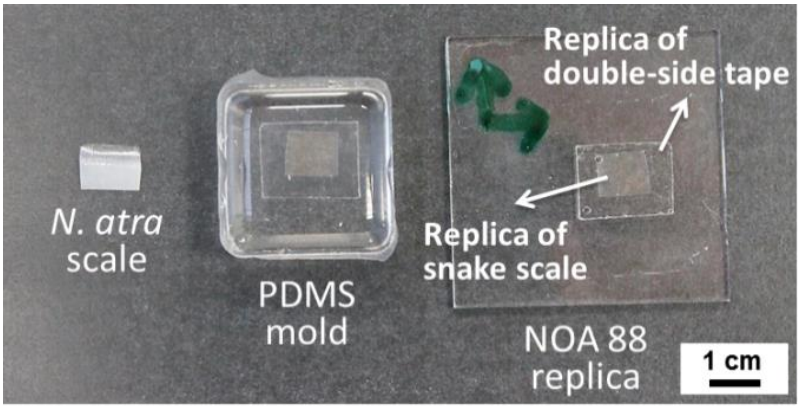

Figure 5.2: A side-by-side comparison of the snake scale, PDMS mold, and the replica. From left to right are the original, rectangular-cut *N. atra* ventral scale, the PDMS mold with negative micro-fibril structures, and the NOA 88 replica on a glass slide, respectively.

5.2.2 Friction anisotropy characterization

Friction anisotropy was characterized on the surface of various samples including ventral scales of seven snake species (*A. ramsayi*, *V. aspis*, *S. miliarius*, *B. arietans*, *N. atra*, *S. diadema*, and *P. guttatus*), a polymeric replica of *N. atra* ventral scale, and a flat polymeric reference with a reciprocating linear micro-tribometer. A 2 mm diameter, polished sapphire sphere (Saphirwerk AG, Bruegg, Switzerland) was used to pair against the samples. The normal load applied on all the investigated surfaces was kept as 0.5 N. The reciprocating stroke and sliding speed was set to 8 mm and 0.5 mm/s, respectively. Single, rectangular-cut ventral scales of seven snake species were fixed on a silicon wafer with double-sided adhesive tapes. The polymeric replica of *N. atra* ventral scale was obtained with the soft lithography technique mentioned above. The flat NOA 88 reference was imprinted with a flat PDMS mold by the same method. In difference to the frictional measurements described in Chapter 3.4.2, the friction anisotropy was characterized by measuring the friction on each sample in two opposite orientations (before and after turning the sample of 180°). For each sample orientation the results for the tribometer sliding in both trace and retrace directions were recorded. In this case, the frictional forces along the same sample/micro-tribometer moving direction were averaged in order to eliminate the friction deviation of the micro-tribometer reciprocating movement in trace and retrace direction. For each sample orientation, three reciprocating lines on different positions were measured and along each line five reciprocating cycles in both trace and retrace directions were conducted. The friction coefficients for the same sample/micro-tribometer moving direction were averaged and compared between the snake moving forward and backward direction. The results are summarized in Table 5.1. For all the tests, the temperature (22±1 °C) and humidity (45±5%) were controlled.

Table 5.1: Summary of the friction coefficients on snake scales moving in forward and backward direction. All the results were recorded with a reciprocating linear micro-tribometer and reveal friction anisotropy on the ventral scales of seven snake species and on a polymeric replica surface.

Samples	**Moving forward**	**Moving backward**	**Difference (abs.)**	**Difference (%)**
A. ramsayi	0.163	0.183	0.020	12.3
V. aspis	0.195	0.211	0.016	8.2
S. miliarius	0.162	0.181	0.019	11.7
B. arietans	0.177	0.194	0.017	9.6
P. guttatus	0.158	0.175	0.017	10.8
S. diadema	0.175	0.200	0.025	14.3
N. atra	0.187	0.227	0.040	21.4
NOA replica of *N. atra*	0.402	0.435	0.033	8.2
Flat NOA reference	0.401	0.400	-0.001	0.25

The ventral scales of all the investigated snake species as well as the polymeric replica of *N. atra* ventral scale display friction anisotropy shown as larger friction coefficients in backward than in forward direction. For most snake species, a difference of around 10% was observed between the friction coefficients in these two inverse directions, while on *S. diadema* and *N. atra* the value reaches even about 15% and 20%, respectively. Interestingly, although the friction coefficient difference (8.2%) is not as large as its original biological scales, similar anisotropic friction between forward and backward direction was also observed on the polymeric replica of *N. atra* ventral scale. Measurements on the flat polymeric reference of the same material indicate an almost isotropic friction (the difference is only 0.25%) in both directions. This outcome suggests that the micro-fibril structures on the surface of ventral snake scales are of great significance for creating friction anisotropy.

More specifically, if comparing the friction coefficients between the polymeric replica and its flat reference, one can see that the values for forward movement on both surfaces are nearly the same, while for backward motion the value on the replica is larger than that on the reference. This outcome reveals that the function of the micro-fibril structures on the ventral snake scales is mainly to increase friction in the direction of snake backward motion, but it cannot reduce friction in snakes' forward motion. This, as a result, leads to friction anisotropy. Nonetheless, one can also observe that the frictional performance of the polymeric replica is not as excellent as its biological snake scales. On the one hand, the obtained friction coefficients on the polymeric replica are considerably larger than that on the original snake scales. Several reasons can be assumed for this, *e.g.*, the elastic modulus of keratin is higher than that of the polymer ($E_{\text{keratin}} = 4.5\ \text{GPa} > 0.9\ \text{GPa} = E_{\text{NOA88}}$) [160] or special material properties of snake scales that might function as a low friction interface. On the other hand, the characterized friction anisotropy on the polymeric replica is smaller than that on the original snake scales. This might be partly caused by the non-perfect replication of the microstructures (*e.g.* the nano-step height at fibril tips on the replica is smaller than that on snake scales). Therefore, although friction anisotropy can be successfully replicated from ventral snake scales to a polymer surface, the snake scales still possess the advantages of exhibiting low friction coefficient with high friction anisotropy if compared to the artificial polymeric surfaces replicated from snakes.

5.3 Friction anisotropy characterization of the nano-step structures by AFM

The existence of the friction anisotropy on ventral snake scales has been validated. The reason for this anisotropic ability has also been verified to be owing to the micro-fibril structures but not the material properties of the scales. However, to determine the mechanisms of how micro-fibril structures inducing friction anisotropy, an even smaller “nano-tribometer”, which is able to analyze the frictional performances of single fibril step on the nanoscale, is needed. A sharp AFM tip meets this requirement through scanning along the micro-fibrils in two inverse directions to correlate the friction anisotropy to the micro-fibril structures. Similarly, the same characterization procedure can be also applied to the step structures of dorsal sandfish scales and a polymeric replica of *N. atra* scales. This is aiming to analyse the friction properties of different types of nanoscale steps as well as their performance on a different material.

5.3.1 Micro-fibril structures of snakes

The friction anisotropy of single fibril steps was examined on the ventral scales of three snake species (*N. atra*, *S. diadema*, and *P. guttatus*). A series of topographical and frictional analysis was carried out and recorded simultaneously by AFM. In order to better simulate the frictional performance of single micro-fibrils (especially at the fibril step) during snake’s locomotion, the sample orientation was intentionally adjusted allowing the AFM sharp tip to scan exactly along the longitudinal axis of the micro-fibril. This will force the tip to unavoidably, vertically move up and down the nano-steps when scanning across the micro-fibril tips. An area of 10 µm × 10 µm was scanned on each sample and in each scan both topographical and frictional signals including trace and retrace data were recorded, respectively.

Figure 5.3 shows the characterization results on the ventral scales of snake *N. atra*. Typical oriented micro-fibril structures were observed from the topography image (top panel of Figure 5.3 a). The red arrow in the image represents the position where a topographical line section longitudinally across the micro-fibrils was extracted. The corresponding topographical line section was plotted in the middle panel. Three apparent, noticeable nanoscale steps can be observed at the fibril tips. The step height regarding as the distance from the fibril top to the bottom base surface was measured as in the range of 50 nm - 60 nm at the three investigated fibril tips.

During the scanning of the AFM tip along the topographical line (position marked by the red arrow), the frictional forces were also recorded simultaneously. The signals of moving in forward (trace) and backward (retrace) directions were collected through a friction loop. The bottom panel in Figure 5.3 a) shows such a friction loop for a normal load of 1184 nN. At the nano-step of fibril tips, a significant frictional peak was observed for the AFM tip scanning in both trace and retrace directions. On the fibril terrace (non-step area), however, the measured friction remains more or less constant. Moreover, it is also interesting to note that the frictional peak in trace direction (AFM tip going upward the step) is larger than that in retrace direction (downward the step). Such a difference indicates comparable friction anisotropy at the nano-steps of fibril tips. To quantitatively analyse this anisotropic friction between upward and downward step direction, frictional increase was defined as the difference between the maximum frictional force at a step edge and the friction on the corresponding terrace [72]. The averaged friction between trace and retrace terraces was calculated as the half of mean difference of the friction values between the two terraces. These defined frictional parameters are all indicated by the black arrows in the bottom panels of Figure 5.3 a).

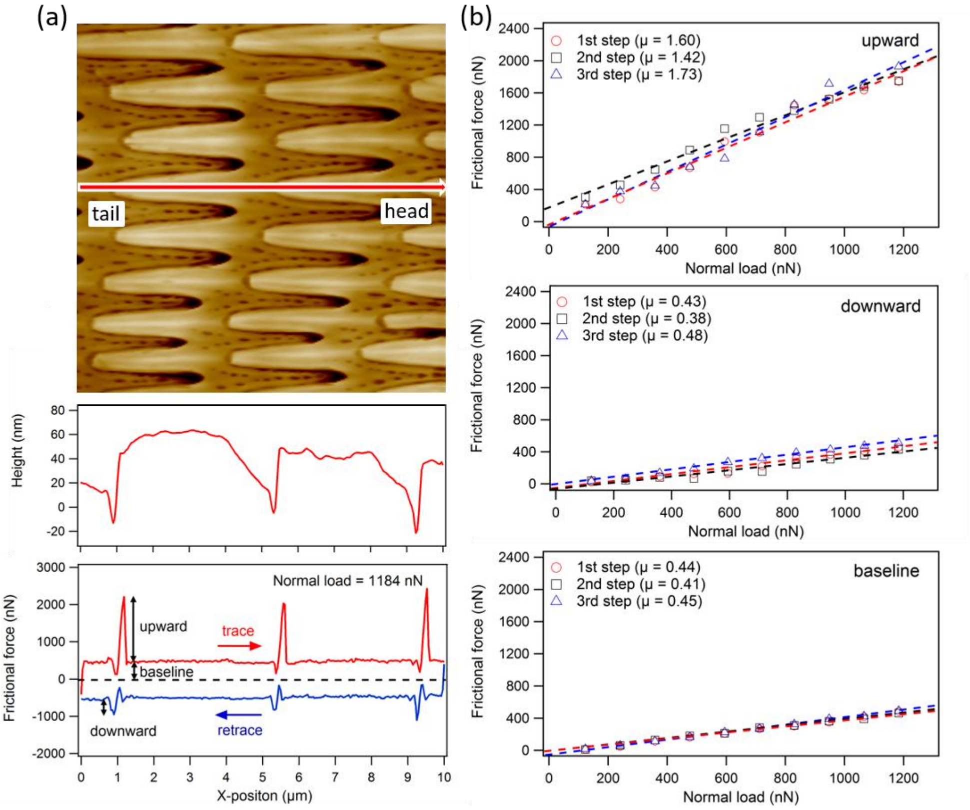

Figure 5.3: Topographical and frictional analysis on the micro-fibril structures. Ventral scales of a Chinese cobra (*N. atra*) were characterized with a sharp AFM tip, which indicates significant friction anisotropy at the step structure of the fibril tips. (a) The top graph shows an AFM topography image (size: 10 μm × 10 μm) of a *N. atra* ventral scale revealing the oriented micro-fibril structures. The snake body proceeds along the red arrow and the head is located towards the right, which means that the micro-fibrils point towards the tail. A longitudinal line section across the fibril structures along the red arrow in the topography image is shown in the middle panel. Three nano-steps were observed at the fibril tips and the step height ranges from 50 nm to 60 nm. The bottom panel represents the corresponding friction loop for the AFM tip scanning along the red arrow under a normal load of 1184 nN. The trace scanning (from left to right, marked in red) represents the AFM tip going upward the steps, while the retrace scanning (from right to left, displayed in blue) shows the downward stepping. Frictional peaks arose at the step edge whenever the tip scans upward or downward the fibril tips. The frictional increase (indicated by the black arrows) for stepping up is much larger than that for stepping down. (b) The calculated frictional increase at the corresponding three fibril steps is plotted as a function of the applied normal load. For the AFM tip stepping upward and downward as well as scanning on the terraces (baseline), the frictional increase displays a linear increase with the normal load, while the corresponding frictional coefficient differs for the three cases (specific values are illustrated in the legend).

Figure 5.3 b) shows the frictional increase for the AFM tip scanning upward and downward the nano-steps (corresponding to “upward” and “downward” in Figure 5.3 a) as well as the friction on the terrace (“base-line”) plotted as a function of the applied normal load. All data points manifest a nearly linear relationship with normal load. The friction coefficients for these three cases can be calculated as the slope of a linear fit. The results are shown in the legends. Apparently, the resulting frictional coefficient for the AFM tip scanning upward the step is much larger than that for scanning downwards. More specifically, at the micro-fibril tips of *N. atra* ventral scale, the averaged frictional coefficient for upward a step is nearly 3.7 times higher as that for stepping down. The friction anisotropy is defined as the frictional coefficient for scanning upward a step divided by that for downward scans. Thus, the friction anisotropy at the nano-steps of the ventral scales of the investigated Chinese cobra is 3.7. Since the micro-fibril structures always point towards the snake’s tail, the frictional coefficient for the AFM tip scanning downward the steps of the fibril tips corresponds to that in the direction of a snake moving forward. Hence, this outcome indicates that for

Chinese cobra moving forward is considerably easier than moving backward. Furthermore, if compared to the results characterized by micro-tribometry in Chapter 5.2.2 (*i.e.* the friction coefficient in forward motion is 21.4% less than that in backward motion), the friction anisotropy characterized at single fibril steps by AFM is more significant.

In addition, in order to further validate the above results, two more snake species (*S. diadema* and *P. guttatus*) were characterized by the same analysis procedure. The results are shown in Figure 5.4 and Figure 5.5, respectively. Very similar micro-fibril structures with nano-steps at their tips as well as the frictional performance when the AFM tip scans over these step structures were observed. However, interestingly, the step height at the fibril tips differs significantly among the investigated snake species. The step height on these two species is smaller than that on *N. atra*, with the value of 15 nm - 30 nm and 10 nm - 20 nm for *S. diadema* and *P. guttatus*, respectively. This difference can be caused by several reasons, *e.g.*, their different ages, sizes, living habitats, or the endured abrasion on the step structures. Although displaying diverse step heights, these snakes show very similar frictional performances at the fibril steps, indicating a general mechanism of generating friction anisotropy by the micro-fibril structures on their ventral scales (see Figure 5.4 b and Figure 5.5 b).

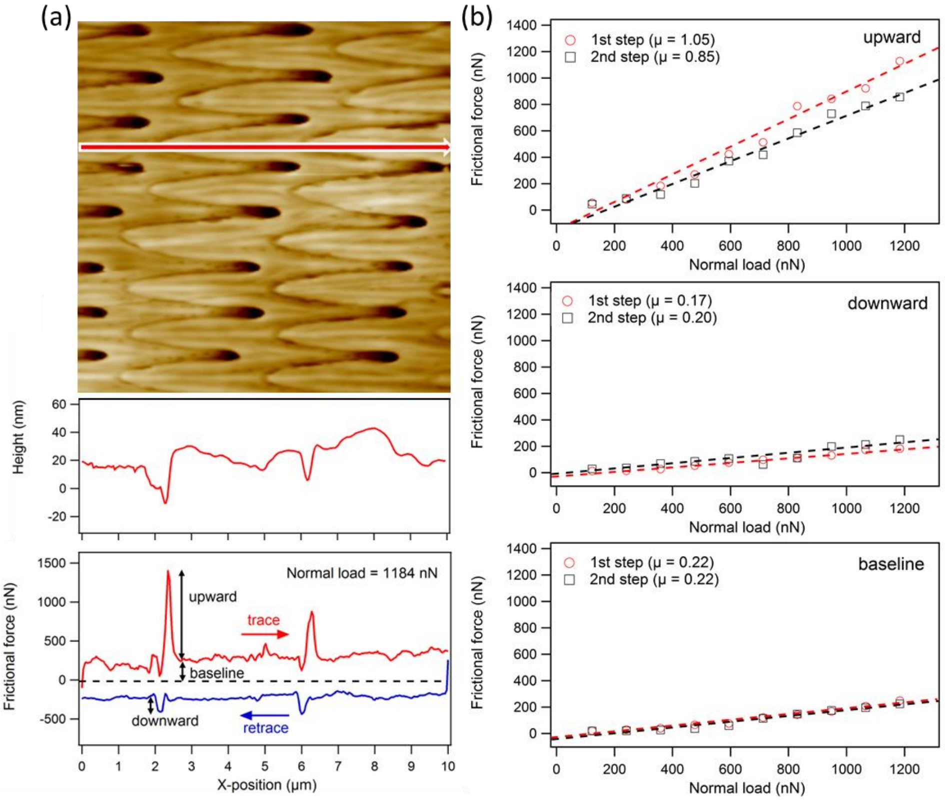

Figure 5.4: The same topographical and frictional analysis as in Figure 5.3 conducted on *S. diadema*. Similar micro-fibril structures as on *N. atra* were observed, while the step height on this snake is smaller (ranging from 15 nm to 30 nm). The frictional performances at the fibril steps were also very similar to that on *N. atra*. The calculated friction coefficients (illustrated in the legends) were smaller than those of *N. atra*.

Similarly, analysing the friction loop across the micro-fibril structures and calculating the friction coefficients at the fibril steps, the friction anisotropy for the AFM tip scanning upward and downward the investigated nano-steps of *S. diadema* and *P. guttatus* are 5.2 and 3.8, respectively. Hence, in the light of the duplicated frictional response observed on these three snake species, it can be confirmed that the step structures at the fibril tips function as a unidirectional stopper to create friction anisotropy. Such design will help snakes to increase traction or avoid slippery when necessary.

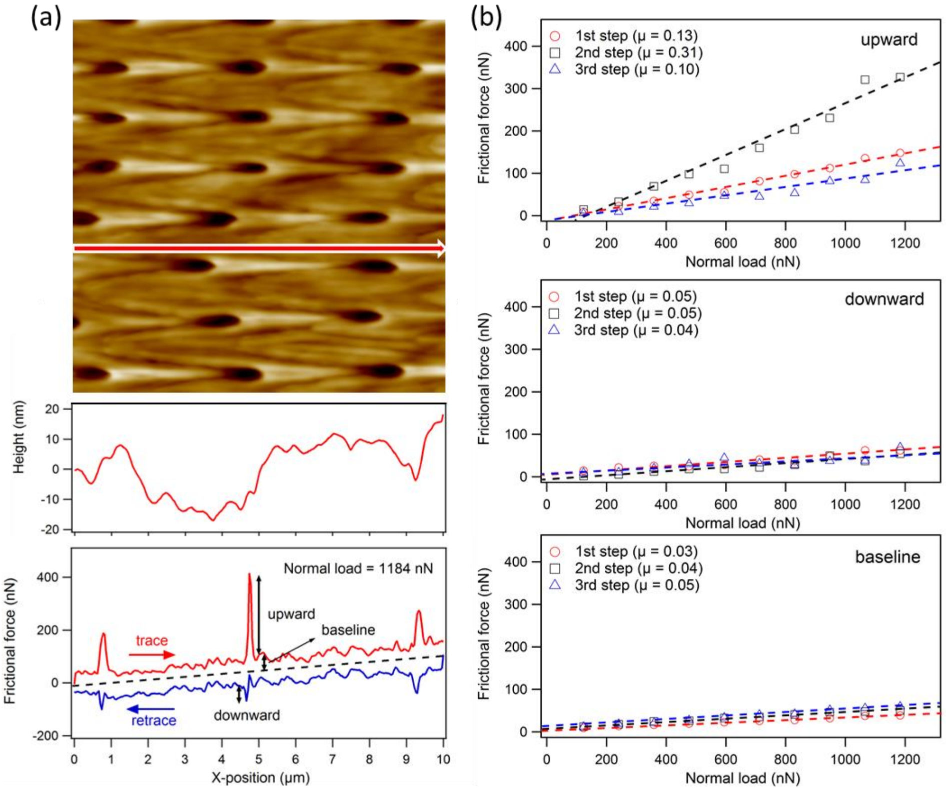

Figure 5.5: The same topographical and frictional analysis as in Figure 5.3 conducted on *P. guttatus*. Smaller step heights (10 nm - 20 nm) and frictional coefficients (illustrated in the legends) as for *N. atra* and *S. diadema* were obtained.

Lastly, further comparing the friction coefficients measured on the three species, one can notice that a larger step height induces a larger friction coefficient. The step height decreases on the species in the order of *N. atra*, *S. diadema*, and *P. guttatus*. The friction coefficient also manifests the same trend for all the three cases of “upward”, “downward”, and “baseline” scanning. This might help to explain the elaborate mechanism of the snakes using their nanoscale step structures to manipulate friction or to achieve the friction anisotropy they desire. A detailed analysis of this friction-controlling mechanism will be given in the following Chapter 5.4. Besides this, it is also very interesting to note that for all the investigated snakes the frictional coefficients for downward the step are very close to that of scanning on the fibril terrace (“baseline”), which are both much smaller than that for upward the step. Particularly, considering that there are no step structures on the fibril terrace, the friction on this area should be mainly caused by the material properties of the snake scales. On this account, the friction in moving downward the step direction also depends on the material properties of the snake scales. No extra, significant friction will be produced when snakes slide towards this direction. Therefore, the oriented micro-fibril structures on the ventral scales of snakes provide unidirectional step structures to increase friction when their potential locomoting direction is upward the fibril steps (corresponding to the backward motion of snakes). They cannot help to reduce friction when the potential locomoting direction is opposite (corresponding to the forward motion of snakes). Such structural arrangement, as a result, leads to a friction anisotropy along the longitudinal snake body. This outcome also coincides with the results obtained by the micro-tribometry in Chapter 5.2.2.

5.3.2 Step structures of sandfish

In difference to the oriented micro-fibril structures on ventral snake scales, the dorsal scales of sandfish exhibit continuous step structures. Nonetheless, both types of microstructures display step edges on the nanoscale. Thus, the nano-step induced friction anisotropy on snakes may also apply to the sandfish. Based on this, the same topographical and frictional analysis was conducted on dorsal sandfish scales. The results are summarized in Figure 5.6. From the topography image and the line cross section graph one can see that sandfish shows even more noticeable step structures than the investigated snakes, *i.e.*, the step height on sandfish is much larger (200 nm - 300 nm). This indicates probably more fascinating frictional performances (*e.g.* larger friction anisotropy) than ventral snake scales.

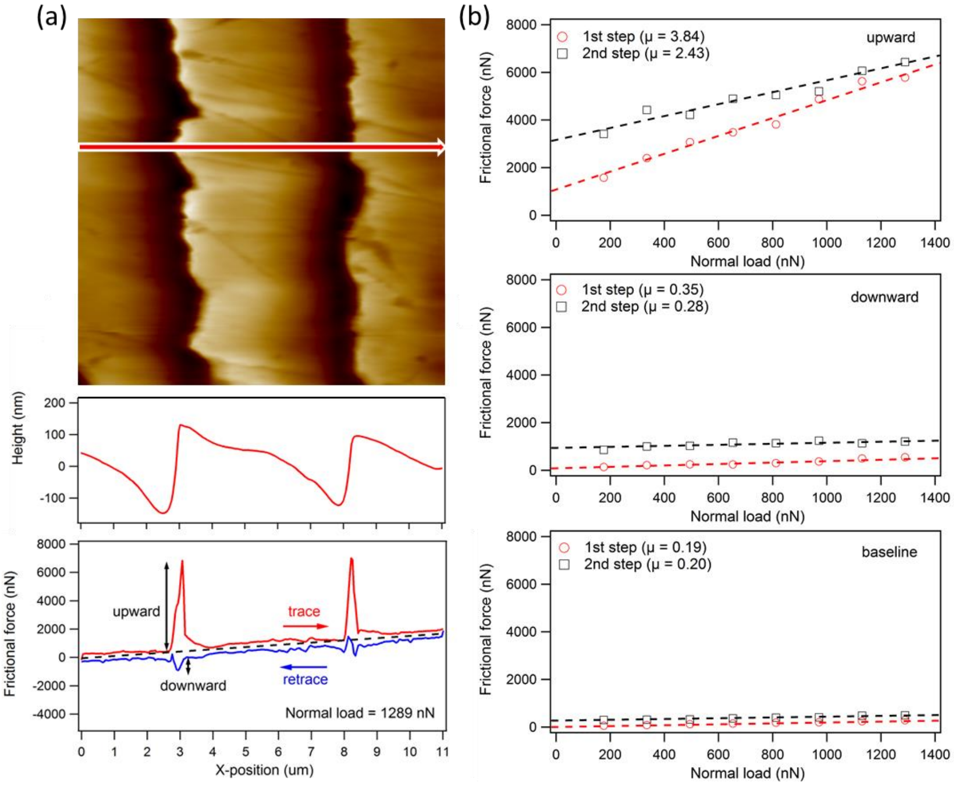

Figure 5.6: Topographical and frictional analysis on dorsal sandfish scales conducted by AFM. The same procedure as already described in Figure 5.3 was applied. The characterized step heights are in the range of 200 nm - 300 nm which are much higher than that on the investigated snakes. The frictional coefficients (illustrated in the legend) for upward the step are also larger, while for downward the step and scanning on the fibril terrace they are comparable with snakes.

Similar to snakes, the frictional effects of the AFM tip scanning vertically across the step edges on dorsal sandfish scales also indicate friction anisotropy. This suggests that they might feature the same mechanism of generating friction anisotropy at the nanoscale. More specifically, the averaged friction coefficient for the AFM tip scanning upward the nano-steps on sandfish (around 3.1) is much larger than that on Chinese cobra (around 1.6). For downward scans, however, the results of sandfish (0.32) is surprisingly smaller than that of Chinese cobra (0.43). More significant friction anisotropy was observed on dorsal sandfish scales (9.8) than on the ventral scales of Chinese cobra (3.7). In addition, dissimilar to the outcome on snakes, for dorsal sandfish scales the friction coefficients on the terrace (“baseline”) are the smallest among the three cases (“upward”, “downward”, and “baseline” scanning), especially smaller than that of downward the steps. This is probably caused by the comparably large step height on dorsal sandfish scales, *i.e.*, the AFM tip scans downward a step of several hundreds of nanometers might produce an additional friction leading to a larger friction coefficient than for scanning on the terrace. Nonetheless, the direction of the step structures on dorsal sandfish scales is not known, because sandfish molts their scales into individual pieces and only a small part of them was obtained for the characterization in this thesis. Overall, it can be concluded that the orientated nanoscale steps on the scales of snakes and sandfish provide anisotropic friction in their locomotion directions. This effect is more noticeable at the nanoscale (characterized by AFM) than at the microscale (characterized by micro-tribometry).

5.3.3 The polymeric replica of snake scales

Although friction anisotropy was found on the micro-fibril structures or step structures of snakes and sandfish, there exists another possibility that this anisotropic frictional behavior might be caused by the material properties of the reptile's integument. One of the best methods to analyze the relationship between the friction anisotropy and step structures is to fabricate these step structures onto a non-biological surface and characterize the friction anisotropy on this surface. Therefore, the above presented topographical and frictional analysis was also repeated on a polymeric replica of *N. atra* ventral scale, which was fabricated beforehand in Chapter 5.2.1, to further validate the nano-steps induced friction anisotropy on snake scales. The results are displayed in Figure 5.7.

As in the previous experiments on snakes and sandfish, the topography image, line cross section, and the frictional response of AFM tip scanning upward and downward the fibril steps were analysed. In the topography image, it can be seen that the micro-fibril structures were well replicated from its original biological sample to the polymer surface. There is also some structural information lost during the replication process (see the black pits at the fibril base part in Figure 5.7 a). The step heights at the fibril tips revealing in the topographical line section graph (scanning position is indicated by the red arrow in the AFM image) range from 30 nm to 45 nm. These values are slightly smaller than that on their original biological sample of *N. atra* scale (50 nm - 60 nm). However, the shape of the friction loop for the AFM tip longitudinally scanning across the micro-fibrils on the polymeric replica is very similar to that on *N. atra* scale (see Figure 5.3). Significant frictional peaks are recorded when the AFM tip scans upward or downward the steps and relatively constant frictional signal on the fibril terrace (non-step area) is observed. In such a friction loop, the predefined frictional increase (see Chapter 5.3.1) for upward and downward the steps as well as the friction on the terrace can be calculated.

Increasing the applied normal load on the surface and recording the friction signal, friction vs. load curves were plotted for the cases of the AFM tip scanning upward, downward the step, and scanning on the fibril terrace. Their corresponding friction coefficient was calculated by conducting a linear fit. Figure 5.7 b) shows the results of it scanning along the red arrow in Figure 5.7 a) across three different nano-steps. If compared to the results obtained on *N. atra* scale in Figure 5.3, the friction coefficients for scanning upward the steps on this polymeric replica are a little bit smaller. The averaged value for the replica and *N. atra* is 1.21 and 1.58, respectively. This might be caused by the smaller step heights on the replica surface compared to that on the original snake scales. However, interestingly, the averaged frictional coefficient for downward the step on the replica (0.49) is slightly larger than that on snake scale (0.43). As already discussed in Chapter 5.3.1, the frictional coefficient in this direction is close to that on the fibril terrace, which is mainly determined by the material properties of the sample. Thus, the difference of the friction coefficient for downward the step direction between the polymeric replica and *N. atra* scale is probably caused by the material discrepancy of NOA 88 and snake scales, such as elastic modulus (see the discussion in Chapter 5.2.2). As a result, the friction anisotropy on the replica surface is calculated as 2.5, which is also not superior than *N. atra* scale (3.7). Lastly, although displaying different values, the overall outcome (*i.e.* friction coefficients and friction anisotropy, on both *N. atra* scale and polymeric replica) characterized by AFM also coincides with the results from micro-tribometry in Chapter 5.2.2. The friction anisotropy on the step structures, however, is more apparent on the nanoscale by the analysis of AFM than that of micro-tribometry.

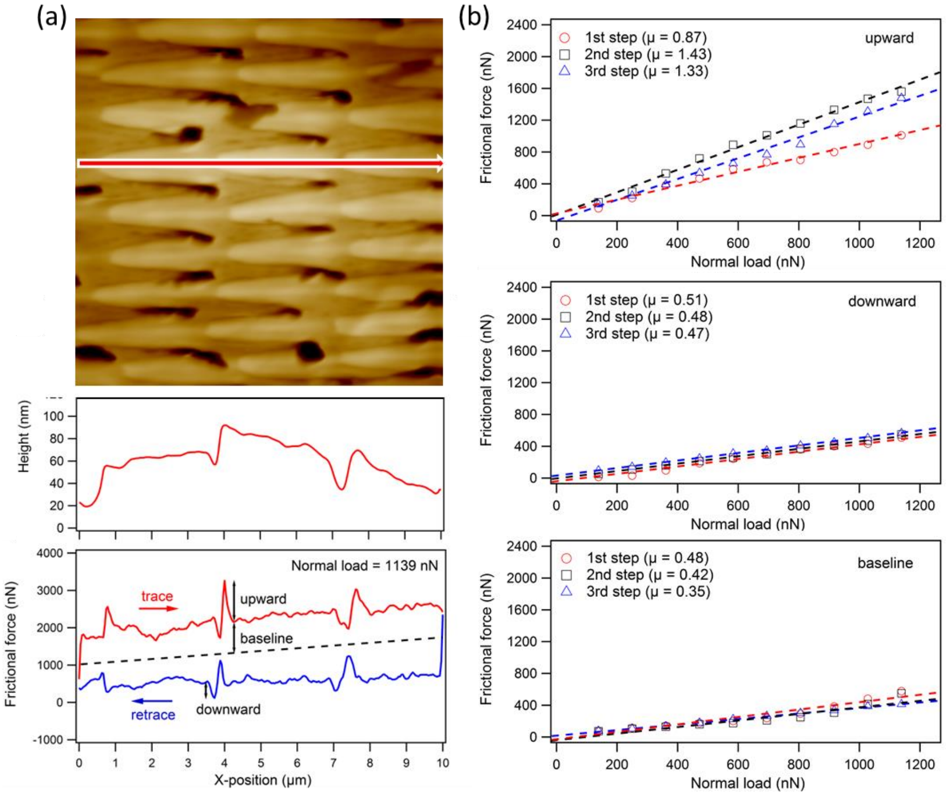

Figure 5.7: The same measurement and analysis as in Figure 5.3 conducted on the polymeric replica. The fibril step height on the replica (30 nm - 45 nm) is slightly smaller than that on its original biological template (50 nm - 60 nm). The frictional coefficient for upward the step is smaller while for downward the step it is larger. This leads to a smaller frictional anisotropy on the replica than on the original snake scale.

5.4 Friction anisotropy performance along snake bodies

From the analysis above, it can be confirmed that the oriented micro-fibril structures on the ventral scales of snakes featuring nano-steps at the fibril tips help to create anisotropic friction in their locomotion directions. Snakes moving forward is comparably easier than moving backward. This structure induced friction anisotropy might allow snakes to achieve various beneficial performances when necessary. Moreover, from the results of AFM characterization, the height of fibril step also plays an important role for regulating friction anisotropy. In this case, it is of great necessity to examine the step height as well as the friction anisotropy from an overview of the whole snake body for better understanding their frictional performances during locomotion.

5.4.1 Step height dependent friction anisotropy

First, as discussed in Chapter 5.3.1, on the three investigated snake species a larger step height induces a larger friction coefficient for the AFM tip scanning upward the steps, while the friction coefficient for downward the steps is always close to that on the terrace. The relationship between step height and friction coefficients as well as friction anisotropy should provide the detailed mechanism of snakes controlling friction. Hence, frictional coefficients together with the calculated friction anisotropy were characterized at several nano-steps on the ventral scales of *N. atra*, *S. diadema*, and *P. guttatus*. The results were plotted as a function of their corresponding step heights and summarized in Figure 5.8.

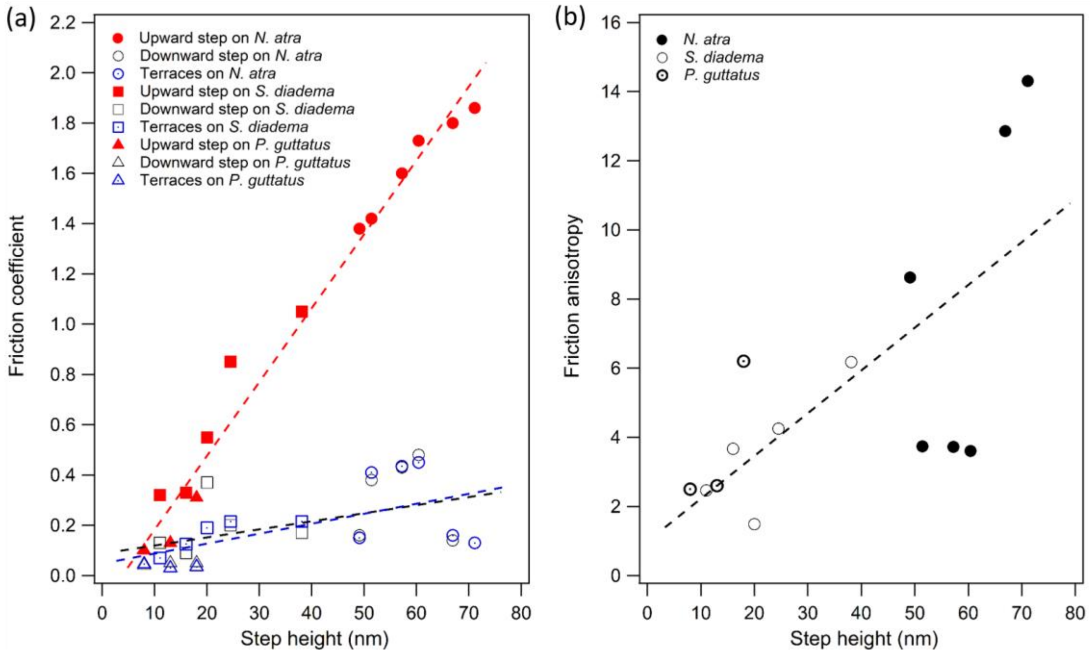

Figure 5.8: Friction coefficients and friction anisotropy plotted as a function of the fibril step height. The friction coefficients at step edges and on terraces as well as the calculated friction anisotropy on the ventral scales of *N. atra*, *S. diadema*, and *P. guttatus* are plotted. (a) Friction coefficients for upward steps display a linear increasing relationship with step height, while for downward steps and on the terraces the increase is quite low. (b) Friction anisotropy shows a similar trend as the upward friction coefficient.

For increasing step heights, the friction coefficients for upward steps grow linearly, while those for downward steps and on the terraces show a nearly negligible increase. The upward frictional coefficients grow much faster than the downward ones. As a result, the calculated frictional anisotropy shows a similar trend as the upward frictional coefficients, displaying a significant increase with the step height. On different snake species, friction anisotropy can be observed in the range of 1.5 - 14.3 according to the step heights ranging from 11 nm to 57.2 nm. A step height of several tens of nano-meters can even produce more than 10-times of the nanoscale anisotropic friction in the opposite directions. This effect is independent of snake species indicating a universal mechanism. Furthermore, some more smart abilities can be imagined, for example, snakes might equip micro-fibril structures with flexible fibril tips which can adjust the step height whenever necessary. With unchangeable tips but different step heights on different segments of their ventral scales achieving desired friction anisotropy along snake's body might be also possible. Before examining the distribution of the step height, the flexibility of the micro-fibrils was first checked. A detailed analysis of the distribution of the step height and friction anisotropy along the snake's body will be discussed in the following Chapter 5.4.3.

5.4.2 Checking the flexibility of the micro-fibrils

Snakes might possess the ability of dynamically controlling the step heights, *i.e.*, the micro-fibrils might be flexible at their tips leading to adjustable step heights to achieve desirable friction anisotropy when necessary. Recent studies [31, 171] reported that snakes can move their scales to enhance friction and prevent slipping. Similarly, on the microscale, snakes might be able to move the micro-fibril tips to realize variable step heights for designated friction anisotropy during locomotion.

As a first test, we tried to violently stretch or cut the scales, which caused the displacement of the micro-fibrils from their original position. The scale surface was then imaged by SEM. Figure 5.9 shows the topography of *N. atra* ventral scale after a series of these operations. It can be clearly seen that some micro-fibrils were separated from the scale surface (Figure 5.9 a) after being stretched along the fibril longitudinal direction. Figure 5.9 b) and c) show the free micro-fibrils hanging over the scale edge after cutting the scales across the fibril structures with a sharp blade. All these evidences indicate that the micro-fibrils on the scale surface might be movable or flexible. However, it has to be considered that the violent methods used above are not commonly happened in a snake’s daily life. It is also possible that the micro-fibrils are loosely attached on the scale surface and were separated by the produced huge forces during these violent operations. Practically, snakes rarely withstand such huge forces during locomotion. Thus, another experimental procedure by SEM was applied.

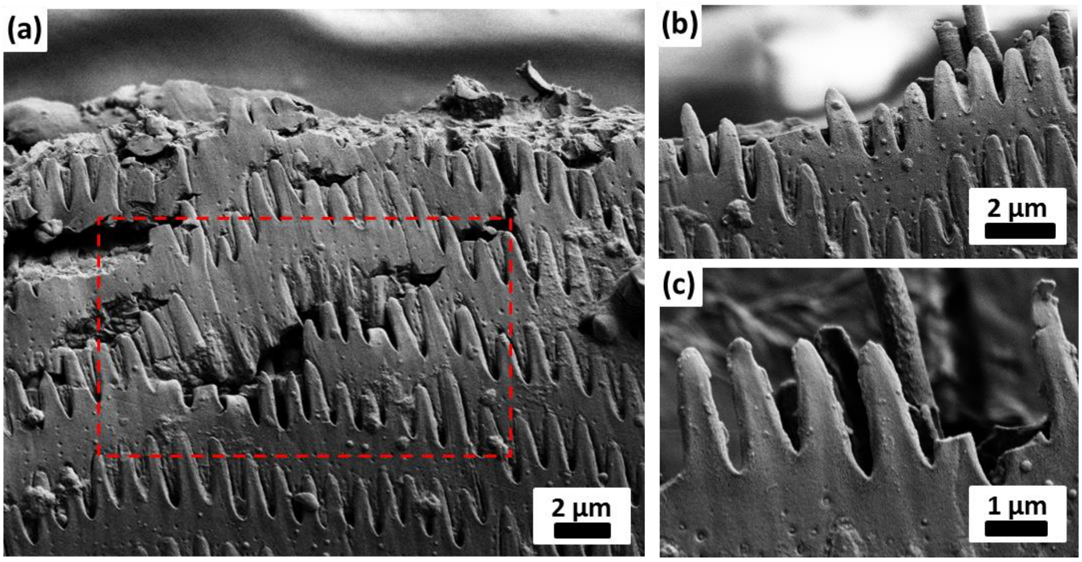

Figure 5.9: SEM images of the stretched or cutted *N. atra* ventral scales. The results indicate that the micro-fibrils might be movable and not rigidly fixed. (a) Stretching the surface along the longitudinal direction of the fibrils leads to the separation of some micro-fibrils from the surface. (b) Cutting the scale surface across the micro-fibril structures causes several micro-fibril tips hanging over the cutting edge. (c) Several micro-fibrils are completely freed from the substrate surface.

To further check the possible flexibility of the micro-fibrils, an examination with a micro-needle scratching on the scale surface or bending the surface from one side was conducted on *N. atra* ventral scales. The whole operating process was conducted under SEM observation. To avoid the influence of the sputtering metal on the manipulation results, no coating was sputtered on the scale surface. A low acceleration voltage together with a low working distance between the SEM detector and the sample surface was used to enable the SEM investigation. Figure 5.10 shows the time-lapse of a micro-needle manipulating the micro-fibril structures on the scale surface.

Using the micro-needle scratching against the micro-fibrils on the scale surface (Figure 5.10 a), the fibrils were found to remain at their original position and the fibril tips were not movable. Further placing the micro-needle beneath the scale bottom surface and subsequently lifting the scale caused the surface bending (Figure 5.10 b). In this case, the micro-fibril structures on the surface should endure a considerably large bending force. If the micro-fibrils were flexible, the movement of the fibril tips would be observed during this bending process. However, from Figure 5.10 b) no evidence shows that the fibril tips are flexible.

Therefore, it can be concluded that, at least on the molted snake scales, the micro-fibrils are not movable but fixed, and the step heights at the fibril tips are not adjustable.

Despite this, it has to be mentioned that all the investigations above were conducted on the molted scales of snakes. Although no extra treatment was applied, the scales were used for examination at least several months after being molted from the corresponding snakes. Thus, the loss of water or other fluids with time may reduce the flexibility of the micro-fibrils on such molted scales. However, the same measurements on a living animal are not applicable due to the requirement of a vacuum condition for SEM investigation, which is not suitable for a living snake. Further examinations of the flexibility of the micro-fibrils on a "fresh" snake integument are highly recommended.

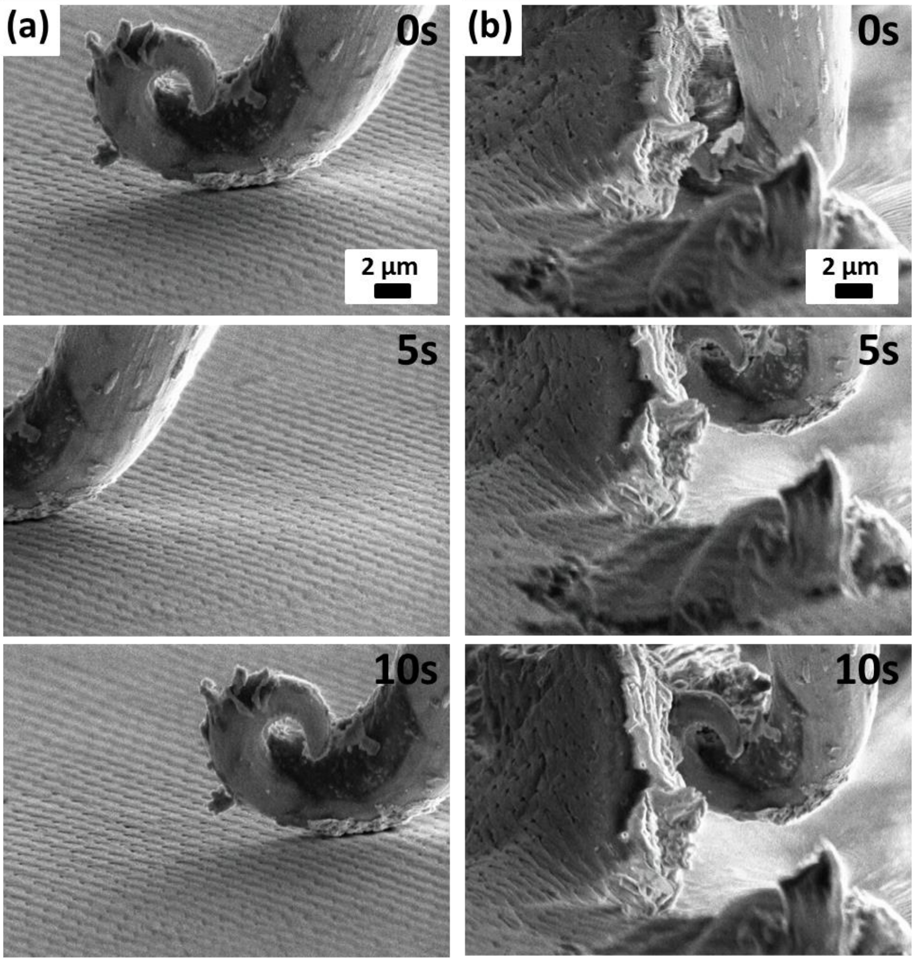

Figure 5.10: Time-lapse of the micro-needle manipulation experiments. Ventral scales of *N. atra* were checked. The whole manipulating process was observed with a SEM. No sputtering was conducted on the sample surface. (a) Micro-manipulator scratches against the micro-fibrils on the sample surface. No visible change or movement was found on the fibril structures. (b) Using the same manipulator lifting and pushing the scale from its side makes the surface bend. Similarly, no flexible micro-fibrils were observed. For both cases, 10 s of manipulation were shown.

5.4.3 Distribution of step height and friction performance along snake bodies

Since no evidence was found for the assumption that the micro-fibrils are movable under the control of snakes, another possible feature, which snakes might have, is suspected. They might carefully organize various magnitudes of step height along their body to achieve diverse friction anisotropy in different segments. To check this, an investigation of the distribution of the step heights along a snake's body was conducted to describe the frictional performance on different sections of the ventral snake scales. The results are summarized in Figure 5.11. The step heights are indicated by the red bars and their specific values are evaluated at the left axis.

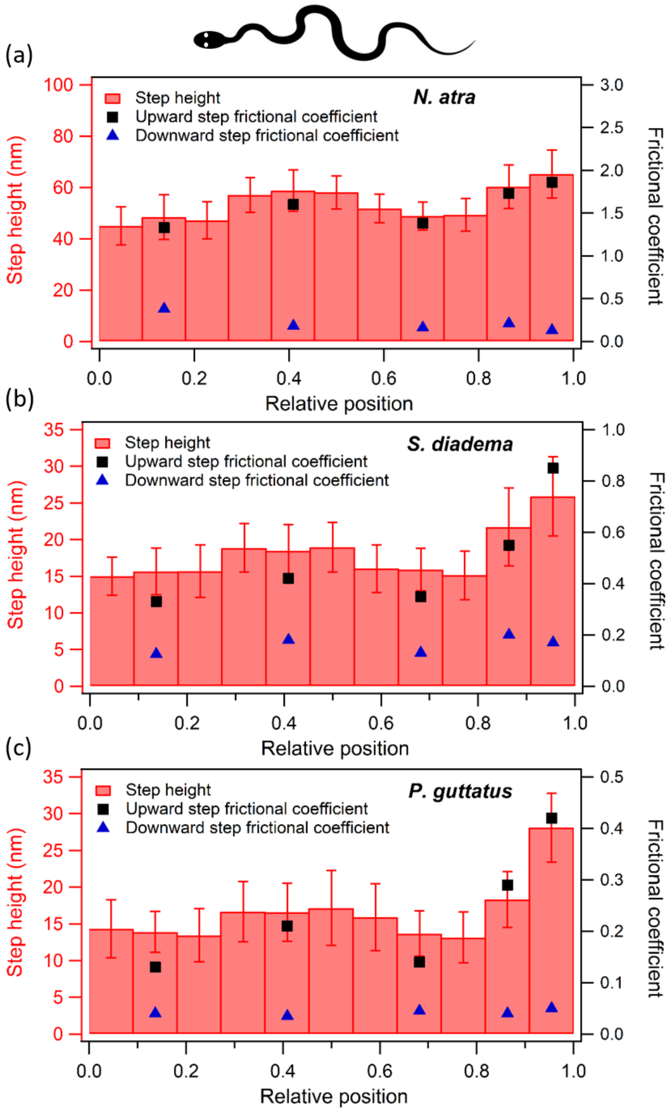

Figure 5.11: Distribution of the step height and friction coefficient along three snake's bodies. The averaged step heights (red bars) as well as their corresponding frictional coefficients for scanning upward the steps (black square markers) and downward the steps (blue triangle markers) on the ventral scales along the body of snake (a) *N. atra*, (b) *S. diadema*, and (c) *P. guttatus* are presented. The snout and tail end of the snakes are represented by the "0" and "1" position in the graph, respectively. 11 segments were evenly divided on each snake body and 50 different step heights were measured in each section. The step height values in each section were averaged and plotted. Their statistical errors were also calculated. Comparably large step heights and upward friction coefficients were observed on the middle section of all the investigated snakes. It is also interesting to note that at the far end of the snake tail locates extremely large step heights which were shown as high ridges at the fibril tips on the nanoscale.

Three snake species including *N. atra*, *S. diadema*, and *P. guttatus* were examined. On each snake 11 segments from the snout to the tail end were evenly selected for characterization. 50 different step heights in each divided section were measured and averaged to the values presented in Figure 5.11. The error bars represent the statistical errors. It is interesting to note that the step height distributes very similarly along the body of the three investigated species. The step heights on the middle section of each snake are considerably larger than those on the other areas except the tail end where exhibits the largest values. Furthermore, the averaged step heights in the anterior area (the first three sections) and the posterior area (except the far end of the tail) are very approximated. This outcome indicates that snakes (at least the investigated species) exploit a universal but well-designed distribution of step heights along their body for the control of friction anisotropy during locomotion.

In addition, the distribution of the frictional coefficients for scanning upward the fibril step (corresponding to snake backward motion) along the body of the three snake species was also analysed. The results are shown by the solid square markers (values indicated by the right axis) in Figure 5.11. Coinciding with the results in Chapter 5.4.1, the distribution of this type of frictional coefficients manifests a similar trend as their corresponding step heights. The comparably large step heights on the middle section of snake bodies cause relatively large friction coefficients in the direction of snake backward motion. The largest frictional value locates at the far end of the tail. The results in the other areas are all smaller. The friction coefficients for downward scans (blue triangle markers in Figure 5.11), however, are considerably lower and nearly independent of the step height. As a result, the friction anisotropy shows a similar distribution pattern as the upward friction coefficients along the snake body.

Consequently, snakes are equipped with relatively large step heights in their middle section to generate high friction anisotropy for the aim of enhancing traction forces during locomotion or to prevent slipping when performing climbing behaviours. One can also note that the extremely large step heights at the tail end induce even more significant friction anisotropy. Nonetheless, the tail of snakes is commonly considered as an anchor during snake's locomotion, which does not involve in the generation of traction or braking forces. A previous study of Jayne *et al*. reported that the most distal portion of the tail neither improves nor inhibits speed of terrestrial lateral undulation of the snake *Thamnophis sirtalis* [172]. Thus, the noticeable friction anisotropy found at snake tail might not have an actual function.

Moreover, the overall averaged step height on the leading half of snake body (anterior half) is smaller than that on the trailing half (posterior half). This also leads to a frictional difference between these two sections along snake body. Snakes can generate more significant friction anisotropy on their trailing half for traction. This outcome confirms the results from Abdel-Aal *et al*. who measured the distribution of friction coefficients and friction anisotropy on a *Python regius* by a bio-tribometer with a 40 mm diameter probe [52]. Therefore, it can be concluded that the micro-fibril structures with nano-steps on the ventral scales enable snakes to achieve friction anisotropy in locomoting directions. Besides this, an even more genius ability of them is that the step height inhomogeneously distributes along the snake body in a well-designed way to optimize their frictional performances during sliding. Recent studies [31, 32, 67, 68] with euthanized snakes evaluated friction coefficients when the whole snake body slides down a slope. The results also reveal frictional anisotropy in snake forward and backward motions, which coincides with our study. However, this type of measurement cannot show the variation of friction anisotropy in different segments of a snake body. Our results will be of great importance for the simulation of snake's locomotion and also for the development of snake-shaped robots [173-175].

5.5 Artificial polymeric surface with variable friction anisotropy

Finally, another artificial polymeric surface, which can show variable friction anisotropy in its different sections, is fabricated using the soft lithography technique described in Chapter 2.4.2. First, six pieces of scales were picked from the head, middle, and tail section of snake *N. atra* (*i.e.* two pieces in each section, respectively). After that, the collected scales were accordingly stitched and fixed on a silicon wafer by a liquid glue (LOCTITE® 401, Henkel Adhesives). The stitched scales were finally replicated onto a NOA 88 surface via a PDMS mold. Due to the variation of the fibril step height as well as its induced friction anisotropy along the snake's body, the resulting polymeric surface accordingly exhibits micro-fibrils with a different step height and therefore, diverse frictional anisotropy in different sections. Figure 5.12 shows a photo of the polymeric replica and the AFM characterized step height and friction anisotropy in each section. The markers "1" - "6" in the photograph represent the six sections on the replicated surface, which corresponds to the original six pieces of snake scales, respectively. Among them, sections "1" and "2" are replicated from scales near snake head, sections marked by "3" and "4" are from snake middle section, and the last two sections ("5" and "6") are from snake tail. The characterized step height and friction anisotropy in each section are displayed in the last two panels at the bottom. A similar increasing trend is observed for step height and friction anisotropy with the section ranging from "1" to "6" (see the dashed lines in the last two panels). This means that the replicated polymeric surface shows increasing friction anisotropy along the scale stitching direction (from head to tail).

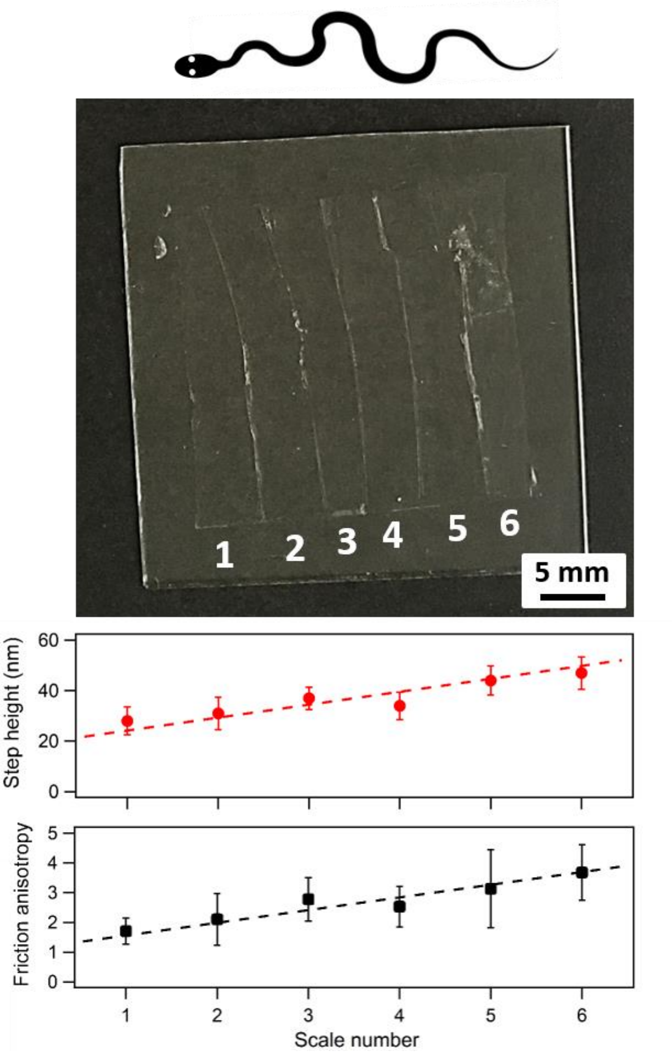

Figure 5.12: An artificial polymeric surface with variable step height and friction anisotropy in different areas. Six pieces of snake scales were stitched and replicated onto a NOA 88 surface. The top panel shows a schematic snake indicating the direction of the scales stitching. The photograph in the second panel shows the resulted polymeric surface on a glass

slide. The numbers "1" - "6" in the photo represent the section replicated from the corresponding snake scale. Sections "1" and "2" are replicated from head scales; "3" and "4" are from the middle section; "5" and "6" are from the snake tail. The step height and friction anisotropy on each section were characterized by AFM and presented in the last two panels at the bottom. Five different positions were measured in each section. The averaged values and their corresponding statistical errors were calculated and plotted. The dashed lines reveal that the step height as well as friction anisotropy on the replica surface increase from section "1" to section "6" (head to tail).

Furthermore, other desired anisotropic frictional performances can be also achieved by applying various types of stitching scheme, *i.e.*, different arrangements of the fibril step height in different surface sections. This will allow researchers to design and fabricate dedicated surfaces which can feature friction anisotropy with intended directions and magnitudes. Besides this, further replications on low friction surfaces such as metals or ceramics will be of high interest. Due to the comparably large "natural" friction coefficient of the polymer (more than 0.4 for NOA 88, see Figure 5.7 b), the friction anisotropy on the current replica surface is not very significant (around 3.6 at maximum, see Figure 5.12) if compared to a real snake scale (nearly 15 at maximum, see Figure 5.8 b). Therefore, a larger friction anisotropy effect can be expected by embedding nano-steps on metal or ceramic surfaces, which will also be more applicable for engineering tasks.

A shortened version of this chapter was published as the article [176] "Variation of the frictional anisotropy on ventral scales of snakes caused by nanoscale steps", by Weibin Wu, Shudong Yu, Paul Schreiber, Antje Dollmann, Christian Lutz, Guillaume Gomard, Christian Greiner and Hendrik Hölscher, Bioinspiration & Biomimetics, 15, 056014 (2020).

6 Snake-inspired, tunable friction anisotropy surfaces based on shape memory polymers

The ventral scales of snakes are decorated with oriented micro-fibril structures, which feature nanoscale steps at the fibril ends, to achieve friction anisotropy. Moreover, the step height at the micro-fibril ends as well as the induced friction anisotropy are variable along the snake's body, displaying a general pattern among different snake species. This interesting characteristic enables snakes to optimize friction and as a result, to travel more efficiently during locomotion. According to the results in Chapter 5, the fundamental principle of snakes controlling anisotropic friction relies on the varying step heights at the micro-fibril ends. A larger step height leads to larger friction anisotropy. Thus, it will be interesting to fabricate an intelligent, micro-fibril structured surface with changeable step height at the fibril end for the aim of realizing tunable friction anisotropy, *e.g.*, replicating the micro-fibril structures onto a shape deformable material will have a great potential in applications which demands unidirectional friction performance.

In this chapter, shape memory polymers (SMPs) are introduced as substrate for such a replication. As already mentioned in Chapter 2.2.2, SMPs are able to change their shape from a temporarily programmed shape to a predefined permanent shape upon certain stimulus. With this fabulous ability, a snake-inspired SMP surface, which can transit reversibly between friction isotropy and anisotropy through the control of the step heights at the fibril ends, was fabricated by replicating the micro-fibril structures from ventral snake scales to SMPs via hot embossing. The shape-changing capability of the step height and of the friction anisotropy was characterized by AFM. Furthermore, the long-term stability (working time) and reusability (programming cycles) of the surface were also analyzed. Finally, an application of using the snake-inspired, tunable friction anisotropy SMP surface as a self-cleaning platform for unidirectional transport of granular particles is presented.

6.1 Snake-inspired SMP surfaces with switchable topography

The design concept of the snake-inspired, tunable friction anisotropy SMP surfaces is to exploit the shape-changing capability of the SMP to control the step height of the micro-fibril ends and consequently to control the friction anisotropy on the surface. The micro-fibril structures of ventral snake scales were replicated onto the SMP surface as a permanent shape and then the surface was flattened into a temporary shape leading to a surface with no apparent micro-fibril structures. Both processes were conducted via hot embossing but with different embossing plates, temperatures, and pressures. To replicate the micro-fibril structures onto SMP surface, a mold insert (Nickel shim) with the negative of the desired pattern was fabricated beforehand by electro-plating (see Chapter 2.4.3). To flatten the structures, a flat embossing plate was used. For the SMP surface in its temporarily flattened shape, once upon heating, the micro-fibril structures will gradually recover onto the surface exhibiting tunable step height as well as tunable friction anisotropy. Figure 6.1 illustrates the procedure of fabricating the Nickel shim, replicating the micro-fibril structures onto a SMP surface, programming the structured surface into a temporarily flattened shape, and the recovery of the micro-fibril structures on the surface, respectively.

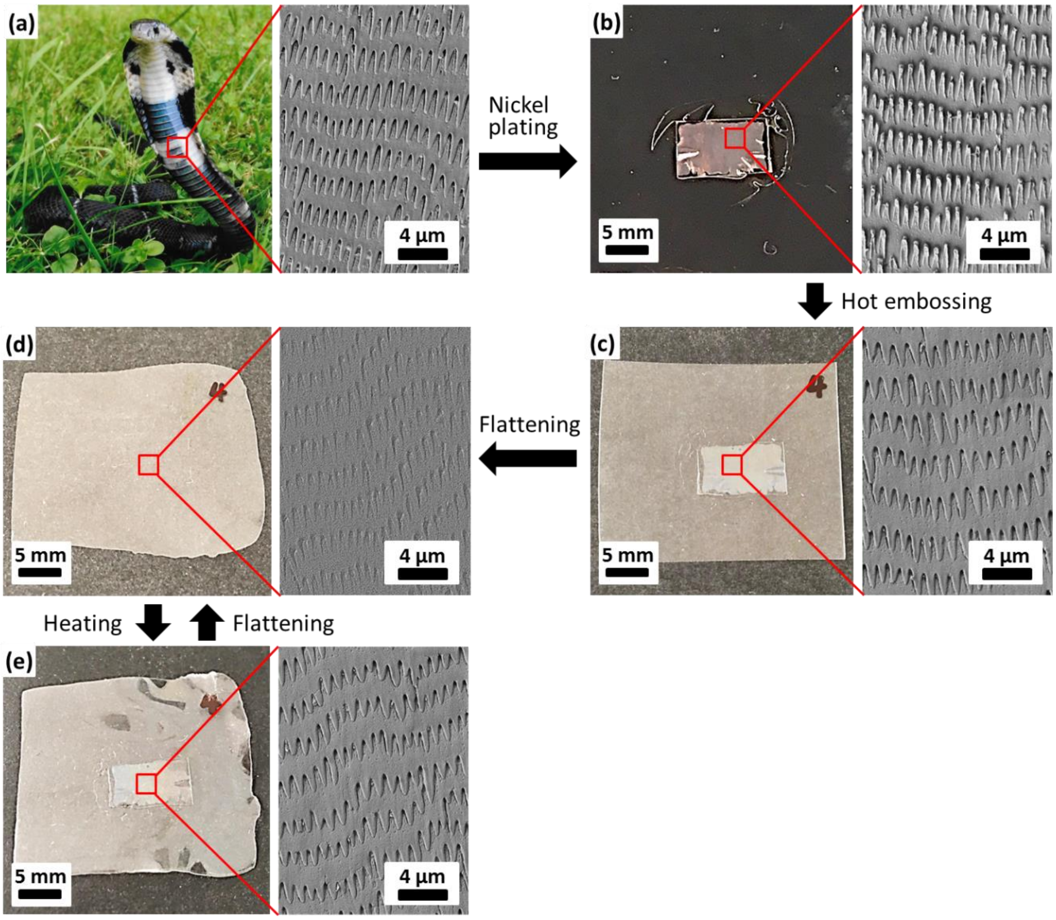

Figure 6.1: Procedures of defining, programming, and recovery of the SMP surfaces. In each sub-image, the left side shows the photos of the snake, Nickel shim as well as the SMP surface in its different states. The right side displays their corresponding SEM image revealing the respective topography of each surface. (a) A Chinese cobra (*N. atra*) in its natural habitat. The enlarged SEM image shows the oriented micro-fibril structures on its ventral scale. (b) A Nickel mold insert electroplated from a small, rectangular shaped ventral *N. atra* scale. It contains a negative pattern of micro-fibril structures observed by SEM. (c) The mold insert is pressed into the melt SMP by hot embossing and after cooling down a half-opaque, rectangular area on SMP surface, which is imprinted from (b), is produced. Similar micro-fibril structures as in (a) are imaged in this area indicating good replication quality. (d) After a flattening process, the rectangular area disappears and the whole SMP surface turns into transparent suggesting that the micro-fibril structures are significantly smoothed. The SEM image on its right side confirms this. (e) Further heating the SMP under a temperature of 55 °C causes the recovery of micro-fibril structures (half-opaque rectangular area) on the polymer surface. Both the appearance (see the photo) and micro-structures (see SEM image) in this state are very similar to its original state in (c). Flattening and heating process can be reversibly cycled allowing the SMP surface to switch its topography between the state shown in (d) and (e) for many times.

Ventral scales of the Chinese cobra (Figure 6.1 a) were selected as the biological template for replication as higher nano-steps and larger friction anisotropy at the micro-fibril ends were characterized on the ventral scales of this snake than the other snakes (see Chapter 5). The snake scales were cut into small pieces (around 10 mm × 7 mm) and glued onto the surface of a silicon wafer for Nickel plating (see Chapter 2.4.3). After the plating process, a mold insert with a negative micro-fibril pattern was obtained (Figure 6.1 b). Then the mold insert was pressed into the melt SMPs by hot embossing with 12 kN embossing forces and 155 °C embossing temperature. With this step and by subsequently cooling down to room temperature, the permanent shape of SMP surface embedded with replicated micro-fibril structures was successfully defined (Figure 6.1 c). To program a temporary topography with no apparent micro-fibril steps, the defined permanent shape SMP was further hot embossed with a flat plate under 8.5 kN embossing forces and 55 °C embossing temperature. Subsequently cooling down to room temperature, a temporarily smooth, unstructured SMP surface was obtained (Figure 6.1 d). Finally, placing the flattened SMP on a hot plate (*T* = 55 °C) released the inner forces and the polymer recovered the structured shape (Figure 6.1 e), which is similar to its original shape in Figure 6.1 c). Moreover, this recovered SMP surface can be further reprogrammed into the temporary state and then switched back to its structured shape for many cycles.

During this procedure, the topography of each surface was also examined by SEM. Micro-fibril structures on snake scale (Figure 6.1 a) together with their negative pattern on the Nickel shim (Figure 6.1 b) were clearly observed. The replicated micro-fibril structures on SMP surface (Figure 6.1 c) are indistinguishable from those on snake scales in both shape and size, which shows the excellent quality of the replication. After being flattened the micro-fibril structures nearly vanished in the temporary state (Figure 6.1 d). Further heating the SMP the micro-fibril structures reappeared again (Figure 6.1 e) and the surface shows no difference to its original state. Meanwhile, it is also possible to predict the existence of the micro-fibril structures by the transparency of the SMP surfaces. On both original and recovered state of SMP, a rectangular, half-opaque area was observed, which corresponds to the shape of Nickel shim. On the temporarily flattened surface, however, this area is not visible and the surface exhibits homogeneous transparency. The reduction of the fibril step height leads to the increase of the transparency on the flattened surface.

6.2 Wetting properties of SMP surfaces

The wetting performance of the SMP surface was first investigated. Besides the snake-inspired SMP surface, a flat plate embossed SMP surface was also introduced as a reference, aiming to figure out the influence of the micro-fibril structures on the wetting performance of the surface. Furthermore, the SMP surface might show different wettability in its different states. Thus, the three topographical states (original shape after replication, temporarily flattened shape, and recovered shape) of both surfaces were examined, respectively. Figure 6.2 shows the resulting equilibrium water contact angles on these SMP surfaces.

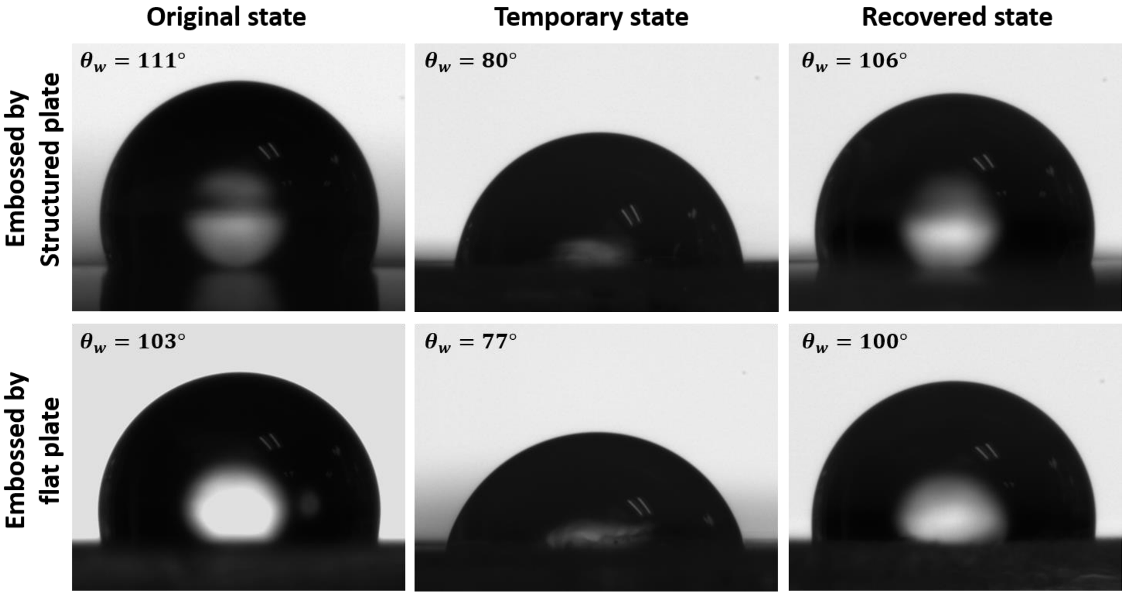

Figure 6.2: Equilibrium water contact angle on the structured and flat SMP surfaces. The results on the micro-fibril structured SMP surface are shown in the top line. The bottom line shows the results on the flat SMP surface. On both surfaces the original, temporarily flattened, and recovered state were investigated, respectively. The droplet volume was 1 µL.

The top line of Figure 6.2 displays the results on different states of the snake-inspired SMP surface. First, on the surface directly embossed from the structured mold insert (original structured state), the equilibrium contact angle was measured as about 111°. Interestingly, after being flattened into its temporary state, the surface showed an equilibrium contact angle of only around 80°. Subsequently, heating the surface on a hot plate (T = 55 °C) leads to a recovery to the structured surface again. The contact angle on the surface increased back to 106°. This phenomenon suggests inverse wetting performances (*i.e*. hydrophobicity and hydrophilicity) between the structured and flattened states of the SMP. Two reasons can be imagined to explain this. On the one hand, the micro-fibril structures on the original state were flattened when the surface was programmed into the temporary state, which might reduce the contact angle on the surface. Once the micro-fibril structures came back (*i.e*. the surface topography switched to the recovered state), the contact angle also increased back. On the other hand, temperatures and pressures were applied to the SMP surface during the flattening (programming) process, which changed the energy conformation state of the polymer chains and might have reduced the contact angle on the surface. Once heating the polymer, the contact angle increased back with the recovery of the energy state. Thus, to further understand this, the same contact angle measurement was also conducted on a flat plate embossed SMP surface and the results are shown in the bottom line of Figure 6.2.

One can observe that the same effect as for the structured SMP surface was found on the flat plate embossed SMP surface, *i.e.*, the surface is hydrophobic in the original (equilibrium contact angle is 103°) and recovered (100°) state, but it is hydrophilic in the temporary state (77°). The same flat plate was utilized to define the original state and to further program the temporary state, while the embossing forces and temperatures for these two states are different (same as the corresponding settings for the structured SMP surface in the top line). Hence, the difference of the wetting performance of these two states will be mainly caused by the variation of the surface chemistry. This means that a flat SMP surface without micro- or nanostructures can also behave inverse wetting properties switching between hydrophobic and hydrophilic regarding to its different states. Furthermore, it is also interesting to note that the contact angles on the flat plate embossed SMP surface (bottom line) are all slightly smaller than that on the snake-inspired SMP surface (top line). It seems that the micro-fibril structures can moderately enhance the hydrophobicity. Additionally, one can also see that the contact angle values of 111° on the snake-inspired SMP surface coincide with the results on the real snake scales (around 110° on the ventral scales of most snakes, see Table 4.2 in Chapter 4.3).

Lastly, it has to be mentioned that the above results are all equilibrium values, *i.e*., the contact angles are calculated when the water droplet rests stable on the surface. However, during the measurement we also observe that the temporary state of the SMP can absorb the water causing a reduction of the contact angle with time. The original and recovered state of the surface do not show the same property. To further investigate the water absorption of the SMP, the contact angle was measured on the three states of a flat SMP surface during a time period of 5 s. Figure 6.3 shows the time-lapse of the contact angle variation on each surface. On the original and recovered state, the measured contact angle was stable at their specific value (103° and 100°, respectively) within the investigating time. On the temporary state, however, once the water droplet was placed on the surface, the initial contact angle was around 84° at 0.2 s and then the value gradually reduced to 77° after 5 s. Both the original state and temporary state of the SMP surface were achieved with the same flat plate by hot embossing. For defining the original state, the embossing forces and temperatures were 12 kN and 155 °C, while for the programming of the temporary state the parameters were 8.5 kN and 55 °C, respectively. The temporary state of SMP surface shows an unstable wetting performance with decreasing contact angle with time, which might be caused by the variation of the energy state of the polymer chains in SMP.

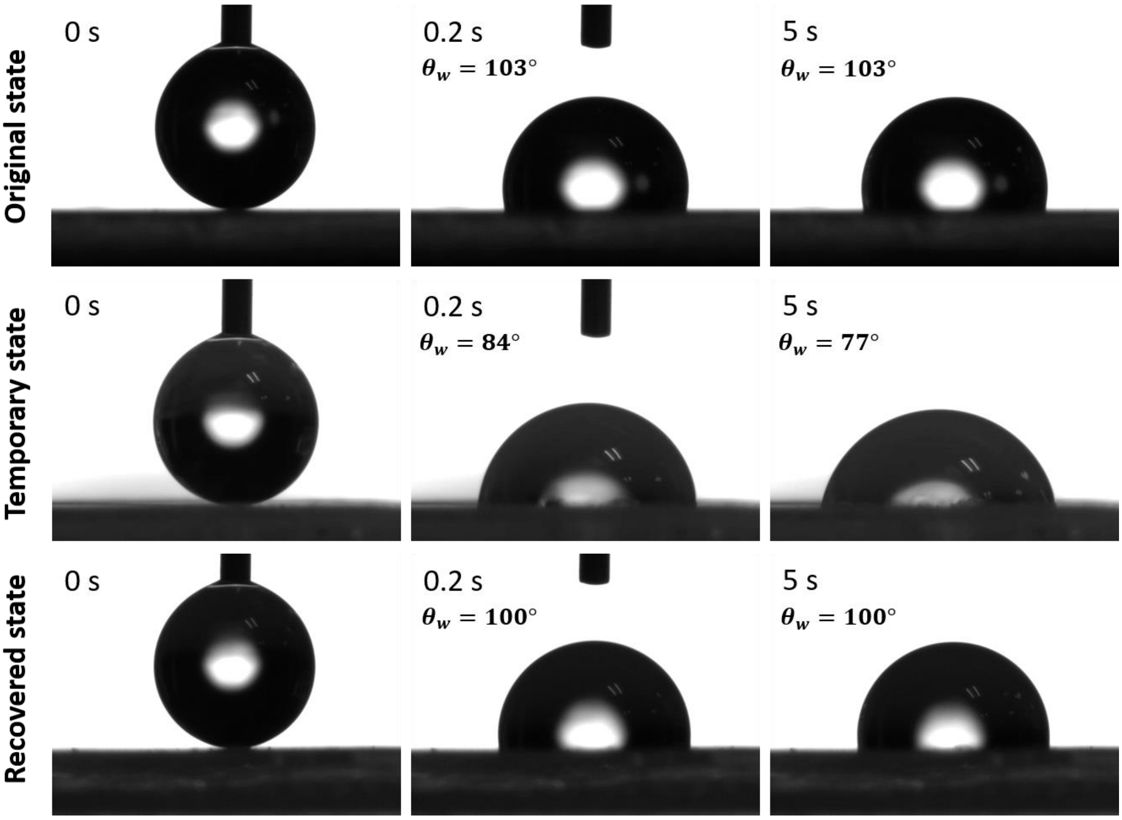

Figure 6.3: Time-lapse of a water droplet on the three states of a flat SMP surface. The SMP was embossed with a flat plate by the same procedure as in Figure 6.2. The contact angle on each surface was measured during a time period of 5 s. The droplet volume was 1 µL.

6.3 *In situ* step height and friction anisotropy evolution during the recovery of the flattened SMP surface

In this chapter, the step height as well as the friction anisotropy at the micro-fibril ends during the recovery process of the snake-inspired SMP surface from its temporarily flattened state to the recovered, structured state were characterized by AFM. The tunable friction anisotropy ability of the snake-inspired SMP surface is demonstrated and its shape-changing capability in terms of tuning the step height and friction anisotropy is calculated.

6.3.1 Topography and step height characterization

Figure 6.4 shows the topography image as well as a topographical line section across the fibril ends of a snake-inspired SMP surface in its flattened, intermediately recovered, and fully recovered state. The whole measurement was conducted *in situ* by an AFM which is originally equipped with a temperature-controllable heating stage. For each image, the scanning size was set to 10 µm × 10 µm. The SMP surface was replicated with the micro-fibril structures and then programmed into the temporarily flattened state by hot embossing. After that, the flattened SMP was placed on the heating stage of the AFM. The first measurement was applied to this flattened surface without any heating and a topography image of Figure 6.4 a) was obtained. Next, the heating stage was turned on with a temperature of 55 °C and the topography images were recorded with time steps of some seconds. After about 200 s, the micro-fibril structures were fully recovered. Figure 6.4 b) and c) show the results after the heating time of 10 s and 200 s leading to an intermediately recovered and a fully recovered surface, respectively. From the topography images, it can be seen that during the whole recovery process, the shape of single fibrils on SMP surface remains unchanged. Their size (both length and width), however, reduces slightly indicating an increase of the step height at the micro-fibril ends.

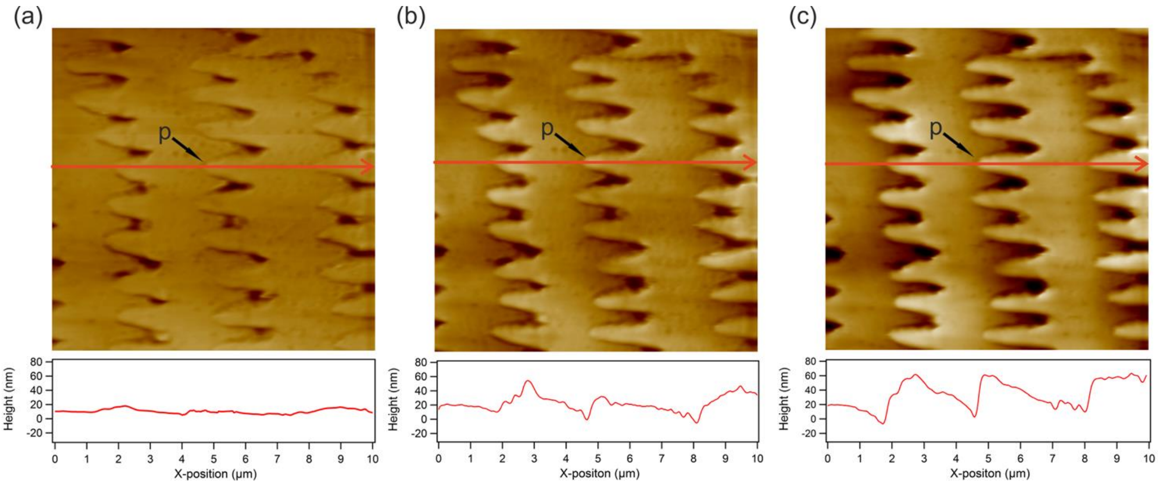

Figure 6.4: AFM images showing the topography evolution of a snake-inspired SMP surface during heating. The recovery of a temporarily flattened SMP surface to its permanent, micro-fibril structured surface over heating time was recorded. (a) The micro-fibril structures of a SMP surface were flattened by a flat plate with hot embossing and imaged by AFM before applying any heating. A topographical line section along the red arrow crossing the fibril ends in the AFM image is shown in the bottom panel, which indicates that the step height at the fibril tips is less than 6 nm. (b) Applying the heating for 10 s, an intermediate state before full recovery, with a step height of about 30 nm at the fibril tips was imaged. The AFM measurement was conducted *in situ* at the same position of the surface during the whole heating process. (c) After about 200 s heating time, the topography image and line section crossing the same fibril ends reveal that the step height at the fibril tips increased to almost 60 nm leading to the full recovery of the SMP surface.

The bottom panel of each image in Figure 6.4 shows the topographical line section along the red arrow in the upper AFM image, which scans longitudinally across the micro-fibril structures demonstrating the step height at the fibril ends. On the flattened SMP surface before applying any heating, a nearly flat line section over the 10-µm scanning range was observed (Figure 6.4 a). The step height at the fibril ends was characterized as less than 6 nm. After being heated for 10 s on the AFM heating stage ($T = 55$ °C), the corresponding line section across the same fibrils showed three significant nano-steps at the fibril tips. Their step height increased to more than 30 nm (Figure 6.4 b). Continuously heating the SMP until about 200 s and AFM imaging at the same position revealed that the nano-steps at the fibril ends were even higher with a height of almost 60 nm (Figure 6.4 c). Thus, the snake-inspired SMP surface features micro-fibril structures with tunable step height at their fibril ends, which can achieve desirable step height by simply heating the surface for certain time.

More specifically, Figure 6.5 shows the step height at one micro-fibril end (indicated by “p” in the AFM image in Figure 6.4) plotted as a function of the heating time during the SMP recovery process from Figure 6.4 a) to c). A logarithmic growing process similar to the description in [127, 177] was observed. An initial step height of 5.9 nm was measured, which corresponds to Figure 6.4 a). Once starting heating the surface, the step height increased precipitously to 55.0 nm within around 50 s. After that, with the heating time increasing, the growth of the step height was significantly slow down and finally reached a value of 58.7 nm after 200 s heating. Therefore, regarding the deformation of the step height, a shape-changing capability of about 1000% was achieved on the snake-inspired SMP surface, *i.e.*, it can switch its topography from a comparably flat surface to a highly structured surface with apparent nano-steps upon a heating stimulus. This tunable step height capability also suggests great potential of tuning friction anisotropy, which will be characterized in the next section.

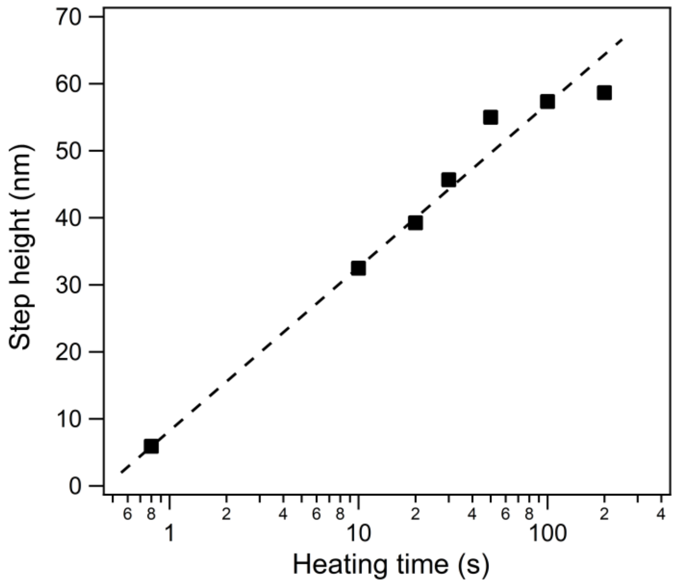

Figure 6.5: Step height evolution on SMP surface during a 200 s lasting heating process. The step height at the second fibril end indicated by “p” in the AFM image in Figure 6.4 was examined.

6.3.2 Friction anisotropy characterization

According to the results in Chapter 5, friction anisotropy is closely related to the step height at the micro-fibril ends on ventral snake scales. Hence, the excellent step height tuning performance of the snake-inspired SMP surface also implies a fabulous ability of tuning friction anisotropy. Similar to the frictional analysis of the snake scales demonstrated in Chapter 5, the friction anisotropy for a sharp AFM tip scanning upward and downward the nano-step of the micro-fibril end was examined on the snake-inspired SMP surface. During the step height characterization, an *in situ* measurement of the friction anisotropy at the second fibril step (indicated by “p” in Figure 6.4) during the SMP surface recovery process (from Figure 6.4 a to Figure 6.4 c) was conducted. The results are summarized in Figure 6.6.

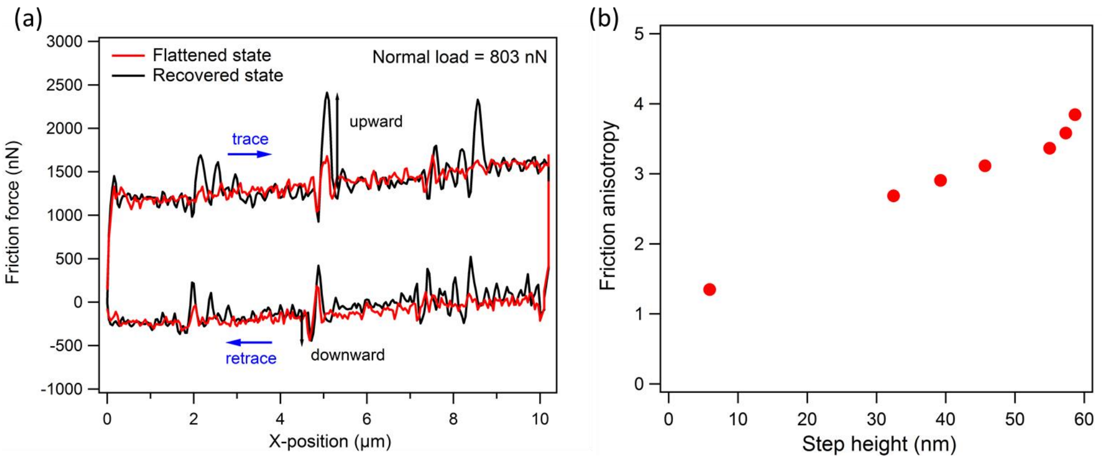

Figure 6.6: Friction loop and friction anisotropy evolution during the recovery process of the snake-inspired SMP surface. (a) Friction loops of a sharp AFM tip scanning the nano-steps up and down along the red arrow indicated in Figure 6.4. The

results of scanning on the flattened surface (corresponding to Figure 6.4 a) and on the fully recovered surface (Figure 6.4 c) are shown. The normal load was set to 803 nN. For all the three nano-steps at the fibril ends, when the AFM tip scans upward the step (trace), the frictional increase on the recovered surface (after 200 s heating) is much larger than that on the flattened surface (before heating). However, when the AFM tip steps downward (retrace), the frictional increase on both surfaces are almost equivalent. This suggests that the friction anisotropy on the recovered surface is more significant than that on the flattened surface. (b) Friction anisotropy plotted as a function of the step height during the recovery process of the snake-inspired SMP surface from Figure 6.4 a) to c) during 200 s heating time. Corresponding values from the second fibril end indicated by “p” in Figure 6.4 were plotted in the graph.

Friction loops of the AFM tip scanning in the opposite directions of stepping up- (trace direction) and downward (retrace direction) the micro-fibril steps along the red arrow indicated in Figure 6.4 are demonstrated in Figure 6.6 a). Results on the flattened surface (corresponding to Figure 6.4 a) and on the recovered, structured surface (Figure 6.4 c) are plotted in red and black, respectively. The normal load applied on both surfaces was kept constant as 803 nN. The SMP surfaces show similar friction loop as ventral snake scales (see Chapter 5.3.1). Significant frictional increases (peaks) were observed on both SMP surfaces when the AFM tip scans upward and downward the nano-steps of the micro-fibril ends. The frictional increase for the AFM tip upward the step is much larger than that for downward direction. The black arrows in Figure 6.6 a) marked the case at the second fibril step. However, during the AFM tip scanning on the terraces of the micro-fibrils (non-step area), the frictional signals were relatively flat. All these results demonstrate that the snake-inspired SMP surface shows the same frictional effect (*i.e.* friction anisotropy) as ventral snake scales at their micro-fibril steps.

Furthermore, comparing the frictional increase at the same fibril step between the flattened surface and the recovered structured surface (red and black peaks in Figure 6.6 a), the peak for upward the step on the recovered surface is much higher than that on the flattened surface even though the normal load applied on both surfaces was the same. However, for the tip downward scanning, the frictional increases on these two surfaces are very equivalent. This outcome suggests that the recovered structured SMP surface (Figure 6.4 c) shows more noticeable friction anisotropy than the temporarily flattened surface (Figure 6.4 a). The higher nano-steps at the micro-fibril ends on the recovered structured surface lead to larger friction anisotropy if compared to the flattened surface.

Similar to the frictional analysis in Chapter 5, increasing the normal load on the surface and recording the frictional increase at the friction peak result a linear increase relationship. The friction coefficients for the AFM tip scanning upward and downward the nano-steps can be acquired by calculating the slope of this linear increase [72]. Friction anisotropy is calculated by the same method as in Chapter 5 (the friction coefficient for the AFM tip upward a step divided by that for downward scan) in order to quantitatively analyze its evolution on the surface during the SMP recovery process. The friction anisotropy at the second fibril step (marked by “p” in Figure 6.4) was plotted as a function of its step height during the recovery of the temporarily flattened surface to its recovered structured surface over heating time. The results are summarized in Figure 6.6 b). During 200 s heating process, with the step height increasing from nearly 6 nm to almost 60 nm, the friction anisotropy increased almost linearly from 1.35 (on the temporarily flattened surface in Figure 6.4 a) to 3.84 (on the recovered structured surface in Figure 6.4 c), realizing a nearly 300% friction-anisotropy-changing capability.

Therefore, the snake-inspired, topography switchable SMP surface can achieve a function of tuning friction anisotropy from a nearly isotropic friction to a considerably anisotropic friction by controlling the nano-step height at the micro-fibril ends. Besides this, the snake-inspired SMP surface is also able to be reversibly switched between the structured and flattened topography for many cycles via heating or flattening process, making it an intelligent, tunable friction anisotropy element. Another even more fascinating ability of this smart surface is that the recovery of SMP can be intentionally interrupted by abruptly terminating the heating stimulus and cooling down to room temperature at any arbitrary time, which will create a surface with appropriate step height and ultimately lead to desirable friction anisotropy on the surface.

6.4 Long-term stability and reusability

6.4.1 Long-term stability

As a temperature sensitive element, the snake-inspired SMP surface should enable a long, and stable working time as long as the surrounding temperature is well controlled within the required ranges. Here, we call this type of requirement long-term stability. For such a friction anisotropy tuning element with micro-fibril structures, the long-term stability of the step height at the fibril ends is a crucial parameter. Moreover, this time dependent stability should also be effective on the different SMP states. Thus, in this section, the long-term stability of the nanoscale fibril step height on four different states of the snake-inspired SMP surface was examined. Samples of an original structured surface directly from replication, a temporarily flattened surface, a partly recovered surface, and a fully recovered structured surface were weekly monitored over a time period of three months.

For the preparation of these tested samples, first, the same Nickel shim (Figure 6.1 b) was utilized to press into the SMPs by hot embossing. The embossing temperature and forces were kept consistent (155 °C & 12 kN) during the replication process (from Figure 6.1 b to c). In total, four SMP samples were replicated with micro-fibril structures on their surface. Among them, the first sample (original structured surface) was directly obtained after embossing while the other three were further flattened by a flat plate (55 °C & 8.5 kN). One of the flattened SMP surfaces was kept as the second tested sample. After that, the left two flattened samples were placed on the hot plate (55 °C) for 10 s and 200 s. Subsequently cooling down leads to a partly recovered surface (the third sample) and a fully recovered structured surface (the fourth sample), respectively. All the four samples were stored in a fridge (4 °C) and measured at room temperature, which are both well below the switching temperature (T_{switch}) of the SMPs.

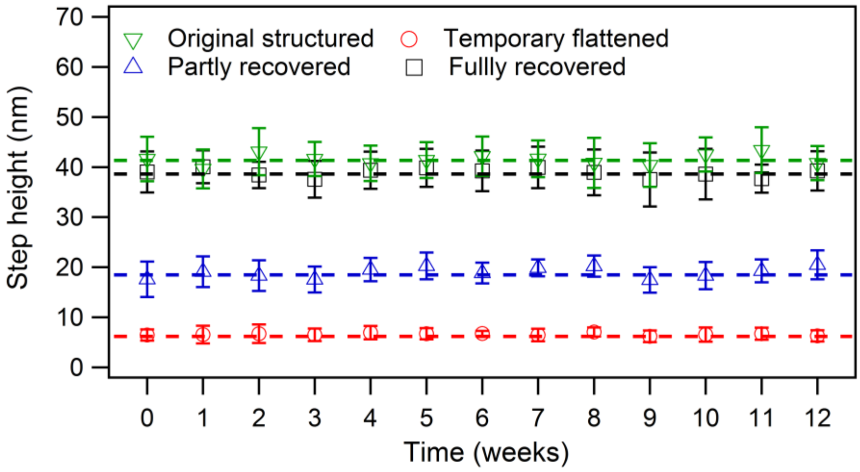

Figure 6.7: Long-term stability of the step height on the snake-inspired SMP surfaces. The step heights on four SMP surfaces including an originally structured, a temporarily flattened, an intermediately recovered, and a fully recovered structured surface were examined by AFM over 12 weeks. The temperature was well controlled below T_{switch} during the storage and measurement of all samples. Each data point in the graph was averaged from 40 values at five different positions and the corresponding error bar represents the statistical error. The dashed lines represent the overall averaged step height of each data set (SMP sample) over 12 weeks.

The averaged step height on each sample surface was weekly checked by AFM over a time span of 12 weeks. The results are summarized in Figure 6.7. On each sample, five different positions were examined and at each position eight random step heights were characterized. Thus, every data point in Figure 6.7 was averaged from 40 measured values. Their corresponding statistical error was calculated and plotted. It can be seen that on each sample the averaged step height varies very gently over the investigating time, *i.e.*, the step height on the SMP surface is stable on any arbitrary stage of its shape changing period (*e.g.* original state directly from replication or any intermediate state of its flattening/recovery cycle) as long as the temperature is well controlled below T_{switch}. The snake-inspired SMP surface possesses remarkable long-term stability. Moreover, the overall average value of the step heights on each individual sample over 12 weeks was calculated and accordingly plotted as the dashed line in Figure 6.7. For the original structured surface, the averaged step height is 41.5 nm, while the temporarily flattened sample shows an average value of only 6.6 nm. The results for the partly recovered surface (heating 10 s) and the fully recovered surface (heating 200 s) are 19.0 nm and 38.9 nm, respectively. The calculated average step heights on the fully recovered surface and the original surface are very approximated to each other, revealing the excellent, nanoscale shape-memory and -recovery ability of the snake inspired SMP surface.

6.4.2 Reusability

Equally important as long-term stability is the reusability which represents the number of the possible programming/recovery cycles of the SMP surface. It is another indispensable characteristic for a smart, friction anisotropy tuning device. A high reusability allows the same SMP surface being repeatedly used for many times (cycles), which will greatly reduce the fabrication cost and improve the applicability. Thus, in this section, the flattening/recovery cycle was repeatedly applied to a snake-inspired SMP surface for several times to evaluate its reusability. After each flattening or recovery process, the step heights of the micro-fibril ends on the surface were examined by AFM. A new fabricated snake-inspired SMP surface was tested with 11 subsequent flattening/recovery cycles. The step heights on the flattened surface as well as its corresponding recovered structured surface in each cycle were characterized at five different positions. Eight different nano-steps were measured at every position. The averaged step heights and their corresponding statistical errors are summarized in Figure 6.8.

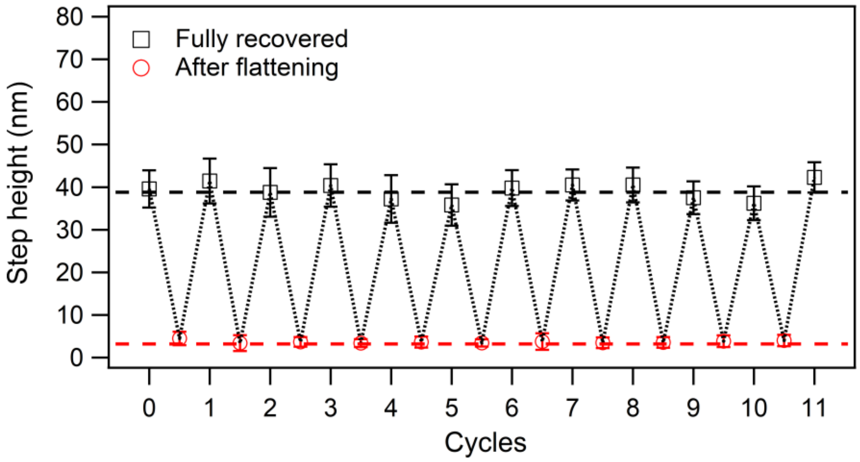

Figure 6.8: Reusability of the snake-inspired SMP surfaces with programming cycles. Fibril step heights on the same SMP surface switch regularly between around 5 nm and 40 nm during 11 consecutive flattening/recovery cycles. Each data point in the graph was averaged from 40 measured values at five different positions and the corresponding statistical error was shown. The dashed lines represent the overall average step height on the flattened surface (red) and the recovered structured surface (black), respectively.

In each flattening/recovery cycle, the nano-step at the micro-fibril ends was programmed into about 5 nm height on the flattened surface and then fully recovered to nearly 40 nm height with sufficient heating time (300 s). The same performance was observed in all the flattening/recovery cycles. More valid cycles can be also expected. Thus, the snake-inspired SMP surface is able to tune the nano-step height at the micro-fibril ends with stable performance for at least 11 effective working cycles, revealing excellent reusability. In this case, it can be concluded that the friction on the snake-inspired SMP surface can be well controlled to reversibly transit between near isotropic and significant anisotropic through tuning the step height at the micro-fibril ends, and this tunable ability also enables a long, stable working time as well as several reliable flattening/recovery cycles.

6.5 Application of the snake-inspired SMP surfaces

The snake-inspired SMP surface was characterized to be an excellent tunable friction anisotropy element with the ability of switching between nearly isotropic and comparably anisotropic friction along the micro-fibrils. The surface with such special features can be potentially used in applications which demands uni-directional transport of micro-particles such as dry self-cleaning coatings without any liquid. Besides this, the fabulous long-term stability and reusability of the surface also allow it to be an ideal device in industrial implementations. Therefore, in this section, transportation experiments of granular particles unidirectional moving on the snake-inspired SMP surface were performed.

6.5.1 Experimental setup

Figure 6.9 shows the photos of the whole setup used for the transportation experiments. PDMS micro-spheres (100 µm - 200 µm diameter) and sea sand particles (100 µm - 300 µm diameter) were transported, respectively. The snake-inspired SMP surface was employed as a substrate to unidirectionally transport these granular particles through a random vibration. Besides this, a real ventral snake scale (*N. atra*) was also introduced as a reference. The movement of the granular particles on the substrate was observed with a microscope.

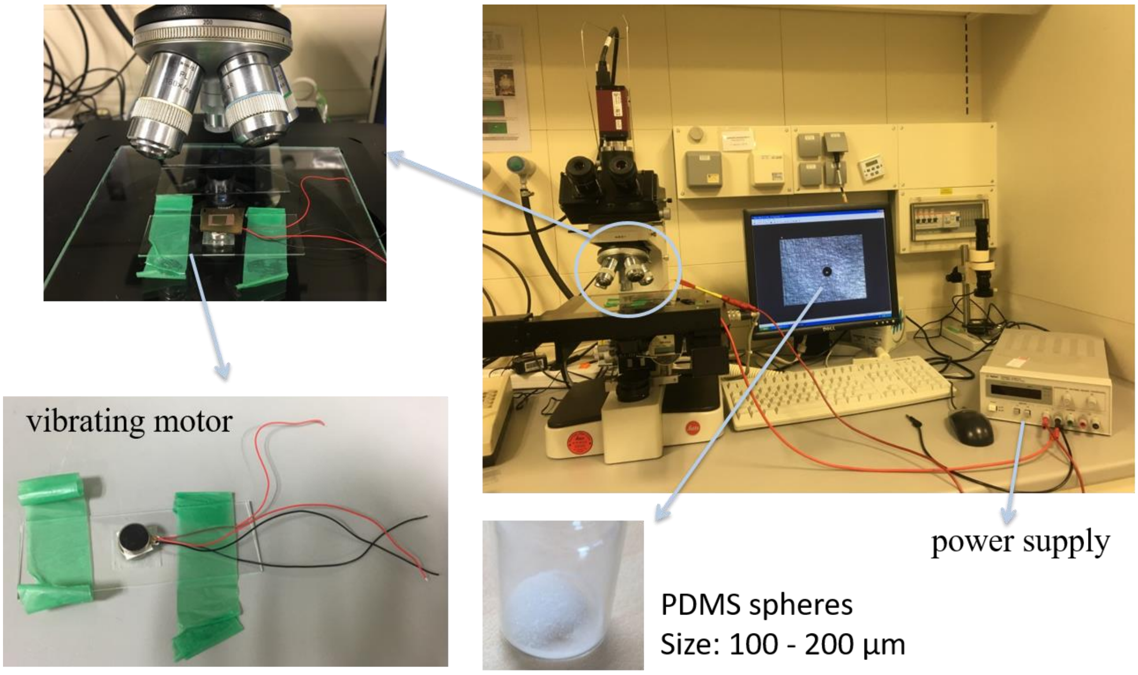

Figure 6.9: Setup for the micro-particle transportation experiments. A vibrating motor was utilized to randomly shake the snake scale or the snake-inspired SMP surface. PDMS spheres, which are 100 µm - 200 µm in diameter, were used for transportation. The whole setup was observed with an optical microscope and the movement of the microsphere was tracked and recorded by a visualizing monitor.

First, the snake scale or SMP surface was glued on a piece of silicon wafer with a double-sided adhesive tape (Fotostrip, Tesa® AG, Germany). This is conducted for the aim of keeping the substrate surface as flat as possible to minimize the influence of the surface curvature during the transportation of micro-particles. Subsequently, the snake scale as well as the snake-inspired SMP surface was sputter-coated with a 10 nm-thick, homogeneous silver layer which will lead to a low surface energy in order to reduce the adhesion forces between the micro-particles and the substrate surface. After that, the silicon wafer with the snake scale or SMP surface on its top was fixed onto a commercial coin mobile phone vibrating motor (10 mm diameter and 2.7 mm thickness, Brunswick Corporation, USA) with double-sided adhesive tapes. This vibrating motor can produce random vibrations on the surface and then exert these vibrations to the top surface of the snake scale or the snake-inspired SMP. The rated voltage and current of the vibrating motor is 1.5 V and 0.05 A, respectively. Next, the whole setup (*i.e.* the vibrating motor together with silicon wafer and sample surfaces on top) was mounted on a glass slide and fixed under an optical microscope (ProMicron, Germany) with a green tape (see Figure 6.9).

The vibrating motor was powered by a voltage and current adjustable power supply (E3620A, Agilent Technologies Inc., UK) via electricity conductive wires. The microspheres used for transportation are PDMS powder particles with their diameter in the range of around 100 µm - 200 µm. The micro sand particles are pure sea sand purchased from Merck KGaA, Darmstadt, Germany. The size of the micro sand particles is around 100 µm - 300 µm. The micro-particle was individually picked up and transferred onto the surface of the snake scale or the snake-inspired SMP with a tweezer. Finally, switching on the power supply causes the random vibration of the motor as well as the substrate surface. The movement of the microsphere or sea sand on the substrate surface was tracked and recorded with a computer monitor which is connected to the microscope during the experiment.

6.5.2 Microsphere transportation on the snake scale and SMP surfaces

Figure 6.10 shows the time-lapse of unidirectional transport of single PDMS microsphere on substrates of the snake scale and the snake-inspired SMP surface (in its different topographical states), respectively. The substrate orientation was intentionally adjusted to allow the micro-fibrils to point towards the bottom of the visualized image (see the inset SEM images). All the substrates were sputter-coated with a homogeneous layer of silver. First, a piece of *N. atra* ventral scale was utilized as transportation substrate. The PDMS microsphere was placed on the upper area of the surface (see images in Figure 6.10 a). Switching on the power supply of the vibrating motor causes the substrate to shake randomly. Figure 6.10 a) displays the movement of the microsphere on the vibrated snake scale. It can be seen that the microsphere moved directionally along the micro-fibril structures in downward the step direction (towards the image bottom) for about 0.42 mm within 14 s vibrating time. This phenomenon also coincides with the results of the frictional characterization on *N. atra* ventral scale in Chapter 5.3.1. The significant friction anisotropy along the micro-fibrils causes the microsphere unidirectionally travelling in downward the step direction on the surface of ventral snake scales.

Next, the same experiment was also conducted on an original structured SMP surface which was directly replicated from *N. atra* ventral scale via hot embossing. The movement of the microsphere on this surface is summarized in Figure 6.10 b). A similar unidirectional motion along the micro-fibrils in downward the nano-step direction was observed, while only 6 s were needed to transport the microsphere for the same distance (0.42 mm) on this randomly vibrated SMP surface. This phenomenon further confirms the characterization results of the friction anisotropy on the structured SMP surface in Section 6.3.2. Besides this, it also indicates that the snake-inspired SMP surface can show as excellent friction anisotropy as a real snake scale, making it an ideal element for engineering applications.

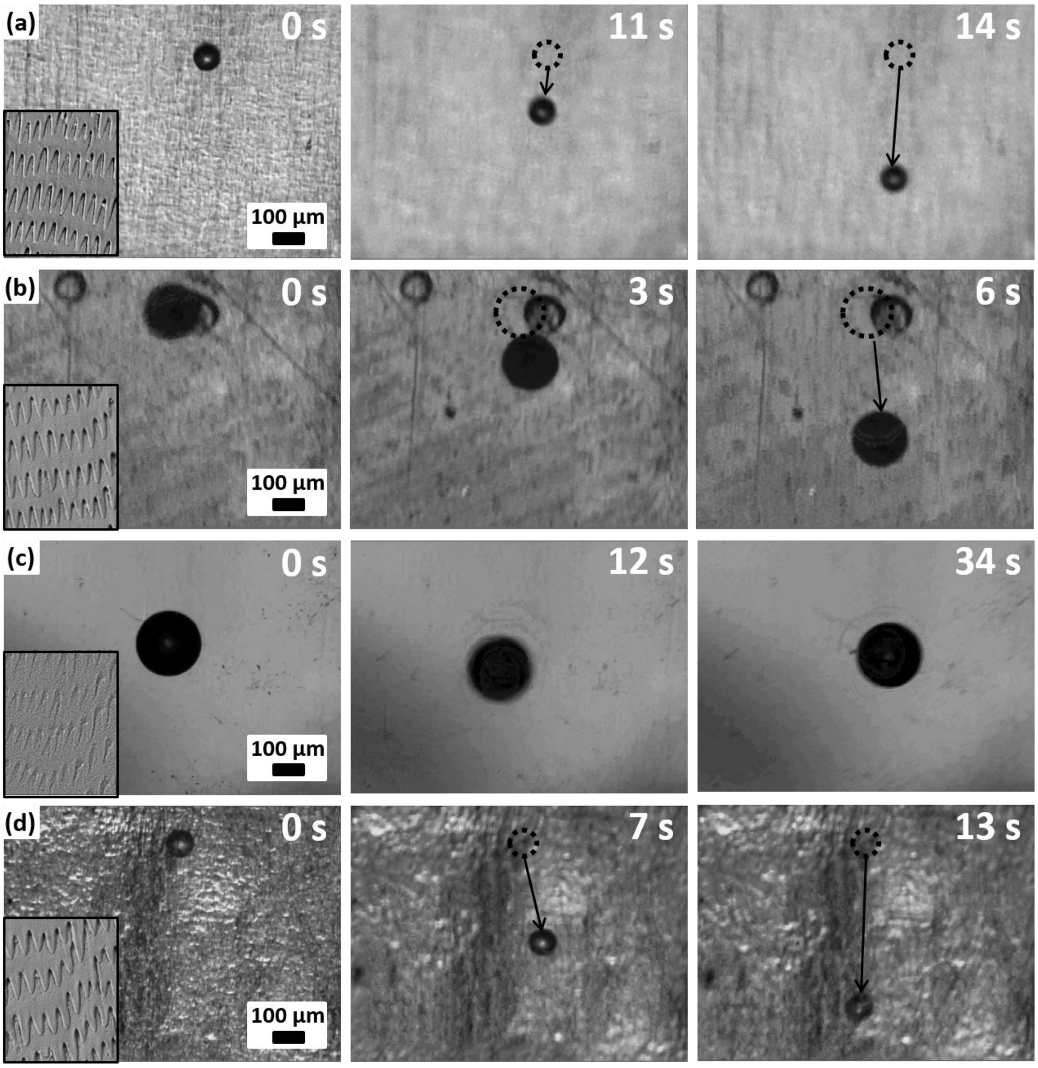

Figure 6.10: Time-lapse photos of the unidirectional transport of single PDMS microsphere. Surfaces of (a) *N. atra* ventral scale, (b) original shaped SMP surface with replicated micro-fibril structures, (c) temporarily flattened SMP surface, and (d) recovered structured SMP surface were used as the substrate for transportation. The orientation of the micro-fibrils on each substrate surface points towards the bottom of the image, as indicated in the inset SEM images. The dashed circle in (a), (b), and (d) represents the original position of the microsphere, and the black arrow reveals its unidirectional movement. All sample surfaces were sputter-coated with a 10 nm silver layer to reduce the adhesion between the microsphere and the surface. A random vibrating excitation was applied to the substrates for driving the microsphere to move.

Subsequently, the original structured SMP surface was flattened into a temporarily non-structured topography. The resulted surface was used as the substrate to conduct the same transportation experiment. The movement of the PDMS microsphere on this surface is recorded in Figure 6.10 c). One can see that, in this case, the microsphere moves randomly within a very small amplitude (maximum 0.1 mm) around its original location during a vibration time of 34 s. This indicates that the flattened SMP surface behaves isotropic friction in all directions and cannot unidirectionally transport the microsphere as on its original structured topography.

Finally, the flattened SMP was placed on a hot plate (T = 55 °C) and heated for 300 s in order to completely restore the micro-fibril structures on the surface. Figure 6.10 d) shows the movement of the microsphere on the vibrated recovered, structured surface. After 13 s vibration, a distance of 0.51 mm along the micro-fibrils in stepping down the nano-step direction was achieved. Due to the curving of the surface during the heating (recovery) process (see Figure 6.10 d), the transporting ability of the recovered SMP surface is not as excellent as its original state (0.42 mm@6 s). This might be also caused by the smaller size of the utilized microsphere in this experiment than that on the original state surface. Nonetheless, the recovered structured surface can still feature friction anisotropy for unidirectional delivery of the microsphere. Consequently, the concept of employing the snake-inspired SMP surface as a smart, friction isotropy/anisotropy switchable platform is proved to be feasible, which will have a great potential in applications for dry self-cleaning or particles sorting.

6.5.3 Trajectories of microspheres

To further test the long-distance transporting capability of the snake scale as well as the snake-inspired SMP surface, these substrates were continuously vibrated for a longer time. The movement of the microsphere was monitored and tracked during the whole vibration time. The trajectories of the microsphere travelling on the Chinese cobra ventral scale and different states of the snake-inspired SMP surface (*i.e.* original replicated, flattened, and recovered) were plotted in Figure 6.11, respectively.

On the snake scale (Figure 6.11 a), the original structured SMP surface (Figure 6.11 b), and the recovered structured SMP surface (Figure 6.11 d), the microsphere travelled an extremely long distance in Y direction (corresponding to the direction of stepping down the micro-fibril steps). In X direction, however, the moving distance is very short, which is evaluated as the maximum distance away from its original position. More specifically, Figure 6.11 a) shows the trajectory of a microsphere moving on ventral snake scale. The microsphere travelled 5.50 mm in Y direction but only 0.50 mm in X direction with the substrate vibrating for 43 s. The values are 4.30 mm and 0.26 mm for the original structured SMP surface which is directly replicated from the snake scale (see Figure 6.11 b). The vibration time of this surface is 20 s. Figure 6.11 d) illustrates the results on the recovered structured SMP surface. A transporting distance of 4.75 mm in Y direction and a maximum of 0.45 mm in X direction was observed. The overall travelling time on this substrate is 41 s. This means that the micro-fibril structures on the snake scale and SMP surfaces can continuously guide the microsphere for unidirectional movement through a random vibrating excitation.

A nearly 5 mm travelling distance was achieved on the SMP surfaces. This distance is mainly limited by the length (along the micro-fibrils direction) of the sample surface. Due to the maximum length of single snake scale (about 6 mm), the replication of micro-fibril structures from snake scale to SMPs can only produce structured SMP surface in a maximum length of about 5 mm (see Figure 6.1 c). Thus, the largest distance of the microsphere travelling from the top to bottom edge of the SMP surface is about 5 mm. Longer transporting distance can be expected on larger SMP samples. However, as shown in Figure 6.11 c), on the flattened SMP surface the microsphere did not unidirectionally travel but moved randomly around its initial position within the range of about 0.1 mm during 37 s vibration time. This indicates isotropic friction in all directions on the surface due to the flattening of the micro-fibril structures. As a result, the SMP surface in this state cannot achieve the same function as in its structured state. This trajectory also coincides with the results in Figure 6.10 c).

Therefore, the snake-inspired SMP surface behaves anisotropic friction like ventral snake scales, which is able to achieve the transportation of a microsphere in downward the fibril step direction for nearly 5 mm. More interestingly, the SMP surface can be also programmed into a flattened topography exhibiting near isotopic friction in all directions on the surface, which displays no unidirectional transporting ability. Furthermore, the subsequent recovery process allows the SMP surface to switch back to its structured topography with anisotropic friction again by simply heating the surface. Such programming/recovery characteristic makes the snake-inspired SMP surface much superior to the biological snake scale. The smart, switchable friction anisotropy capability enables the snake-inspired SMP surface an intelligent, desirable functional platform for unidirectional delivery of micro-particles in many applications.

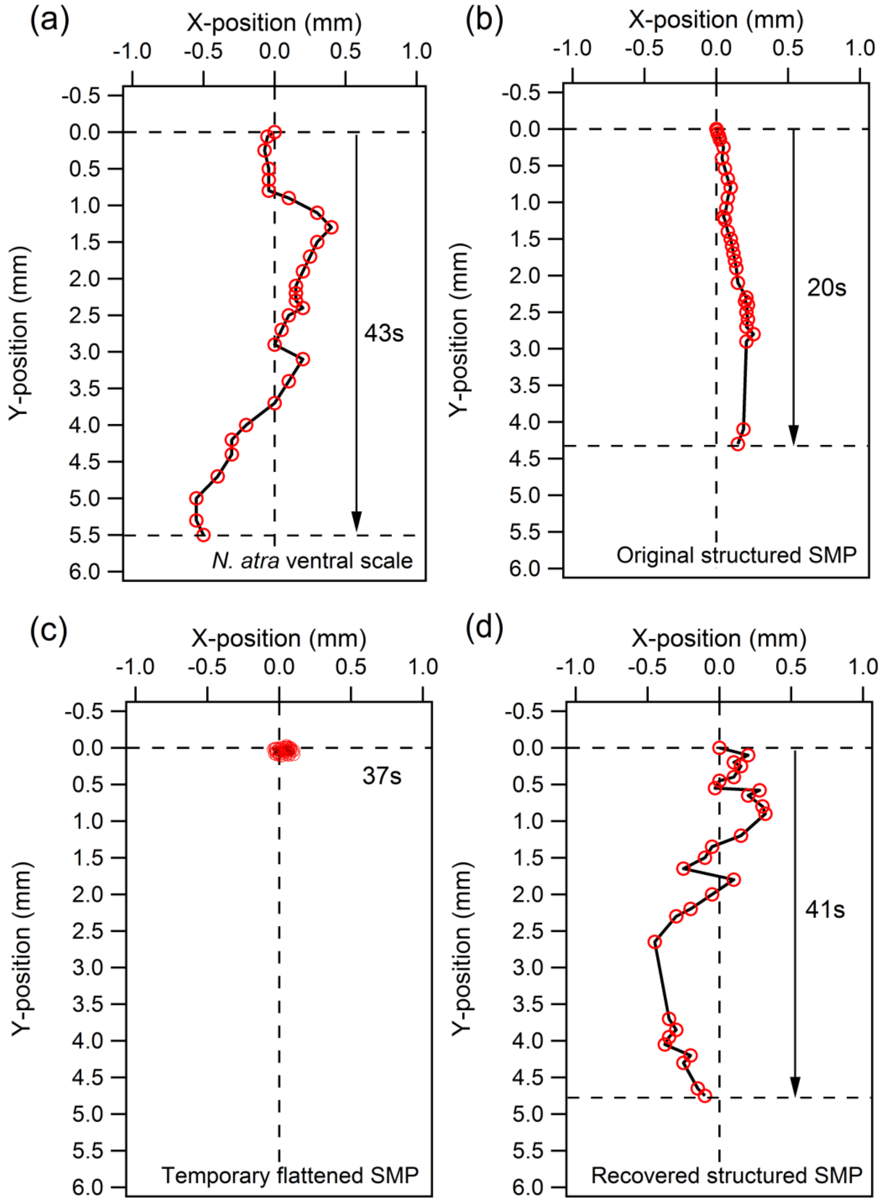

Figure 6.11: The tracked trajectory of a PDMS microsphere travelling on different substrates. Surfaces of (a) *N. atra* ventral scale, (b) original SMP replicated with micro-fibril structures, (c) temporarily flattened SMP, and (d) recovered structured SMP were investigated. All sample surfaces were sputter-coated with a silver layer of about 10 nm. The microsphere as well as its travelling time on different surfaces is different. In each trajectory, nearly 30 data points were tracked, while the overall time interval of each tracking experiment was not the same.

6.5.4 Application for dry self-cleaning without liquids

The experiments of unidirectional transport of granular particles by the snake-inspired SMP surface imply a potential application for dry self-cleaning. In difference to the traditional self-cleaning coatings which are mostly based on the superhydrophobicity of the surface [178-182], the snake-inspired SMP surface achieves self-cleaning through a random vibration instead of water or any other liquids. Besides this, as shown in Chapter 4.5, the ventral scales of snakes show similar spectral transmittance properties as their spectacle scales revealing high transmittance (nearly 90%) in visible light spectrum. This means that the micro-fibril structures do not influence the optical transmittance very much. The NOA 88 replica of *N. atra* in Figure 5.12 showing a transparent surface also confirms this. These advantages will be very attractive for photo-voltaic modules in rainless areas, even though the silver coating on our current surface is not suitable for the applications on solar cells. Therefore, an experiment of self-cleaning microspheres or micro sand particles (sea sand, 100 µm - 300 µm in diameter) on the vibrated snake-inspired SMP surface was conducted. The results are shown in Figure 6.12.

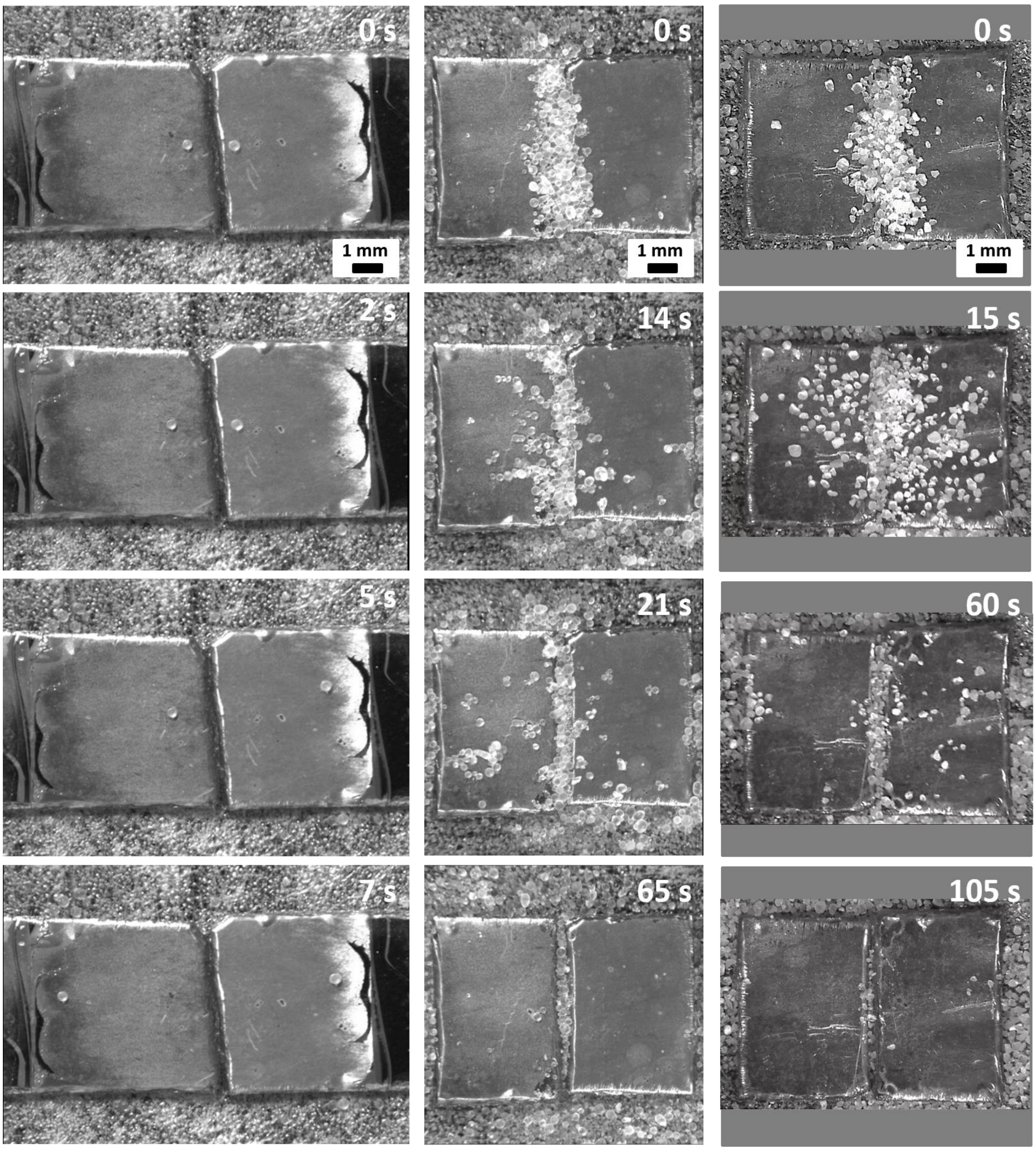

Figure 6.12: Dry self-cleaning experiments on the snake-inspired SMP surfaces. Time-lapse of the movement of PDMS microspheres or micro sand particles on two pieces of inversely orientated SMP surfaces is illustrated. The micro-fibril structures on the left-side SMP surface point towards left, while on the right-side SMP surface the micro-fibril structures are towards right. The left column in the figure shows the case of self-cleaning single PDMS microsphere. The middle column shows the self-cleaning of many microspheres simultaneously. The right column is a similar experiment as the middle, but the sea sands were used. The granular particles were initially placed on the stitching area of the two SMP surfaces

(center of each sub-image). With the vibration exerted to the surface, both microspheres and sea sand particles were guided to move along the micro-fibril structures in downward the step direction (towards the left and right side of each sub-image). After some tens of seconds, most of the granular particles were removed from the surfaces achieving a dry self-cleaning function. All the surfaces were sputter-coated with a silver layer as before.

To obtain reliable results, two pieces of SMP surfaces were placed in opposite orientations, *i.e.*, the micro-fibril structures on the left SMP surface point towards left, while those on the right SMP surface point towards right. First, a single PDMS microsphere was individually placed on each SMP surface. Both spheres were located at the center of the image (see the images in the left column in Figure 6.12). Once starting the vibration, one can see that they separated towards inverse directions. The one on the left SMP surface moved to the left, while the one on the right surface moved to the right, which corresponds to the direction of downward the micro-fibril steps on each SMP surface. After about 7 s, the two microspheres reached the far left and right side of the image, respectively.

For solar cells in industrial applications, many different sized dusts or contaminations simultaneously exist on their surface. Thus, the middle column of Figure 6.12 shows a simulation of this case for self-cleaning many different sized microspheres at the same time. The two SMP surfaces were arranged similarly to that in the left column. Before starting the vibration, numerous microspheres were placed at the center of the image. Then with the substrate vibrating, one part of the microspheres (those on the left SMP surface) moved to the left edge of the image and the others (those on the right SMP surface) moved to the right edge. Finally, after about 65 s, the surfaces were almost cleaned with no apparent microspheres observable. In the right column of Figure 6.12, the same experimental procedure was conducted with sea sand particles (in irregular shapes if compared to microspheres). Switching on the vibration, one can observe a similar phenomenon as in the middle column. After about 105 s vibration, the sand particles were completely removed. Consequently, the snake-inspired SMP surface shows excellent abilities of self-cleaning microspheres and sea sand particles based on a random vibration instead of water or other liquids, which will have an advantage as dry self-cleaning coatings for photo-voltaic modules in arid environments. Such concept can be also applied for particles sorting or separation.

A shortened version of this chapter is in preparation as the article “Snake-inspired, tunable anisotropic frictional surface based on shape-memory polymers for unidirectional transport of microscale particles”, by Weibin Wu, Markus Guttmann, Marc Schneider, Richard Thelen, Matthias Worgull, Guillaume Gomard, and Hendrik Hölscher.

7 Summary and outlook

In summary, this thesis systematically examined the tribological properties of the molted scales of sandfish as well as twelve snake species, and the findings were subsequently used as an inspiration for the fabrication of an artificially engineered surface. With the analysis of the function of the microstructures on the scales from different regions of the reptiles, the correlation between friction anisotropy and typical nano-step structures existing on sandfish and snake scales was established. The outcome suggests a general nanoscale mechanism of reptiles optimizing friction for locomotion. Inspired by this, a smart, tunable friction anisotropy surface made from a SMP was developed. An application of unidirectional transport of micro granular particles by the inspired surface for dry self-cleaning uses was demonstrated. In compliance with the scientific objectives of this work, the main findings together with an outlook on further studies are given in the following.

Tribological properties of sandfish and snake scales

Tribological properties including adhesion, friction, and abrasion resistance of sandfish and snake scales were examined via various AFM techniques and further compared with that of some typical technical materials. Besides a conventional sharp tip, AFM probes with different size and surface chemistry were fabricated and utilized for the characterization. The experimental results show that scales of sandfish and snakes do not show more excellent adhesion properties than technical surfaces on the nanoscale. In agreement with the classical theory, a larger tip size (*i.e.* probe diameter) usually induces a larger adhesion force, while there is no significant dependence of adhesion on the probe surface chemistry. Subsequent comparison between sandfish and snakes reveals that the adhesion of sandfish scales is not extraordinary small, that it is even larger than for snakes. For the analysis of the frictional properties, friction coefficients were characterized by conducting load dependent friction measurements on the respective sample surfaces. The friction measured on dorsal sandfish scales is lower than that on most technical materials like Teflon, PMMA, or silicon. Interestingly, ventral scales of a psammophile snake (*S. diadema*) have an even smaller friction coefficient than sandfish scales, but they both are not as low as the dry lubricant HOPG. The shape or size of the exploited tip did not influence the overall outcome. Abrasion resistant experiments on sandfish and snake scales as well as on technical materials demonstrate that sandfish resists normal load slightly better than most technical materials, but it is not stable for longer scratching periods.

Consequently, scales of snakes and sandfish only feature superior frictional properties (small friction coefficient) if compared to the investigated technical surfaces. The adhesion and abrasion resistant properties are nearly alike among the characterized biological and technical samples. Scales of snakes show even better tribological properties than that of sandfish. We, therefore, conclude that the fabulous tribological properties of sandfish swimming under sand are not exclusively caused by its scales. Some other origins such as the elastic properties of its epidermis or the dynamics of locomotion are also very likely important for enabling sand swimming in combination with low wear rates. Thus, further research on the tissue underneath the epidermis as well as the dynamics of the swimming will be of high interest. Such studies will be helpful for the development of new robots aiming to locomote in granular materials.

Function of the microstructures on scales from different regions of snake body

Micro- and nanostructures on the dorsal, ventral, and spectacle scales of twelve snake species were imaged by SEM. For an individual snake, micro-ornamentations on scales of these three regions are totally different. On different snake species, however, the scales from the same region show very similar micro-ornamentations, *e.g.*, oriented micro-fibril structures on ventral scales or stitching polygon structures on spectacle scales. Interestingly, dorsal scales of the investigated snakes display dedicated micro-ornamentations according to the respective species. All the scales exhibit similar stacked layered structures in the cross sectional architecture, while the thickness of the scales from different regions of the same snake varies significantly. Ventral scales are nearly two times thicker than dorsal scales, indicating better wear resistance. Thus, on the one hand, the difference of the structural properties of scales from different regions of the same snake suggests the multi-functional abilities of snake scales. On the other hand, the similarity of the structural properties of the same regional scale between different snake species reveals a common principle of this multi-functionality.

On this account, the wettability, adhesion properties, and spectral transmittance properties were investigated on the three types of regional scales of twelve snake species to characterize this multi-functionality. Water contact angle varies on the dorsal snake scales within the range of 120° - 145° according to different species, while the ventral and spectacle scales show stable values of around 110° and 100°, respectively. Further adhesion measurements using a sharp AFM tip interacting with the snake scales also coincide with the contact angle results. Dorsal scales are able to gradually scatter the light spectrum with the wavelength decreasing. Spectacle scales and ventral scales show similar spectral transmittance pattern, revealing high transmittance values (nearly 90%) in the near-infrared and visible light spectrum but a cut-off in the ultraviolet spectrum.

We, consequently, conclude that snakes evolved micro-ornamentations on different regional scales covering their body for designated functions in order to better fit to their habitat. Ventral or spectacle scales show similar microstructures among different species, respectively, indicating universal functions on these two types of regional scales on snakes. However, micro-ornamentations on dorsal scales evolved diversely according to the demands of individual snakes. More specifically, dorsal scales of most snakes possess a possible self-cleaning ability and light scattering property, which can protect their skin from contaminations and strong solar radiations. As a window for the eyeballs, spectacle scales abandon self-cleaning capability to acquire better spectral visibility and to filter harmful ultraviolet spectrum. This might also be the reason of the flat, uncomplicated topography on spectacle snake scales as self-cleaning ability usually occurs with exquisite and complicated micro- or nanostructures which might reduce the visible light transmittance (*e.g.* on dorsal scales). Ventral scales are considered important for friction or wear related functions because they are commonly in contact with the substratum during snake's locomotion. The correlation between the micro-ornamentations and the frictional functions of ventral snake scales is specifically discussed in the next section.

Mechanism of snakes and sandfish creating friction anisotropy via nano-steps

The investigated snake species show micro-fibril structures with nano-steps at the fibril ends on their ventral scales. Sandfish shows even more apparent nanoscale step structures which are continuously arranged on their dorsal scales. Nanoscale frictional behavior of a sharp AFM tip scanning across the nano-steps on ventral scales of snakes (*N. atra*, *S. diadema*, and *P. guttatus*) and dorsal scales of sandfish demonstrates significant friction anisotropy along the same scanning tracks in two inverse directions (upward and downward the step). This reveals that snakes and sandfish exploit the same mechanism of creating friction anisotropy by nano-step structures.

It is also interesting to note that, for all the three investigated snakes, friction of the AFM tip scanning upward the nano-step increases with its step height leading to large frictional coefficients. However, downward step friction behaves nearly independent of the step height. The resulting friction coefficient is very close to that on the fibril terraces, which is mainly determined by the material properties of the snake scales. Hence, it seems that the nano-step structures on ventral snake scales are responsible for increasing friction when snakes locomote in the direction of upward the step (corresponding to snake backward motion) but cannot reduce friction in the opposite direction (snake forward motion). This means that the nano-step structures contribute mostly to the generation of friction anisotropy but not to the decrease of friction during snake's locomotion. Very similar friction performance was also found on a polymeric replica of *N. atra* scales, which confirms that the frictional behavior of the nanoscale step edge on snake scales is determined by the structure but not by the material properties. The same effect was also observed by micro-tribometry. Moreover, the friction anisotropy on snake scales is step height dependent. A larger step height induces a larger friction anisotropy. More interestingly, we also observed diverse sections of step heights which induce a variation of frictional anisotropy along the body of snakes. Smallest and largest step heights were found in the head and tail section, respectively, and intermediate values in the other sections. Friction anisotropy manifests the same distribution pattern as the nano-step heights along the snake's bodies. Snakes might benefit from such a design to realize optimized frictional performances during locomotion or when climbing slopes.

Therefore, we conclude that the frictional performance of snakes is determined by the material and structural properties of their ventral scales together. The material properties are important for reducing resistance with low friction coefficients, while the nanoscale step structures are responsible for providing diverse sections of frictional anisotropy along the snake's bodies. This construction principle may be used to embed nano-steps on low friction surfaces (*e.g.* metals or ceramics) in order to achieve desirable friction anisotropy for potential applications such as snake-shaped robots or digging machines. Besides this, considering that our current studies are mainly conducted on the molted snake scales, further investigations on living animals to check if the micro-fibrils are movable leading to an adjustable step height as well as changeable friction anisotropy at the fibril ends will be of high interest.

Snake-inspired tunable friction anisotropy surface based on SMPs

Inspired by the nano-step structures induced friction anisotropy on ventral snake scales, we developed a smart, tunable friction anisotropy surface by replicating the micro-fibril structures from *N. atra* ventral scales onto SMPs via hot embossing technique. The resulting replica was shown to be able to switch reversibly between a flattened surface and a micro-fibril structured surface. In this way, the friction on the surface was accordingly controlled to switch between nearly isotropic and significantly anisotropic along the longitudinal direction of the micro-fibrils. Moreover, the snake-inspired SMP surface can be repeatedly programmed into a temporarily flattened topography and when necessary, recover to the micro-fibril structured topography upon heating stimulus, leading to an ability of tuning friction anisotropy.

The shape-changing capability of the nano-step height at the micro-fibril ends as well as its induced friction anisotropy on the surface was characterized by AFM. The step height on the SMP replica can be flattened to an average value of about 6 nm in its temporary state and further increase back to nearly 60 nm after full recovery by heating. The corresponding friction anisotropy at the nano-steps was characterized to increase from 1.35 to 3.84 during the same recovery process. Thus, a shape-changing capability of nearly 1000% and 300% was achieved in terms of the step height and friction anisotropy, respectively. In addition, the recovery of the SMP surface is continuous and controllable with heating time. It can be abruptly terminated at any demanded occasion before fully recovered for the purpose of obtaining a desirable step height and friction anisotropy on the surface, making it an intelligent element. Besides this, the step height at any arbitrary state of the SMP surface stays constant with storing time and programming/recovery cycles as long as the surrounding temperature is below its switching temperature (T_{switch}). This behavior reveals an excellent long-term stability and a remarkable reusability. All these outstanding capabilities make the snake-inspired, tunable friction anisotropy surface an ideal device for many potential applications in industry and engineering.

Finally, a novel concept of exploiting the snake-inspired SMP surface as a functional platform for unidirectional transport of micro granular particles was demonstrated. Taking the advantage of the friction anisotropy at the micro-fibril steps, the micro particles on the randomly vibrated, structured SMP surface were directionally transported in the direction of downward the nano-steps. However, after being flattened, the SMP surface behaves nearly isotropic with no unidirectional transportation ability. The experimental results show that the smart SMP surface switching between an isotropic and an anisotropic frictional topography can realize the dynamic control of a microsphere randomly moving around its original location within a 0.1 mm amplitude or unidirectionally moving in downward the nano-step direction for nearly 5 mm. Further tests of simultaneously transporting many microspheres or micro sand particles by the structured SMP surface indicate a potential application as self-cleaning coatings. More interestingly, this method can achieve dry self-cleaning without water or any other liquids, which will be an advantage in extreme dry areas lacking rains. This work also provides a promising prospect for other applications such as particle sorting or separation.

Acknowledgements

Looking back at the past four years, all the experiences about happiness or sadness, success or fail make my time in KIT an amazing adventure which will be extraordinarily unforgettable to me. However, it would not have been possible for me to accomplish this thesis without the support and encouragement from numerous people. Heartfelt gratitude goes to everyone whoever provided his aid and assistance during my Ph.D. journey. Here, I just hope I could recall all the help I received without anyone unmentioned.

First of all, I would like to express my sincere thanks to my supervisor Prof. Dr. Hendrik Hölscher. Thank you for giving me the opportunity to pursue my Ph.D. thesis and the continuous guidance and advice throughout my work. I really learned a lot from you in the field of both “science” and “life”. With knowledge you motivated me to open mind with scientific issues. With wisdom you taught me the optimistic attitude to face problems in life. I believe all of these will benefit me all my life. Lastly, special thanks for your extra help and kind support in the work due to my poor German language.

Next, I want to thank Prof. Dr. Manfred Kohl and Prof. Dr. André Schirmeisen for being the co-referees of my PhD thesis as well as Prof. Dr. Martin Dienwiebel for being the chairman in my Ph.D. examination.

Furthermore, throughout my work I also acquired continuous support from Dr. Guillaume Gomard from Light Technology Institute (LTI), who provided me with adequate experimental samples, creative working ideas and possible experimental instruments. His Ph.D. student Shudong Yu also gave me a great help for the introduction of replicating snake scales and the spectrometer measurement. Shudong is a good listener and adviser when I met obstacles in my work. Many thanks to both of them.

I also want to thank Dr. Christian Greiner and his students Paul Schreiber, Antje Dollmann and Simon Mersch from Institute for Applied Materials (IAM) for their kind help of conducting friction measurements by their different types of micro-tribometers.

In addition, I owe a big thank-you to the staff in IMT: Prof. Dr. Manfred Kohl and his Ph.D. student Sanaz Rastjoo for the help of micromanipulation experiments in the SEM; my research group colleague Richard Thelen for the introduction to AFM as well as his endless, hands-on help throughout my work; my Ph.D. colleague Christian Lutz for teaching me to graft artificial AFM probes and helping me to take SEM images; my Ph.D. colleague Aiman Roslizar for stimulating discussions about self-cleaning surfaces; my Bachelor student Felix Buck for contributing experimental results of water contact angle on snake scales; Dr. Markus Guttmann and his group for the fabrication of the Nickel shim; PD Dr. Matthias Worgull and Marc Schneider for their help in hot embossing experiments; all the other supports from Alexandra Moritz and her workshop team as well as Dr. Uwe Köhler and his clean room team. Special thanks to my colleagues Richard Thelen, Janis Heuer, Luisa Borgmann and Junchi Chen for their proof-reading this thesis and providing helpful suggestions. Extra thanks to Janis for his kind help to translate the abstract of this thesis into a German version.

It is a pleasure to thank the people who provided photos and molted scales of the reptiles investigated in this thesis: Guillaume Gomard, Georg Gassner, Felix Hulbert, Philippe Wolf and Gerrit Jan Verspui. This work would not have been accomplished so smoothly without your generous support.

I kindly acknowledge the financial support from: the China Scholarship Council (CSC) for subsidizing my living fees during my study in KIT; the “Ideenwettbewerb Biotechnologie - Von der Natur lernen” of the

"Ministerium für Wissenschaft, Forschung und Kunst Baden-Württemberg" (7533-7-11.10-22) for supporting my study; the WE Heraeus Communication Program of the "Deutsche Physikalische Gesellschaft" for attending the Spring Meeting of the DPG in Regensburg 2019; Karlsruhe House of Young Scientists (KHYS) for supporting my German language learning and my incomplete research stay abroad. I also owe a big thank-you and sorry to Prof. Dr. Udo Schwarz of Yale University for the help and support during my application of the research stay in Yale. This thesis was also partly carried out with the support of the Karlsruhe Nano Micro Facility (KNMF).

I am thankful for all my friends and basketball mates in Germany, who greatly enriched my life after working time. Just to name a few: Thanks to Jinpeng Liu and Ziyan Zhao for your delicious Sichuan meals which greatly satisfy my taste buds outside China. Thanks to Lei Zheng and Kunxi Zhang for being my best basketball mates making us "The Big Three in Karlsruhe". Regular basketball playing with you gave me a healthy body and clear mind for better facilitating my work. Extra thanks to Lei for being my personal, free barber with occasionally a surprised haircut. Thanks to Ruo Jia for being an energetic companion of "The Big Three" when drinking cocktails. Thank you all for being patient listeners when I need talk.

Special thanks to my girlfriend Yue Yuan. I feel so lucky and proud to have you in the acknowledgement list of both my Master and Ph.D. thesis because I know it is not easy for you to have a boyfriend who is more than 8600 km far away from you. You must endure plenty of difficult time in China alone during these four years. I owe you a big thank-you, and also a big sorry. Thank you for your always understanding and unwavering support. Life in Germany is wonderful, the only pity is without you by my side. I am excited to get reunion with you and looking forward to our future life together.

Finally, I would like to thank my parents for their constantly unconditional trust and support. You encouraged me to make my favorite choices and had my back whenever I need help. My limited words cannot express my gratitude and appreciation for all the things you have done for me. I am so grateful to have you as my parents.

List of publications

Articles

Weibin Wu, Christian Lutz, Simon Mersch, Richard Thelen, Christian Greiner, Guillaume Gomard, Hendrik Hölscher, *Characterization of the microscopic tribological properties of sandfish (Scincus scincus) scales by atomic force microscopy,* Beilstein Journal of Nanotechnology, 9, 2618-2627 (2018).

Weibin Wu, Shudong Yu, Paul Schreiber, Antje Dollmann, Christian Lutz, Guillaume Gomard, Christian Greiner and Hendrik Hölscher, *Variation of the frictional anisotropy on ventral scales of snakes caused by nanoscale steps*, Bioinspiration & Biomimetics, 15, 056014 (2020).

Weibin Wu, Felix Buck, Shudong Yu, Richard Thelen, Guillaume Gomard, and Hendrik Hölscher, *Multifunctional snake scales: the structural property, wettability and spectral transmittance of the dorsal, ventral and spectacle scales of twelve snake species*, in preparation.

Weibin Wu, Markus Guttmann, Marc Schneider, Richard Thelen, Matthias Worgull, Guillaume Gomard, and Hendrik Hölscher, *Snake-inspired, tunable anisotropic frictional surface based on shape-memory polymers for unidirectional transport of microscale particles*, in preparation.

Conference contributions

Oral presentations

Weibin Wu, Shudong Yu, Christian Greiner, Guillaume Gomard, and Hendrik Hölscher. *Nanoscale surface steps as the origin of friction anisotropy of snake scales*. DPG Spring Meeting, Regensburg, Germany, March 31st - April 5th, 2019.

Posters

Weibin Wu, Christian Lutz, Simon Mersch, Richard Thelen, Christian Greiner, Guillaume Gomard, and Hendrik Hölscher. *Characterization of the microscopic tribological properties of sandfish (Scincus scincus) scales by atomic force microscopy*. Nano-BW symposium of the competence network functional nanostructures, Bad Herrenalb, Germany, September 26th - 28th, 2018.

Weibin Wu and Hendrik Hölscher. *Characterization of the frictional properties of reptile scales*. WE-Heraeus-Seminar "Bio-inspired, Nano- and Microstructured Surfaces: New Functionality by Material and Structure", Bad Honnef, Germany, May 29th - 31st, 2017.

Bibliography

[1] Bhushan B., Biomimetics: lessons from nature - an overview, *Phil. Trans. R. Soc. A*, **367**, 1445-1486, 2009.

[2] Hwang J., Jeong Y., Park J. M., Lee K. H., Hong J. W., Choi J., Biomimetics: forecasting the future of science, engineering, and medicine, *Int. J. Nanomedicine*, **10**, 5701-5713, 2015.

[3] Dai Z., Tong J., Ren L., Researches and developments of biomimetics in tribology, *Chinese Sci. Bull.*, **51**, 2681-2689, 2006.

[4] Ivanović L., Vencl A., Stojanović B., Marković B., Biomimetics design for tribological applications, *15th International Conference on Tribology*, Kragujevac Serbia, 663-672, 17-19 May, 2017.

[5] Singh R. A., Yoon E. S., Biomimetics in tribology - recent developments, *J. Korean Phys. Soc.* , **52**, 656-668, 2008.

[6] Ruibal R., Ernst V., The structure of the digital setae of lizards, *J. Morphol.*, **117**, 271-294, 1965.

[7] Barthlott W., Neinhuis C., Purity of the sacred lotus, or escape from contamination in biological surfaces, *Planta,* **202**, 1-8, 1997.

[8] Wen L., Weaver J. C., Lauder G. V., Biomimetic shark skin: design, fabrication and hydrodynamic function, *J. Exp. Biol.*, **217**, 1656-1666, 2014.

[9] Motta P., Habegger M. L., Lang A., Hueter R., Davis J., Scale morphology and flexibility in the shortfin mako *Isurus oxyrinchus* and the blacktip shark *Carcharhinus limbatus*, *J. Morphol.*, **273**, 1096-1110, 2012.

[10] Chen H., Zhang L., Zhang D., Zhang P., Han Z., Bioinspired surface for surgical graspers based on the strong wet friction of tree frog toe pads, *ACS Appl. Mater. Interfaces*, **7**, 13987-13995, 2015.

[11] Federle W., Barnes W. J., Baumgartner W., Drechsler P., Smith J. M., Wet but not slippery: boundary friction in tree frog adhesive toe pads, *J. R. Soc. Interface,* **3**, 689-697, 2006.

[12] Iturri J., Xue L., Kappl M., García-Fernández L., Barnes W. J. P., Butt H. J., *et al.*, Torrent frog-inspired adhesives: attachment to flooded surfaces, *Adv. Funct. Mater.*, **25**, 1499-1505, 2015.

[13] Modesto S. P., Anderson J. S., The phylogenetic definition of reptilia, *Syst. Biol.*, **53**, 815-821, 2004.

[14] Holmberg K., Erdemir A., Influence of tribology on global energy consumption, costs and emissions, *Friction*, **5**, 263-284, 2017.

[15] Stadler A. T., Vihar B., Gunther M., Huemer M., Riedl M., Shamiyeh S., *et al.*, Adaptation to life in aeolian sand: how the sandfish lizard, *Scincus scincus*, prevents sand particles from entering its lungs, *J. Exp. Biol.*, **219**, 3597-3604, 2016.

[16] Arnold E. N., Identifying the effects of history on adaptation: origins of different sand-diving techniques in lizards, *J. Zool.*, **235**, 351-388, 1995.

[17] Baumgartner W., Fidler F., Weth A., Habbecke M., Jakob P., Butenweg C., *et al.*, Investigating the locomotion of the sandfish in desert sand using NMR-imaging, *PLOS ONE*, **3**, e3309, 2008.

[18] Maladen R. D., Ding Y., Li C., Goldman D. I., Undulatory swimming in sand: subsurface locomotion of the sandfish lizard, *Science*, **325**, 314-318, 2009.

[19] Rechenberg I., Tribologie im Dünensand: Sandfisch, Sandboa und Sandschleiche als Vorbild für die Reibungs- und Verschleißminderung, TU-Berlin, pp 1-24, 2009. https://docplayer.org/14947105-Tribologie-im-duenensand.html (accessed on 28.09.2020).

[20] Staudt K., Saxe F., Schmied H., Böhme W., Baumgartner W., Sandfish inspires engineering, *Bioinspiration, Biomimetics, and Bioreplication*, Proc. of SPIE, 79751B, 2011.

[21] Wu W., Lutz C., Mersch S., Thelen R., Greiner C., Gomard G., *et al.*, Characterization of the microscopic tribological properties of sandfish (*Scincus scincus*) scales by atomic force microscopy, *Beilstein J. Nanotechnol.*, **9**, 2618-2627, 2018.

[22] Baumgartner W., Friction reducing sandfish skin, In: Bhushan B. Eds. *Encyclopedia of Nanotechnology*, Springer, Dordrecht, 2015.

[23] Rechenberg I., Khyari A. R., Reibung und Verschleiß am Sandfisch der Sahara, TU-Berlin, pp 1-11, 2004. https://docplayer.org/57379610-Reibung-und-verschleiss-am-sandfisch-der-sahara-ingo-rechenberg-und-abdullah-regabi-el-khyari.html (accessed on 28.09.2020).

[24] Rechenberg I., Khyari A. R., Der Sandskink der Sahara - Vorbild für Reibungs- und Verschleißminderung, TU-Berlin, pp 1-5, 2005. http://docplayer.org/31580421-Der-sandskink-der-sahara-vorbild-fuer-reibungs-und-verschleissminderung.html (accessed on 28.09.2020).

[25] Baumgartner W., Saxe F., Weth A., Hajas D., Sigumonrong D., Emmerlich J., *et al.*, The sandfish's skin: morphology, chemistry and reconstruction, *J. Bionic Eng.*, **4**, 1-9, 2007.

[26] Staudt K., Böhme W., Baumgartner W., Comparative investigations of the sandfish's β-keratin (Reptilia: Scincidae: *Scincus scincus*). Part 2: glycan-based friction reduction, *J. Biomimetics, Biomater. Biomed. Eng.*, **16**, 1-9, 2012.

[27] Vihar B., Hanisch F. G., Baumgartner W., Neutral glycans from sandfish skin can reduce friction of polymers, *J. R. Soc. Interface*, **13**, 20160103, 2016.

[28] Integrated Taxonomic Information System (ITIS). https://www.itis.gov/ (accessed on 09.06.2020).

[29] Gray J., Lissmann H. W., The kinetics of locomotion of the grass-snake, *J. Exp. Biol.*, **26**, 354-367, 1950.

[30] Gray J., The mechanism of locomotion in snakes, *J. Exp. Biol.*, **23**, 101-120, 1946.

[31] Marvi H., Hu D. L., Friction enhancement in concertina locomotion of snakes, *J. R. Soc. Interface*, **9**, 3067-3080, 2012.

[32] Hu D. L., Nirody J., Scott T., Shelley M. J., The mechanics of slithering locomotion, *Proc. Natl. Acad. Sci. U.S.A.*, **106**, 10081-10085, 2009.

[33] Goldman D. I., Hu D. L., Wiggling through the world, *Am. Sci.*, **98**, 314-323, 2010.

[34] Leydig F., Ueber die äusseren Bedeckungen der Reptilien und Amphibien, *Archiv f. mikrosk. Anatomie*, **9**, 753-794, 1873.

[35] Fontarnau R., Bea A., A quick, simple method of replicating for scanning electron microscopy applied to the Oberhäutchen micro-ornamentation study, *J. Herpetol.*, **21**, 366-369, 1987.

[36] Stille B., Dorsal scale microdermatoglyphics and rattlesnake (*Cortalus* and *Sisturus*) phylogeny (Reptilia: Viperidae: Crotalinae), *Herpetologica*, **43**, 98-104, 1987.

[37] Price R. M., Dorsal snake scale microdermatoglyphics: ecological indicator or taxonimical tool, *J. Herpetol.*, **16**, 294-306, 1982.

[38] Price R., Kelly P., Microdermatoglyphics: basal patterns and transition zones, *J. Herpetol.*, **23**, 244-261, 1989.

[39] Price R., Microdermatoglyphics: the Liodytes-Regina problem, *J. Herpetol.*, **17**, 292-294, 1983.

[40] Chiasson R. B., Bentley D. L., Lowe C. H., Scale morphology in Agkistrodon and closely related Crotaline Genera, *Herpetologica*, **45**, 430-438, 1989.

[41] Beyerlein P., Studies on the significance of microdermatoglyphics in viperid systematics. I. The microdermatoglyphics of desert vipers (Squamata: Serpentes: Viperidae), *Herpetozoa*, **11**, 79-86, 1998.

[42] Hoge A. R., Santos P. S., Submicroscopic structure of "stratum corneum" of snakes, *Science*, **118**, 410-411, 1953.

[43] Chiasson R. B., Lowe C. H., Ultrastructural scale patterns in *Nerodia* and *Thamnophis*, *J. Herpetol.*, **23**, 109-118, 1989.

[44] Gower D. J., Scale microornamentation of uropeltid snakes, *J. Morphol.*, **258**, 249-268, 2003.

[45] Baum M. J., Kovalev A. E., Michels J., Gorb S. N., Anisotropic friction of the ventral scales in the snake *Lampropeltis getula californiae*, *Tribol. Lett.*, **54**, 139-150, 2014.

[46] Benz M. J., Lakhtakia A., Kovalev A. E., Gorb S. N., Anisotropic frictional properties in snakes, *Bioinspiration, Biomimetics, and Bioreplication*, Proc. of SPIE, San Diego, 83390X, 4 April, 2012.

[47] Filippov A. E., Gorb S. N., Modelling of the frictional behaviour of the snake skin covered by anisotropic surface nanostructures, *Sci. Rep.*, **6**, 23539, 2016.

[48] Baum M. J., Heepe L., Gorb S. N., Friction behavior of a microstructured polymer surface inspired by snake skin, *Beilstein J. Nanotechnol.*, **5**, 83-97, 2014.

[49] Hazel J., Stone M., Grace M. S., Tsukruk V. V., Nanoscale design of snake skin for reptation locomotions via friction anisotropy, *J. Biomech.*, **32**, 477-484, 1999.

[50] Abdel-Aal H. A., Vargiolu R., Zahouani H., El Mansori M., Preliminary investigation of the frictional response of reptilian shed skin, *Wear*, **290-291**, 51-60, 2012.

[51] Abdel-Aal H. A., El Mansori M., Tribological analysis of the ventral scale structure in a *Python regius* in relation to laser textured surfaces, *Surf. Topogr.: Metrol. Prop.*, **1**, 015001, 2013.

[52] Abdel-Aal H. A., On surface structure and friction regulation in reptilian limbless locomotion, *J. Mech. Behav. Biomed. Mater.*, **22**, 115-135, 2013.

[53] Sivak J. G., The role of the spectacle in the visual optics of the snake eye, *Vision Res.*, **17**, 293-298, 1977.

[54] Stabler R. M., Frequency of skin shedding in snakes, *Copeia*, **4**, 227-229, 1939.

[55] Lillywhite H. B. *How Snakes Work*. Oxford University Press. New York. 2014.

[56] Spinner M., Gorb S. N., Westhoff G., Diversity of functional microornamentation in slithering geckos *Lialis* (Pygopodidae), *Proc. R. Soc. B*, **280**, 20132160, 2013.

[57] Campbell A. L., Bunning T. J., Stone M. O., Church D., Grace M. S., Surface ultrastructure of pit organ, spectacle, and non pit organ epidermis of infrared imaging boid snakes: a scanning probe and scanning electron microscopy study, *J. Struct. Biol.*, **126**, 105-120, 1999.

[58] Maderson P. F. A., Histological changes in the epidermis of the tokay (*Gekko gecko*) during the sloughing cycle, *J. Morphol.*, **119**, 39-50, 1966.

[59] Ruibal R., The ultrastructure of the surface of lizard scales, *Copeia*, **4**, 698-703, 1968.

[60] Porter W. P., Solar radiation through the living body walls of vertebrates with emphasis on desert reptiles, *Ecol. Monogr.*, **37**, 273-296, 1967.

[61] Spinner M., Kovalev A., Gorb S. N., Westhoff G., Snake velvet black: hierarchical micro- and nanostructure enhances dark colouration in *Bitis rhinoceros*, *Sci. Rep.*, **3**, 1846, 2013.

[62] Comanns P., Effertz C., Hischen F., Staudt K., Bohme W., Baumgartner W., Moisture harvesting and water transport through specialized micro-structures on the integument of lizards, *Beilstein J. Nanotechnol.*, **2**, 204-214, 2011.

[63] Gans C., Baic D., Regional specialization of reptilian scale surfaces relation of texture and biologic role, *Science*, **195**, 1348-1350, 1976.

[64] Spinner M., Gorb S. N., Balmert A., Bleckmann H., Westhoff G., Non-contaminating camouflage: multifunctional skin microornamentation in the West African Gaboon Viper (*Bitis rhinoceros*), *PLOS ONE*, **9**, e91087, 2014.

[65] Berthé R. A., Westhoff G., Bleckmann H., Gorb S. N., Surface structure and frictional properties of the skin of the Amazon tree boa *Corallus hortulanus* (Squamata, Boidae), *J. Comp. Physiol. A*, **195**, 311-318, 2009.

[66] Greiner C., Schafer M., Bio-inspired scale-like surface textures and their tribological properties, *Bioinspir. Biomim.*, **10**, 044001, 2015.

[67] Gart S. W., Mitchel T. W., Li C., Snakes partition their body to traverse large steps stably, *J. Exp. Biol.*, **222**, jeb185991, 2019.

[68] Sharpe S. S., Koehler S. A., Kuckuk R. M., Serrano M., Vela P. A., Mendelson III J., *et al.*, Locomotor benefits of being a slender and slick sand-swimmer, *J. Exp. Biol.*, **218**, 440-450, 2015.

[69] Abdel-Aal H. A., Vargiolu R., Zahouani H., El Mansori M., A study on the frictional response of reptilian shed skin, *J. Phys.: Conf. Ser.*, **311**, 012016, 2011.

[70] Müller T., Lohrmann M., Kässer T., Marti O., Mlynek J., Krausch G., Frictional force between a sharp asperity and a surface step, *Phys. Rev. Lett.*, **79**, 5066-5069, 1997.

[71] Steiner P., Gnecco E., Krok F., Budzioch J., Walczak L., Konior J., *et al.*, Atomic-scale friction on stepped surfaces of ionic crystals, *Phys. Rev. Lett.*, **106**, 186104, 2011.

[72] Hölscher H., Ebeling D., Schwarz U. D., Friction at atomic-scale surface steps: experiment and theory, *Phys. Rev. Lett.*, **101**, 246105, 2008.

[73] Safer A. B., Grace M. S., Kemeny G. J., Mid-infrared transmission and reflection microspectroscopy: analysis of a novel biological imaging system: the snake infrared-imaging pit organ, The application notebook: molecular spectroscopy, pp 16-18, 2007. http://alfresco-static-

files.s3.amazonaws.com/alfresco_images/pharma/2014/08/21/d72880d6-b21d-48e0-a126-2efd87ca4dfb/article-469980.pdf (accessed on 28.09.2020).

[74] Hart N. S., Coimbra J. P., Collin S. P., Westhoff G., Photoreceptor types, visual pigments, and topographic specializations in the retinas of hydrophiid sea snakes, *J. Comp. Neurol.*, **520**, 1246-1261, 2012.

[75] van Doorn K., Sivak J. G., Spectral transmittance of the spectacle scale of snakes and geckos, *Contrib. Zool.*, **84**, 1-12, 2015.

[76] Simoes B. F., Sampaio F. L., Douglas R. H., Kodandaramaiah U., Casewell N. R., Harrison R. A., *et al.*, Visual pigments, ocular filters and the evolution of snake vision, *Mol. Biol. Evol.*, **33**, 2483-2495, 2016.

[77] van Doorn K. Investigations on Reptilian Spectacle. Ph.D. Thesis, University of Waterloo, Canada, 2012.

[78] Autumn K., Hansen W., Ultrahydrophobicity indicates a non-adhesive default state in gecko setae, *J. Comp. Physiol. A*, **192**, 1205-1212, 2006.

[79] Schneider J., Djamiykov V., Greiner C., Friction reduction through biologically inspired scale-like laser surface textures, *Beilstein J. Nanotechnol.*, **9**, 2561-2572, 2018.

[80] Cuervo P., López D. A., Cano J. P., Sánchez J. C., Rudas S., Estupiñán H., *et al.*, Development of low friction snake-inspired deterministic textured surfaces, *Surf. Topogr.: Metrol. Prop.*, **4**, 024013, 2016.

[81] Mühlberger M., Rohn M., Danzberger J., Sonntag E., Rank A., Schumm L., *et al.*, UV-NIL fabricated bio-inspired inlays for injection molding to influence the friction behavior of ceramic surfaces, *Microelectron. Eng.*, **141**, 140-144, 2015.

[82] Jost P. *Lubrication (Tribology), Education and Research: A Report on the Present Position and Industry's Needs*. H.M. Stationery Off. London. 1966.

[83] Jost P., Tribology origin and future, *Wear*, **136**, 1-17, 1990.

[84] Binnig G., Quate C. F., Gerber C., Atomic force microscope, *Phys Rev Lett*, **56**, 930-933, 1986.

[85] Mate C. M., McClelland G. M., Erlandsson R., Chiang S., Atomic-scale friction of a tungsten tip on a graphite surface, *Phys. Rev. Lett.*, **59**, 1942-1945, 1987.

[86] Meyer E., Heinzelmann H., Grütter P., Jung T. H., Hidber H. R., Rudin H., *et al.*, Atomic force microscopy for the study of tribology and adhesion, *Thin Solid Films*, **181**, 527-544, 1989.

[87] Carpick R. W., Scratching the surface: fundamental investigations of tribology with atomic force microscopy, *Chem. Rev.*, **97**, 1163-1194, 1997.

[88] Israelachvili J. N. *Intermolecular and Surface Forces*. Academic Press. Amsterdam. 2006.

[89] Mate C. M. *Tribology on the Small Scale*. Oxford University Press. New York. 2008.

[90] Good R. J., On the definition of adhesion, *J. Adhes.*, **8**, 1-9, 1976.

[91] Kendall K., The adhesion and surface energy of elastic solids, *J. Phys. D: Appl. Phys.*, **4**, 1186-1195, 1971.

[92] Hejda F., Solař P., Kousal J., Surface free energy determination by contact angle measurement - a comparison of various approaches, *WDS'10 Proceedings of Contributed Papers (Part III)*, Matfyzpress, Prague, pp 25-30, 2010.

[93] Owens D. K., E. I. du Pont de Nemours & Co., Film S., Estimation of the surface free energy of polymers, *J. Appl. Polym. Sci.*, **13**, 1741-1747, 1969.

[94] Wu S., Calculation of interfacial tension in polymer systems, *J. Polym. Sci. C*, **34**, 19-30, 1971.

[95] Neumann A. W., Good R. J., Hope C. J., Sejpal M., An equation-of-state approach to determine surface tensions of low-energy solids from contact angles, *J. Colloid Interface Sci.*, **49**, 291-304, 1974.

[96] Kwok D. Y., Lam C. N. C., Li A., Zhu K., Wu R., Neumann A. W., Low-rate dynamic contact angles on polystyrene and the determination of solid surface tensions, *Polym. Eng. Sci.*, **38**, 1675-1684, 1998.

[97] Packham D. E., Surface energy, surface topography and adhesion, *Int. J. Adhes. Adhes.*, **23**, 437-448, 2003.

[98] Hutchings I. M., Leonardo da Vinci's studies of friction, *Wear*, **360-361**, 51-66, 2016.

[99] Amontons G., De la résistance causée dans les machines, Mémoires de l'Académie Royale A, pp 257-282, 1699.

[100] Dowson D. *History of Tribology*. Longman. London. 1979.

[101] Gao J., Luedtke W. D., Gourdon D., Ruths M., Israelachvili J. N., Landman U., Frictional forces and amontons' law: from the molecular to the macroscopic scale, *J. Phys. Chem. B*, **108**, 3410-3425, 2004.

[102] Rabinowicz E. *Friction and Wear of Materials (2nd Edition)*. John Wiley & Sons. New Jersey. 1995.

[103] Persson B. N. J., Tosatti E. *Physics of Sliding Friciton*. Sringer. Dordrecht. 1996.

[104] Yoshizawa H., Chen Y.-L., Israelachvili J., Fundamental mechanisms of interfacial friction. 1. Relation between adhesion and friction, *J. Phys. Chem.*, **97**, 4128-4140, 1992.

[105] Greenwood J. A., Williamson J. B. P., Contact of nominally flat surfaces, *Proc. R. Soc. Lond. A*, **295**, 300–319, 1966.

[106] Kato K., Wear in relation to friction - a review, *Wear*, **241**, 151-157, 2000.

[107] Khruschov M. M., Principles of abrasive wear, *Wear*, **28**, 69-88, 1974.

[108] Suh N. P., The delamination theory of wear, *Wear*, **25**, 111-124, 1973.

[109] Trezona R. I., Allsopp D. N., Hutchings I. M., Transitions between two-body and three-body abrasive wear influence of test conditions in the microscale abrasive wear test, *Wear*, **225-229**, 205-214, 1999.

[110] Uetz H., Föhl J., Wear as an energy transformation process, *Wear*, **49**, 253-264, 1978.

[111] Archard J. F., Contact and rubbing of flat surfaces, *J. Appl. Phys.*, **24**, 981-988, 1953.

[112] McDiarmid R. W., Campbell J. A., Touré T. A. *Snake Species of the World: A Taxonomic and Geographic Reference*. Herpetologists' League. Washington, DC. 1999.

[113] Mehrtens J. M. *Living Snakes of the World in Color*. Sterling Pub Co Inc. New York. 1987.

[114] Liu C., Qin H., Mather P. T., Review of progress in shape-memory polymers, *J. Mater. Chem.*, **17**, 1543, 2007.

[115] Lendlein A., Kelch S., Shape-memory polymers, *Angew. Chem. Int. Ed.*, **41**, 2034-2057, 2002.

[116] Mather P. T., Luo X., Rousseau I. A., Shape memory polymer research, *Annu. Rev. Mater. Sci.*, **39**, 445-471, 2009.

[117] Lendlein A., Jiang H., Jünger O., Langer R., Light-induced shape-memory polymers, *Nature*, **434**, 879-882, 2005.

[118] Cho J. W., Kim J. W., Jung Y. C., Goo N. S., Electroactive shape-memory polyurethane composites incorporating carbon nanotubes, *Macromol. Rapid Commun.*, **26**, 412-416, 2005.

[119] Mohr R., Kratz K., Weigel T., Lucka-Gabor M., Moneke M., Lendlein A., Initiation of shape-memory effect by inductive heating of magnetic nanoparticles in thermoplastic polymers, *Proc. Natl. Acad. Sci. U.S.A.*, **103**, 3540-3545, 2006.

[120] Chae Jung Y., Hwa So H., Whan Cho J., Water-responsive shape memory polyurethane block copolymer modified with polyhedral oligomeric silsesquioxane, *J. Macromol. Sci. B*, **45**, 453-461, 2006.

[121] Huang W. M., Yang B., An L., Li C., Chan Y. S., Water-driven programmable polyurethane shape memory polymer: demonstration and mechanism, *Appl. Phys. Lett.*, **86**, 114105, 2005.

[122] Hager M. D., Bode S., Weber C., Schubert U. S., Shape memory polymers: past, present and future developments, *Prog. Polym. Sci.*, **49-50**, 3-33, 2015.

[123] Zhao Q., Qi H. J., Xie T., Recent progress in shape memory polymer: new behavior, enabling materials, and mechanistic understanding, *Prog. Polym. Sci.*, **49-50**, 79-120, 2015.

[124] Maitland D. J., Metzger M. F., Schumann D., Lee A., Wilson T. S., Photothermal properties of shape memory polymer micro-actuators for treating stroke, *Lasers Surg. Med.*, **30**, 1-11, 2002.

[125] Jin Yoo H., Chae Jung Y., Gopal Sahoo N., Whan Cho J., Polyurethane-carbon nanotube nanocomposites prepared by in-situ polymerization with electroactive shape memory, *J. Macromol. Sci. B*, **45**, 441-451, 2006.

[126] Xu H., Yu C., Wang S., Malyarchuk V., Xie T., Rogers J. A., Deformable, programmable, and shape-memorizing micro-optics, *Adv. Funct. Mater.*, **23**, 3299-3306, 2013.

[127] Schauer S., Meier T., Reinhard M., Rohrig M., Schneider M., Heilig M., *et al.*, Tunable diffractive optical elements based on shape-memory polymers fabricated via hot embossing, *ACS Appl. Mater. Interfaces*, **8**, 9423-9430, 2016.

[128] Xie T., Xiao X., Li J., Wang R., Encoding localized strain history through wrinkle based structural colors, *Adv. Mater.*, **22**, 4390-4394, 2010.

[129] Rodriguez E. D., Luo X., Mather P. T., Linear/network poly(epsilon-caprolactone) blends exhibiting shape memory assisted self-healing (SMASH), *ACS Appl. Mater. Interfaces*, **3**, 152-161, 2011.

[130] Lendlein A., Langer R., Biodegradable, elastic shape-memory polymers for potential biomedical applications, *Science*, **296**, 1673-1676, 2002.

[131] Xie T., Xiao X., Self-peeling reversible dry adhesive system, *Chem. Mat.*, **20**, 2866-2868, 2008.

[132] Eisenhaure J. D., Xie T., Varghese S., Kim S., Microstructured shape memory polymer surfaces with reversible dry adhesion, *ACS Appl. Mater. Interfaces*, **5**, 7714-7717, 2013.

[133] Boesel L. F., Greiner C., Arzt E., del Campo A., Gecko-inspired surfaces: a path to strong and reversible dry adhesives, *Adv. Mater.*, **22**, 2125-2137, 2010.

[134] Eaton P., West P. *Atomic Force Microscopy*. Oxford University Press. New York. 2010.

[135] Guo D., Xie G., Luo J., Mechanical properties of nanoparticles: basics and applications, *J. Phys. D: Appl. Phys.*, **47**, 013001, 2014.

[136] Liu E., Blanpain B., Celis J. P., Calibration procedues for friction measurements with a lateral force microscope, *Wear*, **192**, 141-150, 1996.

[137] Chung K. H., Pratt J. R., Reitsma M. G., Lateral force calibration: accurate procedures for colloidal probe friction measurements in atomic force microscopy, *Langmuir*, **26**, 1386-1394, 2010.

[138] Reitsma M. G., Gates R. S., Cook R. F., Lateral force cantilever for precise atomic force microscope friction measurements, *Proceedings of the XIth International Congress and Exposition*, Society for Experimental Mechanics Inc., Orlando, pp 1-8, 2-5 June, 2008.

[139] Bogdanovic G., Meurk A., Rutland M. W., Tip friction - torsional spring constant determination, *Colloids Surf. B*, **19**, 397-405, 2000.

[140] Schwarz U. D., Köster P., Wisesendanger R., Quantitative analysis of lateral force microscopy experiments, *Rev. Sci. Instrum.*, **67**, 2560-2567, 1996.

[141] BudgetSensors. https://www.budgetsensors.com/all-in-one-afm-probes (accessed on 07.04.2020).

[142] Leite F. L., Bueno C. C., Da Róz A. L., Ziemath E. C., Oliveira O. N., Theoretical models for surface forces and adhesion and their measurement using atomic force microscopy, *Int. J. Mol. Sci.*, **13**, 12773-12856, 2012.

[143] Reimer L. *Scanning Electron Microscopy: Physics of Image Formation and Microanalysis*. Springer. Berlin. 2013.

[144] Becker S., Popp U., Greiner C., A reciprocating optical in situ tribometer with high-speed data acquisition, *Rev. Sci. Instrum.*, **87**, 085101, 2016.

[145] Greiner C., Liu Z., Strassberger L., Gumbsch P., Sequence of stages in the microstructure evolution in copper under mild reciprocating tribological loading, *ACS Appl. Mater. Interfaces*, **8**, 15809-15819, 2016.

[146] Rohrig M., Thiel M., Worgull M., Holscher H., 3D direct laser writing of nano- and microstructured hierarchical gecko-mimicking surfaces, *Small*, **8**, 3009-3015, 2012.

[147] Schmutz J.-E., Schäfer M. M., Hölscher H., Colloid probes with increased tip height for higher sensitivity in friction force microscopy and less cantilever damping in dynamic force microscopy, *Rev. Sci. Instrum.*, **79**, 026103, 2008.

[148] Lutz C. Bio-inspired Dry Adhesives From Carbon Nanofibers and Their Potential Use in Space Technology. Ph.D. Thesis, Karlsruhe Institute of Technology, Germany, 2018.

[149] Ducker W. A., Senden T. J., Pashley R. M., Measurement of forces in liquids using a force microscope, *Langmuir*, **8**, 1831-1836, 1992.

[150] Eaton P., Smith J. R., Graham P., Smart J. D., Nevell T. G., Tsibouklis J., Adhesion force mapping of polymer surfaces: factors influencing force of adhesion, *Langmuir*, **18**, 3387-3389, 2002.

[151] Eaton P., Estarlich F. F., Ewen R. J., Nevell T. G., Smith J. R., Tsibouklis J., Combined nanoindentation and adhesion force mapping using the atomic force microscope: investigations of a filled polysiloxane coating, *Langmuir*, **18**, 10011-10015, 2002.

[152] Xia Y., Whitesides G. M., Soft lithography, *Angew. Chem. Int. Ed. Engl.*, **37**, 550-575, 1998.

[153] Qin D., Xia Y., Whitesides G. M., Soft lithography for micro- and nanoscale patterning, *Nat. Protoc.*, **5**, 491-502, 2010.

[154] Hünig R., Mertens A., Stephan M., Schulz A., Richter B., Hetterich M., *et al.*, Flower power: exploiting plants' epidermal structures for enhanced light harvesting in thin-film solar cells, *Adv. Opt. Mater.*, **4**, 1487-1493, 2016.

[155] Leach R., Giusca C., Guttmann M., Jakobs P.-J., Rubert P., Development of low-cost material measures for calibration of the metrological characteristics of areal surface texture instruments, *CIRP Ann. Manuf. Technol.*, **64**, 545-548, 2015.

[156] Schroers J., Pham Q., Desai A., Thermoplastic forming of bulk metallic glass - a technology for MEMS and microstructure fabrication, *J. Microelectromech. Syst.*, **16**, 240-247, 2007.

[157] Worgull M. *Hot Embossing: Theory and Technology of Microreplication (Micro and Nano Technologies)*. Elsevier Science. Norwich. 2009.

[158] Klein M. C., Gorb S. N., Ultrastructure and wear patterns of the ventral epidermis of four snake species (Squamata, Serpentes), *Zoology*, **117**, 295-314, 2014.

[159] Klein M. C., Deuschle J. K., Gorb S. N., Material properties of the skin of the Kenyan sand boa *Gongylophis colubrinus* (Squamata, Boidae), *J. Comp. Physiol. A*, **196**, 659-668, 2010.

[160] Klein M. C., Gorb S. N., Epidermis architecture and material properties of the skin of four snake species, *J. R. Soc. Interface*, **9**, 3140-3155, 2012.

[161] Jacobs T. D. B., Junge T., Pastewka L., Quantitative characterization of surface topography using spectral analysis, *Surf. Topogr.: Metrol. Prop.*, **5**, 013001, 2017.

[162] Walls G. L., The significance of the reptilian "spectacle", *Am. J. Ophthalmol.*, **17**, 1045-1047, 1934.

[163] Bellairs A. D. A., Underwood G., The origin of snakes, *Biol. Rev.*, **26**, 193-237, 1951.

[164] Lee C., Li Q., Kalb W., Liu X.-Z., Berger H., Carpick R. W., *et al.*, Frictional characteristics of atomically thin sheets, *Science*, **328**, 76-80, 2010.

[165] Filleter T., McChesney J. L., Bostwick A., Rotenberg E., Emtsev K. V., Seyller T., *et al.*, Friction and dissipation in epitaxial graphene films, *Phys. Rev. Lett.*, **102**, 086102, 2009.

[166] Lee H., Lee N., Seo Y., Eom J., Lee S., Comparison of frictional forces on graphene and graphite, *Nanotechnology*, **20**, 325701, 2009.

[167] Levita G., Cavaleiro A., Molinari E., Polcar T., Righi M. C., Sliding properties of MoS_2 layers: load and interlayer orientation effects, *J. Phys. Chem. C*, **118**, 13809-13816, 2014.

[168] Klein M. G., Gorb S. N., Scratch resistance of the ventral skin surface in four snake species (Squamata, Serpentes), *Zoology*, **119**, 81-96, 2016.

[169] Baum M. J., Heepe L., Fadeeva E., Gorb S. N., Dry friction of microstructured polymer surfaces inspired by snake skin, *Beilstein J. Nanotechnol.*, **5**, 1091-1103, 2014.

[170] Abdel-Aal H. A., El Mansori M., Zahouani H., A comparative study of frictional response of shed snake skin and human skin, *Wear*, **376-377**, 281-294, 2017.

[171] Marvi H., Cook J. P., Streator J. L., Hu D. L., Snakes move their scales to increase friction, *Biotribology*, **5**, 52-60, 2016.

[172] Jayne B. C., Bennett A. F., The effect of tail morphology on locomotor performance of snakes: a comparison of experimental and correlative methods, *J. Exp. Zool.*, **252**, 126-133, 1989.

[173] Onal C. D., Rus D., Autonomous undulatory serpentine locomotion utilizing body dynamics of a fluidic soft robot, *Bioinspir. Biomim.*, **8**, 026003, 2013.

[174] Nor N. M., Ma S., Smooth transition for CPG-based body shape control of a snake-like robot, *Bioinspir. Biomim.*, **9**, 016003, 2014.

[175] Hopkins J. K., Spranklin B. W., Gupta S. K., A survey of snake-inspired robot designs, *Bioinspir. Biomim.*, **4**, 021001, 2009.

[176] Wu W., Yu S., Schreiber P., Dollmann A., Lutz C., Gomard G., *et al.*, Variation of the frictional anisotropy on ventral scales of snakes caused by nanoscale steps, *Bioinspir. Biomim.*, **15**, 056014, 2020.

[177] Meier T. Magnetoresistive and Thermoresistive Scanning Probe Microscopy with Applications in Micro- and Nanotechnology. Ph.D. Thesis, Karlsruhe Institute of Technology, Germany, 2014.

[178] Cuddihy E. F., Theoretical considerations of soil retention, *Sol. Energy Mater.*, **3**, 21-33, 1980.

[179] Chen J.-D., Zhou L., Ou Q.-D., Li Y.-Q., Shen S., Lee S.-T., *et al.*, Enhanced light harvesting in organic solar cells featuring a biomimetic active layer and a self-cleaning antireflective coating, *Adv. Energy Mater.*, **4**, 1301777, 2014.

[180] Verho T., Bower C., Andrew P., Franssila S., Ikkala O., Ras R. H., Mechanically durable superhydrophobic surfaces, *Adv. Mater.*, **23**, 673-678, 2011.

[181] Tsui K. H., Lin Q., Chou H., Zhang Q., Fu H., Qi P., *et al.*, Low-cost, flexible, and self-cleaning 3D nanocone anti-reflection films for high-efficiency photovoltaics, *Adv. Mater.*, **26**, 2805-2811, 2014.

[182] Vullers F., Fritz B., Roslizar A., Striegel A., Guttmann M., Richards B. S., *et al.*, Self-cleaning microcavity array for photovoltaic modules, *ACS Appl. Mater. Interfaces*, **10**, 2929-2936, 2018.